2008-04-23

Measurements and Modeling of Coal Ash Deposition in an Entrained-Flow Reactor

Ryan P. Blanchard
Brigham Young University - Provo

MEASUREMENTS AND MODELING OF COAL ASH DEPOSITION

IN AN ENTRAINED-FLOW REACTOR

by

Ryan Blanchard

A thesis submitted to the faculty of

Brigham Young University

in partial fulfillment of the requirements for the degree of

Master of Science

Department of Mechanical Engineering

Brigham Young University

August 2008

BRIGHAM YOUNG UNIVERSITY

GRADUATE COMMITTEE APPROVAL

of a thesis submitted by

Ryan Blanchard

This thesis has been read by each member of the following graduate committee and by majority vote has been found to be satisfactory.

Date	Dale R. Tree, Chair

Date	Larry L. Baxter

Date	R. Daniel Maynes

BRIGHAM YOUNG UNIVERSITY

As chair of the candidate's graduate committee, I have read the thesis of Ryan Blanchard in its final form and have found that (1) its format, citations, and bibliographical style are consistent and acceptable and fulfill university and department style requirements; (2) its illustrative materials including figures, tables, and charts are in place; and (3) the final manuscript is satisfactory to the graduate committee and is ready for submission to the university library.

_____   _____
Date   Dale R. Tree
                                                                   Chair, Graduate Committee

Accepted for the Department

                                                 _____
                                                              Matthew R. Jones
                                                              Graduate Coordinator

Accepted for the College

                                                 _____
                                                              Alan R. Parkinson
                                                              Dean, Ira A. Fulton College of Engineering
                                                              and Technology

ABSTRACT

MEASUREMENTS AND MODELING OF COAL ASH DEPOSITION

IN AN ENTRAINED-FLOW REACTOR

Ryan Blanchard

Department of Mechanical Engineering

Master of Science

Coal plays a significant role in meeting the world's need for energy and will

continue to do so for many years to come. Economic, environmental, and public opinion

are requiring coal derived energy to be cleaner and operate in a more narrow window of

operating conditions. Fouling and slagging of heat transfer surfaces continues to be a

challenge for maintaining boiler availability and expanding the use of available fuels and

operating conditions. The work incorporates existing information in the literature on ash

deposition into a User-Defined Function (UDF) for a commercial comprehensive

combustion and CFD code. Results from the new submodel and CFD code is are then

compared to deposition measurements in on a simulated boiler tube where particle mass

deposited and ash size distribution are measured.

Several model components governing various aspects of ash deposition have been incorporated into the UDF which has been implemented in a quasi-unsteady Computation Fluid Dynamics (CFD) simulation. The UDF consists of models governing ash particle impaction and sticking, thermal and physical properties of ash deposits, unsteady growth of the ash deposits, and the effects of the insulating ash layers on the combustion processes. The ash layer is allowed to transition from an accumulation of individual particles, to a sintered layer, and finally to a molten or frozen slag layer. The model attempts to predict the deposit thickness, thermal conductivity, and emittance.

Measurements showed fly ash particle sizes that were much smaller than predicted under a non-fragmentation assumption. Use of a fragmentation model matched mean particle diameters well but did not match the upper tail of the particle sizes where inertial impaction takes place. Assuming 100% capture efficiency for all particles provided reasonably good agreement with measured deposition rates. The observed trend of lower deposition rates under reducing conditions was captured when the gas viscosity was calculated using the probe temperature.

ACKNOWLEDGMENTS

I would like to thank Dr. Tree for his mentoring throughout this project. I would also like to thank my committee for their guidance in the completion of this research. I am grateful to my wife who has supported my work in many ways. I am also grateful to the other graduate and undergraduate students with whom I have worked for their help.

TABLE OF CONTENTS

LIST OF TABLES

LIST OF FIGURES

NOMENCLATURE

ACRONYMS

CFD	Computiational fluid dynamics
HMFR	Heated multifuel reactor
UDF	User-defined function
UDM	User-defined memory
UDML	User-defined memory location
SCR	Silicon-controlled rectifier

VARIABLES

a	Kalmanovitch-Urbain pre-exponential factor
A	Area
b	Kalmanovitch-Urbain exponential factor
B	Browning intermediate factor
c	Watt-Fereday model offset
D	Diameter
E_o	Equilibrium Constant
G	Capture efficiency
l	thickness
m	Mass
M	Watt-Fereday coefficient
N	Number of Particles
R	Thermal Resistance
S	Weighting factor
SF	Shape Factor
Stk	Stokes number
T	Temperature
t	time
V	Velocity
η	Impaction efficiency
μ	Viscosity
ρ	Density
ζ	Collection efficiency

1 Introduction

Coal plays a significant role in meeting the world's need for energy and will continue to do so for many years to come. Economic and environmental factors have recently driven research towards making future coal use cleaner and more efficient. One aspect of coal-derived power that has historically been an economic liability is that of fouling and slagging of heat transfer surfaces caused by the accumulation of ash. Efforts to better understand the behavior of these processes by means of in-situ measurements and mathematical models are ongoing. The objective of this research is to implement existing models of coal ash deposition into a CFD-based combustion simulation program and compare the predictions to measured coal ash deposition on a simulated boiler tube.

2007 Energy Information Administration (EIA) data project that coal consumption will increase to nearly 200 quadrillion Btu by 2030 from the current rate of 110 quadrillion Btu which represents a quarter of worldwide energy consumption. In the United States roughly 90% of the 1 billion tons of coal burned each year is used for producing electricity. As economic and environmental concerns over coal power mount, new improvements in efficiency and pollution control are sought in order to maintain coal's viability as a source of energy.

While there are many technologies on the horizon that may help realize increased efficiency and decreased environmental impacts, the accumulation of coal ash on reactor

surfaces could limit the feasibility of these new technologies. Typically 80-95% of coal mass can be used as fuel with the balance being left over as ash. This left over ash often becomes deposited on solid surfaces causing a number of problems including decreased heat transfer, corrosion, and flow blockage. If not removed, deposits can grow large and slough off causing damage to boiler and gasifier walls and in some cases steam related explosions and fatalities. Changes in the type of coal burned can cause currently unpredictable deposition behavior which limits operator flexibility in purchasing coal and increases costs. While ash deposition may not be able to be eliminated, the characterization of the formation and properties of these deposits is critical to managing the problems they cause. The growth rate and thermal properties of these deposits are strong functions of fuel composition, combustion temperature, aerodynamics, and particle size distribution.

Computation fluid dynamics (CFD) tools have been developed to model coal combustion processes with marked success. But while CFD codes, such as FLUENT, can model combustion of solid-phase coal particles in an oxidizing environment, they are typically poorly equipped to model the deposition of the ash on solid surfaces. Additionally, as heat transfer surfaces become fouled and insulated by ash deposits, heat transfer decreases and their surface temperatures simultaneously increase.

This research has four primary objectives:

- Combine existing deposition-related models into a single user-defined function (UDF) that can be incorporated into a CFD-based coal combustion simulation.

- Complete the fabrication and installation of a new multi-fuel reactor including: assembling existing reactor components, designing and constructing various plumbing and preheating subsystems, and shakedown the reactor by identifying and correcting operational issues to make the reactor fully operational.

- Measure fly ash flux, fly ash particle size distribution, deposition rate, and deposit size distribution for a cylinder in cross-flow geometry in the newly constructed heated multi-fuel reactor (HMFR).

- Compare the measured ash deposition data to the CFD-based predictions under both reducing and oxidizing conditions.

2 Deposition Theory and Literature Review

This chapter discusses the theory behind important factors related to ash deposition and the research which has been done to characterize deposition-related processes. The various deposition mechanisms are described with emphasis being given to the inertial impaction mechanism. Within the context of inertial impaction, special focus is given to particle capture and ash viscosity models. Thermal properties of ash deposits are also discussed.

2.1 Deposition Mechanisms

The processes which govern ash deposition can be divided into five categories: inertial impaction, eddy impaction, thermophoresis, condensation and chemical reaction. The net deposition rate can be represented as the sum of these deposition mechanisms[2].

2.1.1 Inertial Impaction

Inertial impaction is believed to be the dominant deposition mechanisms on superheater tubes or at any location where entrained ash particles are required to turn sharp corners at high velocity. Inertial impaction occurs when a particle has sufficient momentum to impact an obstruction by penetrating the flowfield surrounding the obstruction. Of the particles that do reach the tube some fraction will tend to stick to the

tube and become deposited there. The tendency of particles to stick to the tube is thought to be dependent on the properties of the particle at the moment of impact as well as those of the impacted surface, especially the previously accumulated ash layer. While the physics that lead to particle impaction are fairly well understood, predicting what fraction of impacting particles will stick is much more difficult. As shown in equation 2-1, inertial deposition can be thought of as the product of an impaction efficiency, η, and a capture efficiency, G, which together form a collection efficiency (ζ)[13].

$$Collection \ Efficiency = \zeta = \frac{\dot{m}_{Deposit}}{\dot{m}''_{Ash} A_{Cross}} = \eta \ G \qquad \text{(2-1)}$$

2.1.2 Eddy Impaction

Eddy impaction occurs when very fine ash particles located near a solid surface are a blown by turbulent eddies onto the surface where they become deposited. In part due to the complexities of describing near-wall turbulent eddies, this mechanism is not well understood[2].

2.1.3 Thermophoresis

Steep thermal gradients surrounding a particle can give rise to thermophoretic forces. Thermophoresis, which is significant only for very fine particles, typically transports particles towards regions of lower temperature, which, in the case of a cooled superheater tube, drives particles toward the tube and can lead to deposition. Ash deposited by thermophoresis is generally more evenly distributed around a superheater

tube whereas inertial impaction will occur only on the tube's upstream side. As the insulating layer of ash accumulates and the temperature difference between the gas and the deposit surface temperature decreases, thermophoretic deposition also decreases[10].

2.1.4 Condensation

Condensation occurs when mass from the gas phase collects on a cool surface. Relatively low temperatures near a cooled tube can cause certain gas-phase constituents to condense and accumulate. In addition to temperature, condensation is also dependent on the concentrations of these various constituents in the gas phase. Condensation is typically of greater concern in biomass applications or wherever a large amount of inorganic material (particularly alkali salts) is present in the fuel[13].

2.1.5 Chemical Reaction

Chemical reactions between the solid and gas phases can also change the net rate of mass deposition. These reactions may also affect the properties of the ash deposit by changing the temperatures at which sintering and melting occur, which can in turn affect the number of particles captured during inertial impaction processes.

2.1.6 Other Mechanisms

Several other mechanisms exist which may play a role in deposit formation. These other mechanisms include electrostatic forces, photophoresis, and Brownian motion. Current understanding however suggests that these mechanisms are not significant in the formation of deposits[2].

2.2 Inertial Impaction and Capture Models

Several inertial impaction models have been suggested to describe the likelihood of a particle sticking to the surface which it has impacted. These models, which typically use one of two approaches, attempt to capture the effects of numerous variables on sticking propensity. A partial list of these variables would include:

- Particle Composition

- Particle Temperature

- Surface Temperature

- Surface Roughness

- Surface Material/Composition

- Impaction Angle

- Particle Velocity at Impact

One approach used in literature compares the kinetic energy of the impacting particle with a prediction of energy dissipation at impact[12]. A second method predicts an effective viscosity for the particle and/or the impacted surface and predicts an effective stickiness of the impact[20].

2.2.1 Impaction Efficiency

Particle impaction is the first step in describing the inertial deposition mechanism. For a particle to deposit on a surface it must have sufficient momentum normal to the surface to penetrate the fluid layer flowing parallel to the surface. This flow penetration ability is described by the Stokes number which can be thought of as a ratio of a particle's stopping distance to the characteristic length of the flow obstruction. The

Stokes number for a spherical particle approaching a cylinder in cross-flow is given in equation 2-2. The Stokes number is seen to be analogous to a Reynolds number multiplied by the ratio of the particle and probe (tube) diameter. Israel and Rosner (1982) developed a relation for impaction efficiency as a function of stokes number which has been widely used in deposition research. Shown in Figure 2-1, Israel's relation is based on a numerical simulation of particles in potential flow field around a cylinder in cross flow which does not include the effects of a viscous boundary layer surrounding the cylinder.

$$ Stk = \frac{\rho_{particle} V_{particle} d^2_{particle}}{9 \mu_{gas} D_{probe}} \tag{2-2} $$
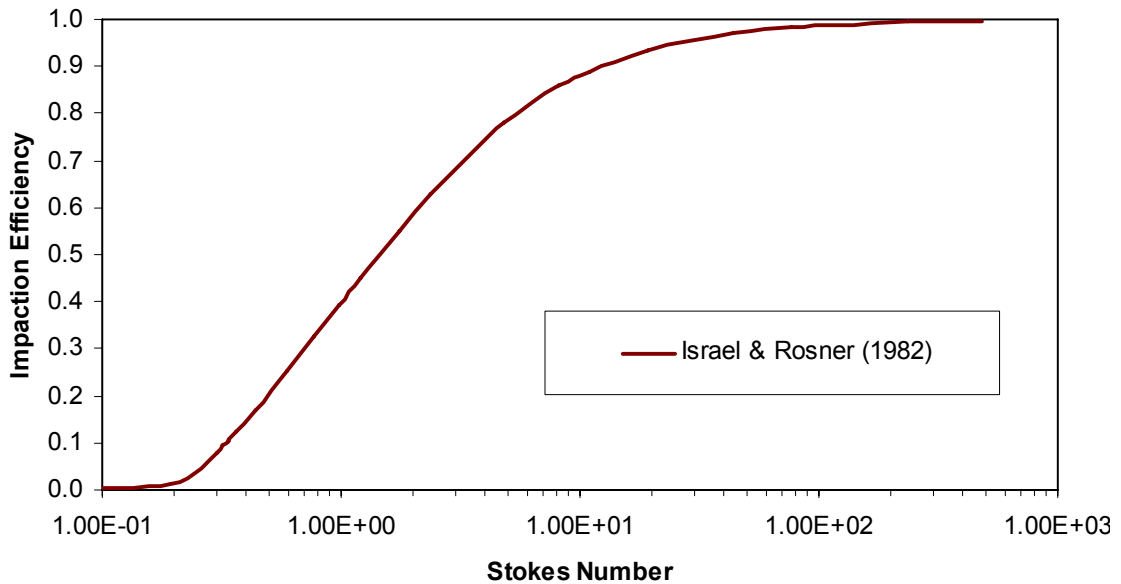
Figure 2-1 Plot of impaction efficiency versus Stokes number.

9

2.2.2   Kinetic Energy Thresholding

The first category of capture models describes inertial impaction in terms of energy exchange. These typically begin by determining the kinetic energy of the particle at the moment of impact and then predict whether the energy dissipated by the collision is sufficient to prevent the particle from rebounding away. If the particle has more kinetic energy than can be dissipated by the collision, the particle is judged to bounce off the surface and not stick to it, however, if the collision can dissipate all of the particle's energy, the particle is judged to stick. Obviously the difficulty with these models arises when trying to predict the amount of energy dissipation as a function of the variables listed previously. One such model, proposed by Li and Ahmadi (1993) and shown below in equation 2-3, predicts a critical velocity as a function of particle mass and coefficient of restitution but an additional model would be needed to predict the coefficient of restitution for the range of impaction conditions that might be encountered.

$$V_{p\_Critical} = \sqrt{\frac{2E_o}{m_p}\left(\frac{1-r^2}{r^2}\right)} \qquad \qquad \textbf{(2-3)}$$

2.2.3   Viscosity-Based Models

Viscosity-based models operate under the assumption that the sticking propensity of particles during inertial impaction is dominated by the effective viscosity of the ash both as entrained particles and also as deposited mass. This effective viscosity is in turn assumed to be a function of temperature and the mass fractions of the various ash constituents. Models that describe this relationship will be described later.

Within the viscosity-based models there are essentially two models for relating viscosity to sticking propensity. The simpler of the two models assumes that an impact involving any viscosity below a predetermined critical viscosity will result in the particle sticking. The second, and most commonly used viscosity-based model, is the one proposed by Walsh et. al (1990) shown as equation 2-4. This assumes that the probability a particle will stick to a surface is inversely proportional to its effective viscosity for viscosities higher than the critical viscosity. For viscosities lower than the critical viscosity, the sticking probability is assumed to be unity. This model is shown mathematically below in equation 2-4. Obviously, in either implementation, the model depends heavily on the value chosen for $\mu_{Critical}$, and unfortunately little consistency exists in the literature for choosing this value, values as low as 1 Pa-s and higher than 10^4 have been reported[22].

$$G = probability\ of\ sticking\ = \min\left[\frac{\mu_{critical}}{\mu}, 1\right] \qquad (2\text{-}4)$$

2.3 Viscosity Models

In order to use the viscosity models discussed previously, a model describing the viscosity of ash is needed. To be useful for deposition modeling, a viscosity must predict ash viscosity as a function of both ash composition and temperature. While many such models have been published, only the most widely used and most validated models are described in this section.

2.3.1 Kalmanovitch-Urbain

A widely used ash viscosity model is that proposed by Urbain (1981) which fit experimental data from a SiO_2-Al_2O_3-CaO-MgO system to the equation shown below as equation 2-5 where a and b are functions of the mole fractions of Al_2O_3 and CaO.

$$\mu = aTe^{1000b/T}$$

(2-5)

2.3.2 Watt-Fereday

Another widely used model was introduced by Watt and Fereday (1969). Like the Urbain model, the Watt-Fereday model also makes use of Al_2O_3 and CaO mole fractions but also allows for Fe_2O_3 and MgO effects. The model, shown below in equation 2-6, includes two composition-dependent parameters, M and c.

$$\log(\mu) = \frac{10^7 M}{(T-150)^2} + c$$

(2-6)

2.3.3 Browning

Browning et al. (2003) developed a model for predicting ash viscosity for coal ash slags by fitting their model to a combination of experimentally measured ash viscosities and synthetic slag viscosity points taken from literature. The model, shown in equation 2-7, 2-8, and 2-9, is based on viscosity data of less than 1000 Pa-s. The model's single compositional parameter, T_S, is a function of the mole fractions of S, Al, Ca, Fe, Mg, Na, K, Mn, Ti, and S and provides an indication of how much each constituent affects the

12

slag viscosity prediction. Browning showed that this model, shown below, provides improvements over the other models discussed here in matching experimental data over the range of ashes studied.

$$\log\left(\frac{\mu}{T-T_S}\right) = \frac{14788}{T-T_S} + 10.931 \tag{2-7}$$

$$T_S = 306.63B - 574.31 \tag{2-8}$$

$$B = \frac{3.19Si + 0.855Al + 1.6K}{0.93Ca + 1.5Fe + 1.21Mg + 0.69Na + 1.35Mn + 1.47Ti + 1.91S} \tag{2-9}$$

2.4   Thermal Properties of Ash

As an ash deposit develops on a heat transfer surface, the insulating properties decrease the net heat transfer rate through the ash layer while also causing the surface temperature of the ash to increase with increasing thickness. This rising surface temperature can lead to the sintering of ash particles at the deposit surface forming a distinct sintered layer on top of the cooler, unsintered particles. If the deposit continues to grow its surface temperature may become high enough that the sintered layer begins to melt and slag. If the slag layer becomes thick enough it may insulate itself to the point that some of the slag may freeze. Each of these four layers, though formed from the same ash, may vary widely in density and thermal conductivity. Cundick et al. (2007)

developed a mathematical model to describe these processes and implemented the model with simplified deposition assumptions in a 2-D boiler model.

2.5   Particle Fragmentation

Particle size plays a very important role in inertial impaction. In the process of burning a single particle of coal, it is very common for a single coal particle to fragment to form numerous ash particles. The propensity of a char particle to fragment is a function of the composition and structure of the char as it burns, but also of the particle size. The literature suggests that numerous mechanisms exist by which a single char particle may yield numerous ash particles. Baxter (1992) determined the net effect encompassing all of these mechanisms and produced an empirical relationship between the number of ash particles per parent char particle over the range of initial particle diameters and for the type of coal used in this research.

3 Objectives

The objectives of this work were listed briefly in the introduction. The objectives are repeated here in more detail with the associated tasks involved in completing each objective. The work reported here is a part of a larger research project focused on measuring and modeling deposition rate and deposit properties including ash thermal conductivity and ash emittance. The focus of the work was therefore selected to make a contribution to group as a whole as well as achieve specific individual objectives.

3.1 User-Defined Function (UDF) Deposition Model

Concurrent with this work, two submodels for deposits were developed, one describing the various layers including thermal conductivity of a deposit as it grows and a second describing the deposit spectral emittance. Both of these models require the deposition rate as an input and both needed to be combined in a single code for validation and demonstration purposes. While most boiler and gasifier manufacturing companies have in-house codes, many also use commercial CFD based combustion codes. It was decided that FLUENT be used as a base combustion code in which to place these new deposition related sub-models. The first objective was therefore to write a deposition rate model and combine the project developed models for deposit growth, conductivity and

emittance into a single code to be implemented in FLUENT through a User Defined Function (UDF). The completion of this objective required the following tasks.

- Learn how to use FLUENT, including combustion modeling and two-phase flow modeling for gas and coal particle phases.

- Learn how to set up and run user defined functions in FLUENT

- Investigate a method for modeling for the collection of ash particles on a solid surface based on FLUENT variables and implement the method in code.

- Combine and code in the UDF the two existing models for ash conductivity and ash emittance to utilize and interface appropriately with FLUENT variables.

3.2 Complete Fabrication and Shake-down of New Reactor

Fabrication of the reactor was completed in several stages consisting of building the main reactor structure from existing components. The second stage comprised designing and building the following: a natural gas preheater, a removable shell to encase the reactor during operation, and a plumbing system that could deliver the required flow rates of air, coal, and natural gas. Drawings and renderings of the various parts of the reactor can be found in the appendix. Finally, the last stage of fabrication was made up of bringing the reactor online, subsystem by subsystem, and solving the various problems that arose until reactor could be used for deposition experiments

The first stage of reactor fabrication was to build the main structure of the reactor from existing components, this included accomplishing the following tasks.

- Install SiC support plates and main reactor tubes on the pre-existing steel support frames.

- Cut insulation panels to size and drill holes for heating elements and access tubes, then install the panels with heating elements already in place.

- Wrap an insulation "belt" around the edges of the support plates to prevent cracking due to excessive thermal stress.

- Install thermocouples in each reactor section and connect them to the control panel for used in feedback control of the heating elements.

- Connect the heating elements to the transformers.

The second stage of reactor construction consisted mostly of designing and building the various reactor accessories needed for proper and safe operation. The following tasks were required to complete this stage of reactor construction:

- Design and build an insulation- and refractory-lined combustor "can" for preheating air with a natural gas flame before the air enters the reactor.

- Design and build an air distribution plenum that distributes a single air stream evenly around the circumference of the combustor can.

- Design and build a combustor "cap" that seals the top of the combustor can and also mates with the pre-existing OEM natural gas burner, the air distribution plenum, and a flame detector.

- Select a ceramic monolith flow straightener to condition the flow between the combustor can and the reactor itself.

- Modify the pre-existing natural gas burner such that the flow rate of premixing air can be measured.

17

- Design and build a removable shell that surround the reactor and prevents accidental contact with hot or high-current surfaces.

The reactor's plumbing system consists of coal, air, and natural gas delivery systems. To make the plumbing system operational the following was actions needed to be taken:

- Design and build a solid-fuel feed lance that can convey entrained pulverized coal into the reactor via any of the reactor's access tubes.

- Design and build a natural gas feed lance that can convey a rich natural gas and air mixture into the reactor via any access tube.

- Install plumbing to carry natural gas or air to the combustor can and to the fuel lances and measure the flow rates of each.

With the reactor construction completed the reactor was brought online and shaken down. During the reactor shakedown process several problems arose which had to be fixed before the reactor could be safely used. The following actions were taken to solve them:

- Install "fence" around reactor exhaust port and plug unused access tubes to alleviate leaking due to the buoyancy of the hot flow.

- Determine sources of electrical system problems including blown fuses, broken heaters, melting heater wires and connection lugs, malfunctioning SCRs, and non-constant zero-points for SCR controllers and fix these problems by replacing the faulty components.

- Modify the coal feeding system to allow higher feed rates, more constant feeding, and higher coal to entrainment air ratio.

3.3   Measure Deposition Rate on Tube in Cross Flow

After the newly constructed reactor had been shaken down it could be used for the deposition experiments. The experiments aimed to determine how the deposition rate would change with changes in temperature, stoichiometry, and exposure time. The tasks associated with these experiments are as follows:

- Run the reactor under-steady state condtions with the prescribed wall temperatures and flow rates that explore the effects of temperature and stoichiometry on deposition behavior.

- Collect an ash deposit on a clean probe sleeve for 10, 20, 40, 60, 90, and 120 minute exposure times and determine the mass of ash collected by weighing the probe before and after the deposit is removed from the sleeve.

- Determine the ash mass flux at the deposition probe's location using the fly ash collection probe for 60 minutes.

- Determine the size distributions of the fly ash and deposits.

3.4   Compare Measurements to Existing Model

In order to determine how well the UDF is able to predict deposition behavior, FLUENT combustion and deposition models were made to simulate the various conditions produced during the deposition experiments. The results of these models' predicted deposition rates were then compared to the experimental measurements. Based on the agreement, or lack of agreement between the predictions and measurements conclusions could be drawn about the ability of the models to predict deposition rates and

capture the trends observed experimentally. The following tasks were to be completed in order to meet this objective.

- Produce two-phase non-premixed combustion models in FLUENT to simulate the conditions in the reactor for the various experiments.

- Produce deposition models in FLUENT based on the velocities, temperatures, etc. of the combustion models, and use these models to predict deposition behavior for each of the experimental conditions.

- Compare the predicted deposition rates to the experimentally produced rates and determine how well they agree.

4   Method

This section deals with the method used in performing the deposition experiments and developing the UDF model.

4.1.1   Experimental Setup and Procedure

This section describes the procedures used to conduct the deposition experiments. The experiments were conducted by exposing a simulated reactor tube to the flow conditions at the exit of the reactor for various lengths of time. The ash deposited on the probe is weighed and collected so that its particle size distribution can be measured. This procedure was repeated for four different flow settings.

4.1.2   Reactor Overview

The new heated multifuel reactor, shown in Figure 4-1, consists of seven identical sections each 61 cm (2 ft.) tall positioned one above the other to yield a total height of 4.3 m (14 ft.). The inside of the reactor is 152 mm (6 in) in diameter and can be accessed every 300 mm axially along the length of the reactor through a number of ports that can be used to introduce fuel, air, or instrumentation to the flow. The primary stream of air entering the top reactor is preheated in a natural gas burner located at the top of the reactor. The preheated flow passes downward through a ceramic flow straightener into

21

the reactor. The reactor is heated by electrical resistance heaters which surround the main reactor tube. The tube and heaters are in turn surrounded by several layers of insulation before the entire reactor is surrounded by a protective metal shell. The exit of the reactor opens into the room where the flow is briefly accessible for deposition measurements before it is mixed with air and is drawn out of the room using an induction fan and exhausted to the roof.
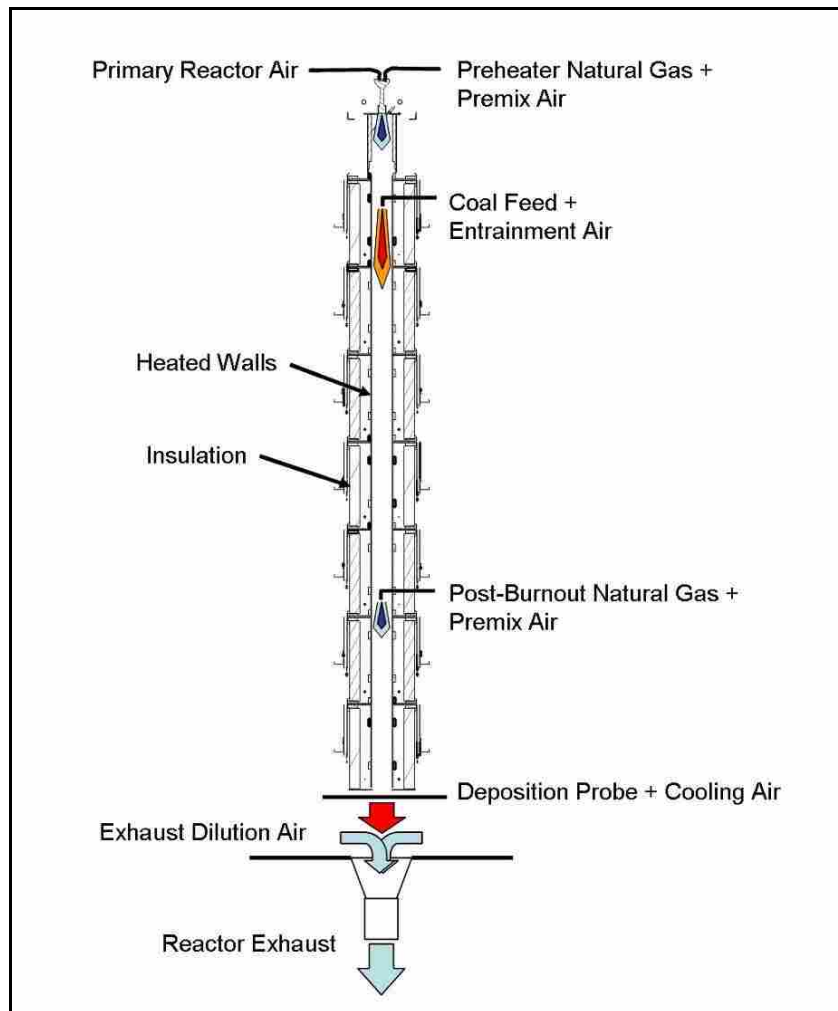
Figure 4-1 Overall reactor layout with typical fuel and air delivery points used in the experiments. The reactor is 4.3 m tall with an inside diameter of 15 cm.

4.1.3   Probe and Sampling Area

The reactor design places the exit of the reactor 35 cm (14 in) above the exhaust port which allows for the hot reactor flow to be accessed before it is mixed and cooled with ambient air in the exhaust. To avoid outside influences, the collection probe (shown in Figure 4-2) on which the deposits were collected was positioned as close to the bottom of the reactor as possible, about 2.5 cm (1 in) below the exit as can be seen in   Figure 4-3 and Figure 4-4. The probe features a removable sleeve 102 mm (4 in) long and 127 mm (0.5 in) in diameter and an adjacent permanent sleeve of the same size and shape. At the end of a deposition experiment, the ash-covered removable sleeve was removed as seen in Figure 4-5, so that the deposit could be weighed and collected. The probe is instrumented with a thermocouple in the permanent sleeve that is embedded in the probe surface 10 mm (0.4 cm) away from the removable sleeve. For each run, the probe was oriented such that the thermocouple was facing upward toward the reactor. It was observed that the deposited mass of ash that stuck to the collection sleeve was uniform along the length of the sleeve and also far enough along the rest of the adjacent probe metal to cover the thermocouple itself. This indicates that the thermocouple was close enough to the deposit to be representative of the sleeve itself. In all cases, the coal was introduced into the reactor through the topmost access port. When reducing conditions were required, additional natural gas was introduced to the flow 762 mm (2.5 ft) above the bottom of the reactor, which still allowed the coal sufficient time under oxidizing conditions to allow the coal to achieve near complete burnout.

Figure 4-2 Cooled deposition probe used to simulate a superheater tube in cross flow. The probe features a 1.2 cm diameter by 10 cm long sleeve that can be removed to allow for easier measurement of the deposited mass

Figure 4-3 Deposition probe installed 2.5 cm below the bottom of the reactor.

Figure 4-4 Typical deposition experiment showing the deposition probe in place under the coal- and natural-gas-fired reactor.

Figure 4-5 Thin deposit layer formed on the probe's deposition sleeve. Note that the sleeve has been removed from the rest of the probe so that the deposit can be weighed and collected.

4.1.4 Isokinetic Fly Ash Sampling

Fly ash was sampled at the reactor exit to determine the size distribution and mass flux of the ash particles at that location. The fly ash was collected with a stainless-steel, water-cooled fly ash collection probe with a variable suction rate. To prevent preferential sampling of the small or large particles within the fly ash size distribution, care was taken to ensure that the ash would be isokinetically sampled. Suction into the fly ash collection probe is controlled by the throat pressure of a venturi located at the end of the probe. The probe's suction rate in ambient air was calibrated as a function of the pressure upstream of the venturi. The calibration was then corrected to account for the viscosity change when the probe would be used to sample hot combustion products. Additionally, a simplified model of fly ash collection process was created in FLUENT whereby the degree to which variations in the probe suction rate would skew the measured size distribution was studied. A uniform distribution of particles across the range of anticipated particle sizes was introduced into the CFD simulation upstream of the simulated collection probe. The distribution of the particles captured by the probe was compared to the desired uniform distribution by means of a normalized chi-square statistic and then plotted against normalized flow rate as shown in Figure 4-6. The simulation was repeated for probes of three different wall thicknesses (D_o/D_i = 1, 1.25, and 1.5). Between calibrating the collection probe and analyzing the results of the sensitivity analysis, it was judged that the flow rate into the collection probe could be well-enough controlled to prevent errors in the measured size distribution.

26
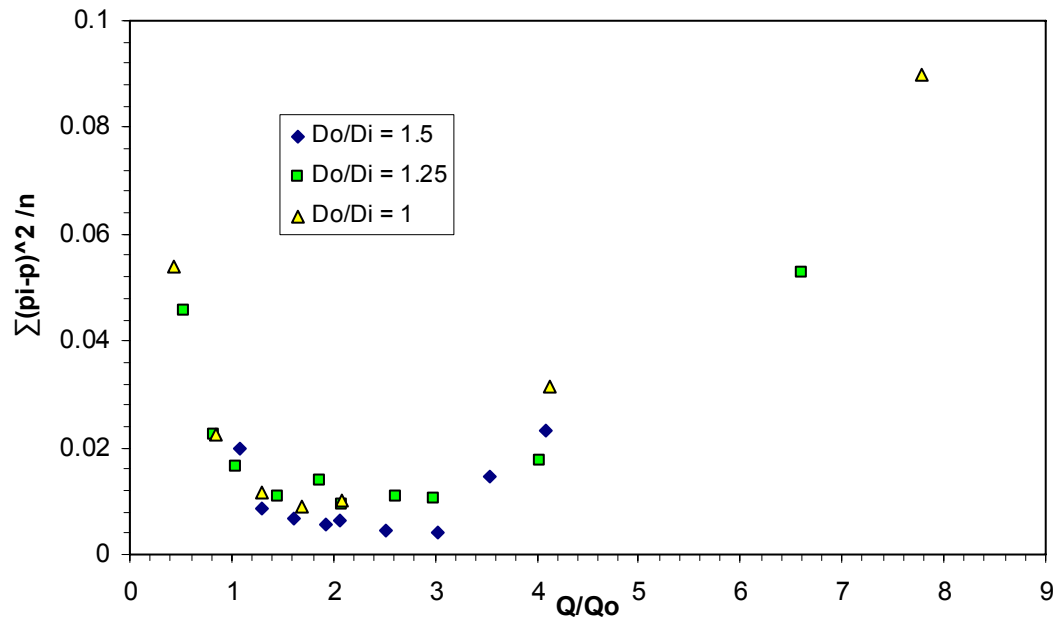
Figure 4-6 Plot showing the predicted effect of suction rate on the amount of deviance of the measured size distribution from the predicted (uniform) size distribution.

4.1.5 Experimental Runs

Four operating conditions were selected for deposition measurement, two under oxidizing and two under reducing conditions. For each of the oxidizing and reducing conditions two particle temperatures were attempted by changing the wall heater temperatures and the gas stoichiometry if possible. The various wall temperatures, air and fuel flow rates, etc. that defined the settings of each experimental run are shown in Table 4-1. These were determined in part by the desire to explore the effects of large changes in parameter values on deposition behavior but in some cases were constrained by operational limitations of the reactors components. Examples of these constraints include minimum wall and flow temperatures to achieve burnout, minimum air flow rates for coal

entrainment, and maximum wall temperature limits to prevent excessive thermal stresses. The resulting set of parameters, though somewhat constrained, represent a wide range of flow temperatures and stoichiometry. Each combination of settings was used to produce a deposit for durations of 10, 20, 40, 60, 90, and 120 minutes, with all but the longest two durations being replicated for uncertainty estimation.

All of the coal burned during the experiment came from a single barrel of White County, Illinois #6 coal. The ultimate and proximate analyses of the coal are given in Table 4-2, with ash composition data in Table 4-3, and fusion temperatures in Table 4-4. This is a high volatile, bituminous coal with intermediate sulfur content. As will be discussed later, this type of coal has been shown in the past to fragment significantly.

Table 4-1 Settings for the four conditions under which deposition was to be measured.

		Oxidizing		Reducing	
		"Cold"	"Hot"	"Cold"	"Hot"
Wall Temperature (°C)		1150	1225	1150	1225
Coal Flow Rate (kg/hr)		0.45	0.45	0.45	0.45
Total Air Flow Rate (kg/hr)		20.2	20.2	20.2	20.2
Preheater Natural Gas Flow Rate (kg/hr)		0.44	0.70	.5	.70
Post Burnout Natural Gas (kg/hr)		0	0	0.5	0.5
Overall Equivalence Ratio		0.62	0.84	1.10	1.26
Probe Temperature (°C)		617	723	770	780
Adiabatic Flame Temperature (°C)		1352	1723	1871	1732
FLUENT Outputs	Velocity (m/s)	1.79	2.12	2.22	2.17
	Temperature (°C)	1303	1563	1624	1568
	Density (kg/m^3)	.179	.154	.149	.153

Table 4-2 Table of analysis results for the White County Illinois #6 coal.

Ultimate and Proximate Analyses of Coal			
		As Received	Moisture Free
Proximate	Moisture %wt	11.09	NA
	Ash %wt	7.17	8.06
	Volatile %wt	37.46	42.13
	Fixed Carbon %wt	44.29	49.81
	Total Sulfur %wt	2.9	3.26
	Heating Value (Btu/lb)	11755	13221
Ultimate	Moisture %wt	11.09	NA
	Carbon %wt	65.21	73.34
	Hydrogen %wt	4.59	5.16
	Nitrogen %wt	1.32	1.49
	Sulfur %wt	2.9	3.26
	Ash %wt	7.17	8.06
	Oxygen (Diff.) %wt	7.72	8.69

Table 4-3 Composition of the coal's ash.

Mineral Analysis of Ash	
SiO_2	50.55
Al_2O_3	18.23
Fe_2O_3	20.6
CaO	2.92
MgO	0.81
Na_2O	1.01
K_2O	2.17
TiO_2	0.95
MnO_2	0.04
P_2O_5	0.17
SrO	0.03
BaO	0.04
SO_3	1.85
Undetermined	0.63

Table 4-4 Fusion temperatures of the ash.

Ash Fusion Temperatures (Celsius)		
	I.D.	1061
Reducing	H = W	1121
	H = W/2	1212
	Fluid	1236
	I.D.	1265
Oxidizing	H = W	1344
	H = W/2	1387
	Fluid	1418

4.2 Model Description

The various models which were combined together into the CFD-based UDF model to describe the ash deposition process will be described in this section. These include models taken from the literature for particle capture and properties of deposit layers as well as models already implemented in FLUENT for solid particle combustion, particle motion, and heat and mass transport models. Also discussed is the coordination algorithm that efficiently manages the flow of information between the UDF's various models within the framework of the FLUENT CFD package.

4.2.1 Combustion Model

The models for solid particle combustion, fluid flow, and particle motion all made use of existing models within FLUENT and receive only brief discussion here. Devolatilization was modeled using a single-rate equation using default values for the pre-exponential factor and activation energy. Char burnout was modeled using a kinetics/diffusion limited model which calculates kinetics-limited and diffusion-limited reaction rates, with the smaller of the two taken to be the assumed rate. Continuous phase

chemistry was assumed to be at equilibrium with preprocessed lookup tables used to calculate flow composition and properties as functions of local transport equation variables (mixture fraction, mixture fraction variance, and temperature). Particle tracking was accomplished using a Lagrangian random-walk model. This model approximates the ensemble of all particle tracks in a turbulent flow with a smaller, user-defined number of of particles that are "walked" through the domain. Each particle travels distance or step where at each step along its path, the drag force on the particle is calculated based on the particle, mean flow, and turbulent velocities. Although the mean flow is fixed by the Eulerian solution and would produce the same drag on every particle, the turbulent flow component is random and therefore produces a drag force unique to each particle. In order for the two-way particle-flow coupling to be physically realistic, each simulated particle must be weighted such that the cumulative effect of the simulated particles approximates the cumulative effect of the actual particles. To reconcile the Eulerian and Lagrangian natures of the fluid and particle flows respectively and the interactions between them, the two simulations are performed in parallel with the Eulerian flow simulation affecting the Lagrangian particles through drag force, diffusion, and thermal transport and the particles affecting the fluid phase through source terms in transport equations (momentum, energy, turbulence etc.). Turbulent fluid flow was modeled using the shear-stress transport (SST) variant of the k-ω closure of the Reynolds-averaged Navier-Stokes transport equations.

4.2.2   Two Simulations in Series

The deposition simulation was conducted as two simulations in series. The first simulation modeled the reactor itself including combustion processes whereas the second

31

modeled the deposition processes. The reactor was modeled assuming a 2-D axisymmetric flowfield using a 25 x 70 structured grid. Boundary conditions for the reactor simulation consisted of two mass flow inlets at the top of the reactor, an isothermal no-slip wall, a centerline axis, and a pressure outlet. Variable values at the exit boundary, with two exceptions (viscosity and particle size), from the combustion simulation were used as the inlet boundary conditions for the deposition simulation. The deposition simulation consisted of a 2-D rectangular grid sized 400mm x 250mm with a 12.5mm diameter circle in the middle to represent the sleeve of the deposition probe. This domain was meshed using unstructured elements surrounding a structured boundary-layer-type grid on the probe wall. The total node count for the deposition simulation was 2223. The reactor and deposition simulations were found to be grid-converged for all variables of interest. The need for the two exceptions arises from the fact that FLUENT's non-premixed, solid-particle combustion models do not predict all of the information necessary for accurate modeling. While FLUENT does predict important gas properties of the mixture of combustion products such as temperature, species' mass fractions, specific heat etc. it does not predict the molecular viscosity of the mixture and instead requires a user-specified viscosity. These values are tabulated for reference in Table 4-1.

The second boundary condition exception, particle size distribution of the burned out fly ash particles, was measured experimentally and then used in the simulation without predictive means of any kind. The only fragmentation models available in FLUENT predict the breakup of liquid droplets as functions of Weber number and are not valid for solid particles. Additional efforts to predict the measured size distribution of fly ash particles based on the size distribution of the pulverized parent coal using models

available in the literature showed decent agreement but were ultimately not successful enough to warrant their use in the deposition simulation.

4.3   Deposition Models

Deposition models taken from literature were chosen to represent the current understanding of inertial deposition and the properties of deposits formed through this mechanism. Where needed, additional models or model parameters have been taken from literature, measured directly, or approximated as nearly as possible.

4.3.1   Particle Capture and Deposit

Particle impaction efficiency was modeled on a particle-by-particle basis using FLUENT's implementation of the stochastic random-walk model. Each particle in the deposition simulation was tracked as it was carried through the computational domain by a combination of steady velocity streamlines and simulated turbulent eddies. Particle capture was modeled using a combination of the Walsh capture model equation equation 4-1 and the Browning viscosity model equations, equations 4-3, and 4-4. The first method of sticking probability involves depositing the particle's mass in a Boolean fashion. The other method, and the one used here assumes that the ratio of mass deposited by a particle to that particle's total effective mass is equal to the sticking probability and thus represents the long term probability of the expected mass deposit from the large number of particles that the single particle represents.

$$ probability\ of\ sticking = \frac{\dot{m}_{deposit}}{\dot{m}_{stream}} = \min\left[\frac{\mu_{critical}}{\mu}, 1\right] \qquad \text{(4-1)} $$

33

The sticking probability is calculated as a ratio of viscosities, where the critical viscosity, $\mu_{Critical}$, the viscosity below which all impacts result in sticking, is assumed to be a constant which can be determined based on a single experiment and then used for subsequent predictions. The effective particle viscosity is assumed to be a function of ash composition and temperature, as calculated with the Browning model, as shown in Figure 4-7 for the ash from three different fuels. The two models combine to form the capture efficiency model shown in Figure 4-8 as a function of temperature for three different values of $\mu_{Critical}$. In this research the predicted deposition rates required using a $\mu_{Critical}$ value of at least 500 Pa-s in order to account for the near-perfect observed capture efficiency. While this model captures important aspects of ash viscosity it does not capture others. For example it does not account for the difference in ash fusion temperatures between ash samples measured under oxidizing vs. reducing conditions as was shown in Table 4-4.

$$\log\left(\frac{\mu}{T-T_S}\right) = \frac{14788}{T-T_S} - 10.931 \qquad \text{(4-2)}$$

$$T_S = 306.63A - 574.31 \qquad \text{(4-3)}$$

$$A = \frac{3.19Si + 0.855Al + 1.6K}{0.93Ca + 1.5Fe + 1.21Mg + 0.69Na + 1.35Mn + 1.47Ti + 1.91S} \qquad \text{(4-4)}$$
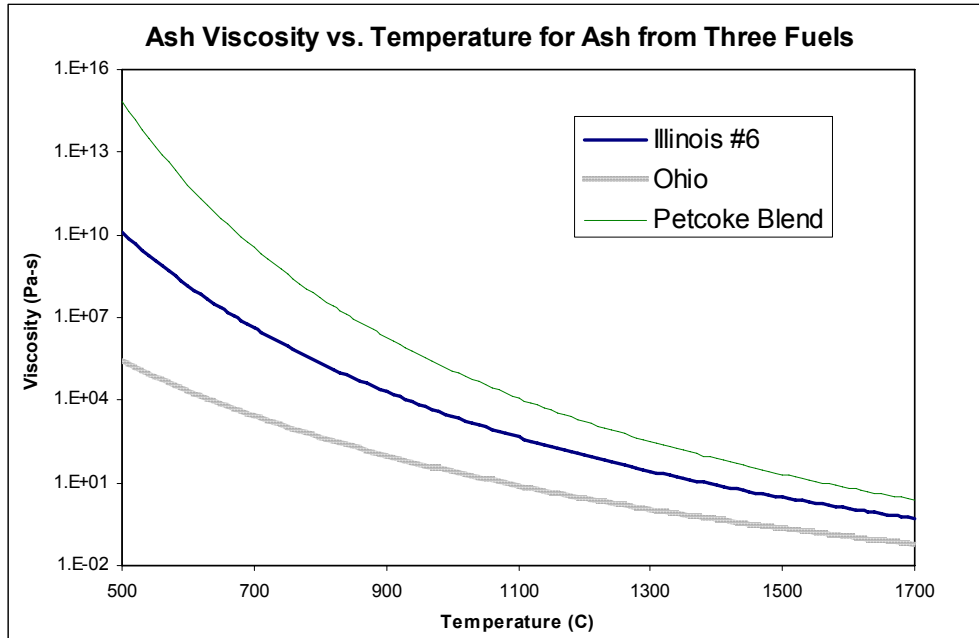
Figure 4-7 Browning-based viscosity predictions for three fuels as functions of temperature.
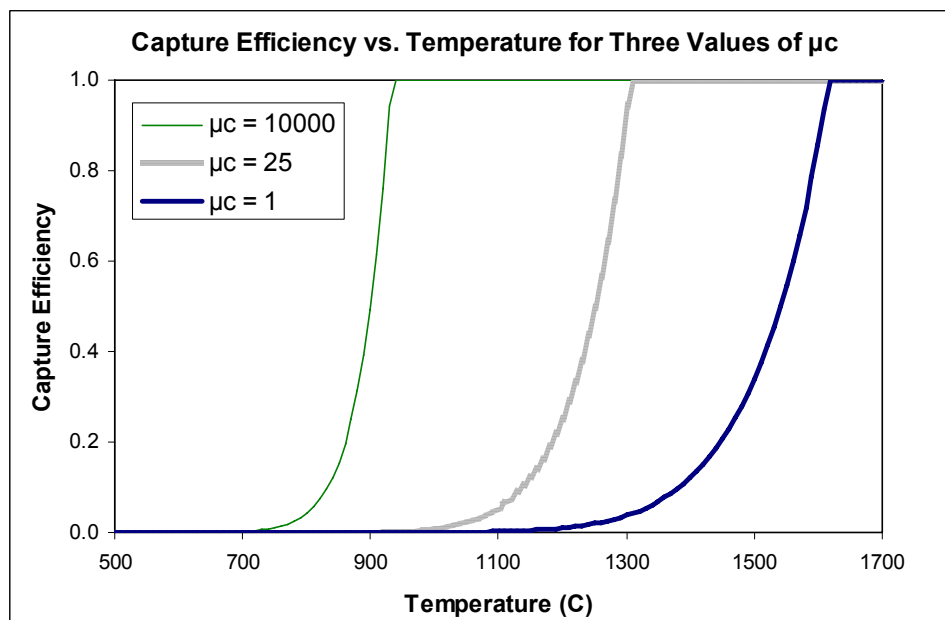

Figure 4-8 Capture efficiency of the Illinois #6 ash using the Browning viscosity model and the Walsh capture model with three values of the Walsh model's critical viscosity parameter.

Since the Browning model captures all of composition information with a single parameter, the shift temperature, T_S, and since the model requires inputs that are generally only available through an ash analysis, it may be possible in the future to add significant accuracy to the viscosity predictions by simply solving for the shift temperature using the ash fusion temperature information which is often included in an ash analysis anyway. This technique would also provide a more reliable way of accounting for the difference in ash viscosity between oxidizing and reducing conditions.

4.3.2   Ash Layer Properties

The thermal properties of accumulated ash layers were described using the model developed by Cundick et al. (2007). The model accounts for the changes a deposit experiences as it grows and insulates the heat transfer surface it covers. Depending on its temperature, the ash can take on particulate, sintered, slag, and frozen slag forms, each with its own density and thermal conductivity. The transitions between particulate, sintered, slag, and frozen slag layers is set to occur at predefined temperatures. The calculated net heat flux through the deposit can account for a combination of ash layers stacked on top of one another. As depicted in Figure 4-9, the model represents the ash layer as a series of thermal resistances between the boundary temperature from the CFD simulation and a user-defined cool side temperature. The heat flux through the layers is then calculated using equation 4-5 and fed back to the CFD simulation as the thermal boundary condition. The total thermal resistance of the deposit is assumed to be the sum of the thermal resistances of its various layers, where the resistance of the ith layer is

calculated with equation 4-6. Slag flow as described in the Cundick model is not currently implemented in the current model.
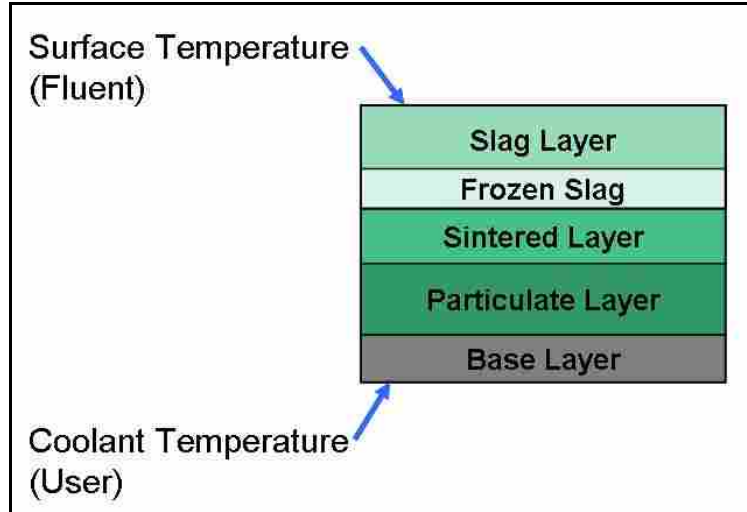

Figure 4-9 Depiction of the various layers of deposit that can be formed. The UDF defines a heat-flux thermal boundary condition based on the thicknesses and thermal conductivities of these layers, the thermal resistance of the user-specified base layer, and the difference between the current FLUENT-specified boundary temperature and the user-defined temperature underneath the base layer.

$$\dot{q}'' = \frac{T_{Surface} - T_{Cool}}{R_{S \, inter} + R_{Particulate} + R_{Frozen} + R_{Slag}} \tag{4-5}$$

$$R_i = \frac{l_i}{k_i} \tag{4-6}$$

4.3.3 Fragmentation

Predicted fly ash size distributions using a no-fragmentation assumption predicted a size distribution that was far larger than the measured fly ash particles. This indicates the presence of a significant amount of particle fragmentation. Using fragmentation results for Illinois #6 coal from Baxter (1992) predicted a size distribution that provided a much better match to the measured fly ash size distribution. The method however did not adequately match to the upper tail of the size range (approximately 30μm), where the bulk of inertial impaction occurred. As a result of these difficulties, prediction of the size distribution of ash particles is not currently included in the UDF. Rather, fragmentation is accounted for by breaking the simulation into two simulations: one for modeling the reactor environment and another for modeling deposition on the probe. The exit conditions (velocity, temperature, etc.) of the reactor simulation are used as the inlet boundary conditions for the deposition simulation with the only exception being the particle size distribution where the size distribution from the reactor is ignored and replaced in the deposition simulation by the measured distribution.

4.4 Coordination Algorithm

The deposition model is a collection of four UDFs that are called by FLUENT at different times to perform the various functions of the model. The role of each of these UDFs and their connection to FLUENT and each other are described in this section.

The first UDF (impaction), called each time a particle impacts a deposition surface, determines how much mass each particle represents, how much of that mass becomes deposited on the surface, which ash layer the mass is added to, and how much

added thickness the mass gives the layer. The second UDF (heat flux), called during each fluent iteration, determines the heat flux through the combined ash and base layers. The third UDF (injection initialization), called each time new particle streams are injected, checks for sintering and slagging of ash layers, and increments the simulation time before injecting a new set of particle streams. The fourth UDF (reset), called on-demand by the user, resets the user-defined memory locations (UDMLs), which store deposit information at each wall-face, to zero. The source code for all four of the UDFs is written in a single file that can be seen in Appendix B.

The algorithm that coordinates the flow of information between the various components of the deposition model consists of an outer loop that marches the deposit growth from time step to time step and an inner loop that solves the steady-state flow and energy equations at each time step, the processes that make up these two loops are shown schematically in Figure 4-10. The outer loop begins with an already-solved flow and energy solution for a clean-wall case, with a converged boundary temperature profile, into which particles are injected. The wall boundary condition related to temperature, thermal resistance, or heat flux are not critical for the initial solution.

The particle streams are tracked by FLUENT through the domain using a stochastic random-walk model. The default boundary condition for a wall dictates that a particle impacting the surface will bounce off and continue in the flow. When the deposition model is selected, particle streams that are carried into a deposition boundary surface are removed from the simulation at the point of impact and added to the deposit mass as dictated by the impaction UDF. The impaction UDF model determines how much mass the particle stream represents and how much of that mass is deposited on the

impacted face. The Heat Flux UDF then calculates thermal resistance for the face and computes the net heat transfer rate through the face based on the new thermal resistance.

FLUENT is then allowed to iterate on the flow and energy solutions without further particle deposition with the heat flux produced by the UDF as a boundary condition until the heat flux produced by the FLUENT flow and energy calculation and the heat flux calculated by the Heat Flux UDF converge.

Once the solution converges, or after a set number of iterations, the model checks to see if any of the particulate layers have sintered, or if any of the sintered layers have slagged. Once the layers have been redistributed to account for sintering and slagging, the simulation time step is incremented, a new set of particles is injected, and the process repeats.

Throughout the simulation process, variables not automatically stored in FLUENT are stored at user-defined memory locations (UDML). The current model uses six such locations, numbered zero to five, and are defined as follows:

- UDML 0 – Total accumulated deposit mass (kg) on the face including slag, sintered, and particulate layers, but not the base layer which has no defined mass.

- UDM 1 – Effective thermal resistance (m-K/W) of the slag, sintered, particulate, and base layers.

- UDM 2 – Thickness of the particulate layer (m).

- UDM 3 – Thickness of the sintered layer (m).

- UDM 4 – Thickness of the slag layer (m).
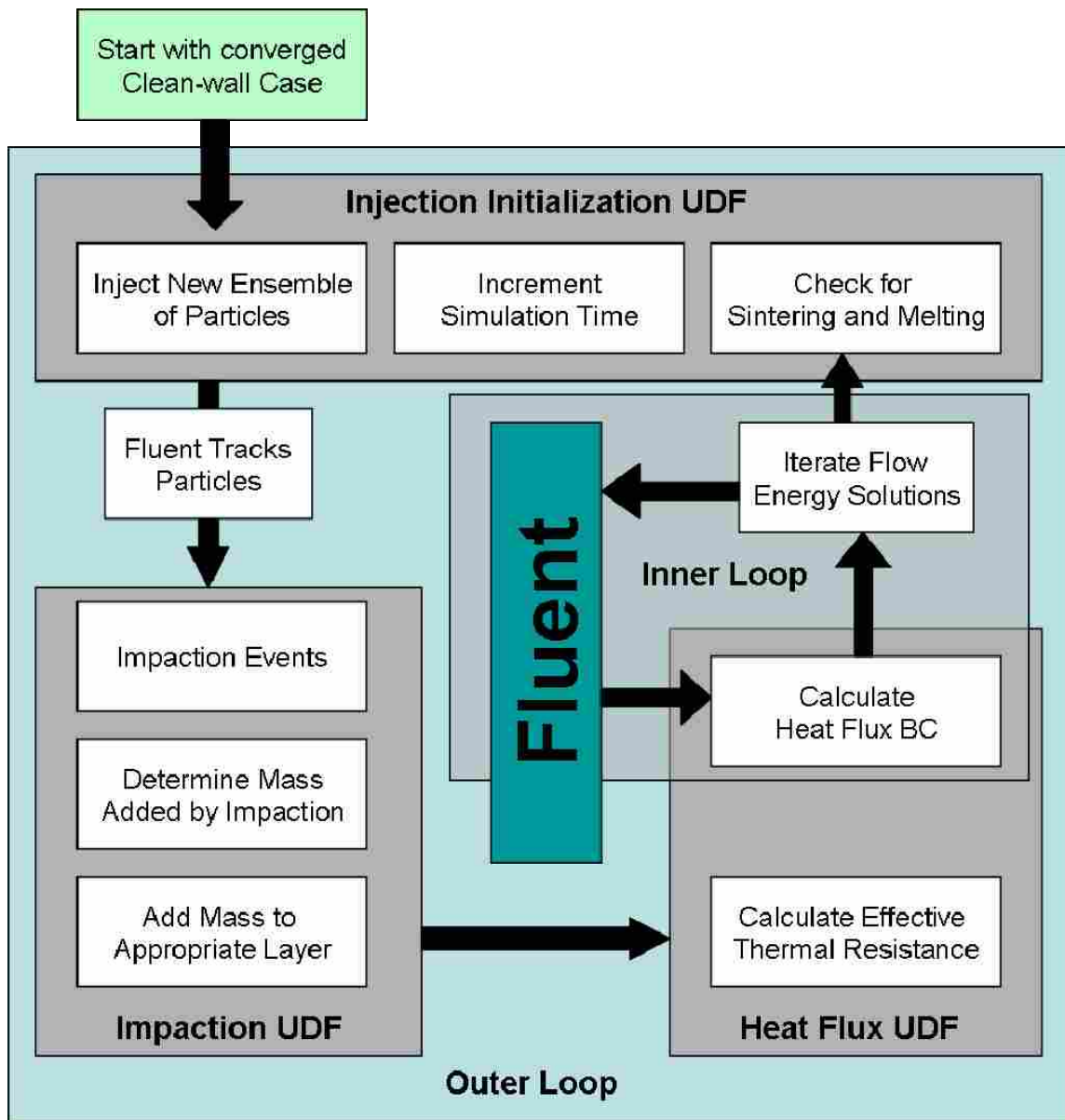
- UDM 5 – Current simulation time (s).

Figure 4-10 Flowchart of operations performed by the model.

4.4.1 Description of Input Parameters

The deposition model requires a number of input parameter values which are stored as global variables for use throughout the simulation process. The definitions of these parameters are given here, including units where applicable, and grouped by category where possible.

- Deposit Properties Parameters

    o T_Cool – Temperature (K) of the cool side of the base resistance layer. If the base resistance layer includes the thermal resistance of an external boundary layer, T_Cool should be the external flow's freestream temperature.

    o T_Slag – Temperature (K) at which ash slagging occurs, this temperature is not calculated by the viscosity model.

    o T_Sinter – Temperature (K) at which sintering occurs, this temperature is not calculated by the viscosity model.

    o K_Slag – Thermal conductivity of the slag layer (W/m-K)

    o K_Sinter – Thermal conductivity of the sinter layer (W/m-K)

    o K_Particulate – Thermal Conductivity of the particulate layer (W/m-K)

    o RHO_Slag – Density of the slag layer (kg/m^3)

    o RHO_Sinter – Density of the sintered layer (kg/m^3)

    o RHO_Particulate – Density of the particulate layer (kg/m^3)

    o R_BASE – Thermal resistance of the base layer (m^2-K/W). This should include any thermal resistance between the top of the "clean" wall and the specified T_Cool, including convection properties of boundary layers etc.

- TIMESTEP_SIZE – Duration of each time step of deposit growth, note that the amount of mass per particle deposited on the probe is proportional to this number

- Particle Capture Parameters

  o T_Shift – This is the shift temperature parameter in the Browning viscosity model, this is a function of ash composition only as shown in the model description section.

  o Critical_viscosity – The critical viscosity (kg/m-s) of ash particles below which particles are assumed to be perfectly sticky.

- Particle Weighting Parameters

  o RR_DBAR – Parameter for characteristic particle diameter (m) of the Rosin-Rammler particle size distribution function.

  o RR_SF – Parameter for shape factor of the Rosin-Rammler particle size distribution function. This parameter is sometimes called the spread parameter or the size distribution parameter, it is typically represented in equations as 'n'.

  o RR_DIAM_MAX – The maximum particle size (m) used in the simulation. Note that this value must correspond to the value entered in the injections panel in Fluent.

  o RR_DIAM_MIN – The minimum particle size (m) used in the simulation. Note that this value must also correspond to the value entered in Fluent's injection panel.

- o RR_MASS_FLOW – Mass flow rate of particles (kg/s). Notice that this

  value does NOT need to correspond to the value entered in Fluent's

  injection panel. This parameter is used to determine how much mass each

  simulation particle represents whereas the injection panel value is used

  only for determining the particle's impact on the fluid domain.

- o RR_NUM_PARTICLES – The total number of particle streams used in

  the simulation. Note that when using a multi-point injector (group,

  surface, etc.) this number will be equal to the number of particle streams

  the specified number of random-walk model "tries."

4.4.2   UDF Hooks

Of the four UDFs that comprise the model, three must be properly "hooked" into FLUENT in order to work together properly, the fourth is executed on demand and is used only for resetting the simulation. The Impaction UDF, which deals with particle impaction, is hooked into FLUENT via the wall boundary conditions panel under the DPM (discrete phase model) tab. The Heat Flux UDF is also hooked into FLUENT via the wall boundary conditions tab, this time under the "thermal" tab. The Injection initialization UDF is hooked into FLUENT through the injections panel under the UDF tab. The additional hooks into FLUENT needed for storing the deposit properties mentioned earlier (layer thickness, total mass, etc.) must be reserved using the user-defined memory menu.

4.4.3 Particle Weighting

FLUENT includes several particle size distributions available for injecting particles into the domain including uniform, Rosin-Rammler, and Rosin-Rammler-Logarithmic. The effect of these distributions is not accounted for by changing the injected number of particle streams of a given diameter, in fact on a number of streams basis, a uniform distribution of particle sizes is always represented. Since the each particle stream injected almost always represents a much larger number of actual particles, each stream is weighted by diameter to account for the desired distribution. FLUENT's UDF manual contains instructions on how to access the mass flow rate represented by a given particle stream from a UDF, when attempted however this function returns an error. To solve this problem the UDF described here does the weighting external to FLUENT's own calculations. Thus the input parameters for the UDF require the user to enter information about the injected particles that has already been entered in the FLUENT GUI.

The weighting of the particles is done by assuming that the FLUENT-generated discrete uniform size distribution between d_{min} and d_{max} (again on a number of streams basis) provides enough resolution in particle size to accurately represent the Rosin-Rammler cumulative size distribution function shown in equation 4-7 where d is the particle size, D is the characteristic particle size parameter, and SF is the shape factor or spread parameter. Next the mass flow rate represented by a stream of a given particle size is assumed to be proportional to the value of the Rosin-Rammler probability density function equation 4-8 evaluated at that particle size with the constant of proportionality, S, given in equation 4-9, N is the total number of particle streams generated by FLUENT

at each timestep, and d_{min} and d_{max} are respectively the smallest and largest particle sizes used in the simulation. The mass represented by each particle stream then becomes the product of the weighting factor, S, the length of the simulation time step, Δt, and the PDF evaluated at the size of the particle stream in question.

$$Rosin - Rammler\ CDF = 1 - e^{-\left(\frac{d}{D}\right)^{SF}} \tag{4-7}$$

$$Rosin - Rammler\ PDF = \frac{d}{dd}CDF = \left(\frac{SF}{d}\right)\left(\frac{d}{D}\right)^{SF} e^{-\left(\frac{d}{D}\right)^{SF}} \tag{4-8}$$

$$Weighting\ Factor = S = \frac{\dot{m}_{injection}\left(d_{max} - d_{min}\right)}{N} \tag{4-9}$$

$$m_{particle}\left(d\right) = S \cdot \Delta t \cdot PDF\left(d\right) \tag{4-10}$$

5 Experimental Results

The results of the experiments are presented here; beginning with characterization of the fly ash then followed by mass measurements of the deposits formed under the various conditions. These results are then compared to model predictions.

5.1 Ash Measurements

To characterize the fly ash particles as they exit the reactor, measurements were made to determine the mass flux of particles and their size distribution to determine differences in fly ash characteristics for changes in operating conditions as well as to determine the repeatability of these measurements. All measurements were made with a 2.5 cm inside diameter by 3.8 cm outside diameter water-cooled fly ash collection probe that had been calibrated such that the suction rate of the probe could be matched to the flow rate of the exhaust gases to ensure isokinetic sampling of the particles. The resulting measurements showed that approximately 50% of the fly ash particles initially in the gas flow deposited on the walls of the reactor before they reached the reactor exit. No significant difference in either mass flux of particles or their size distribution was found between hot- and cold-wall or between oxidizing and reducing conditions.

5.1.1 Mass Flux

Mass flux measurements were made under the conditions of the various experimental runs; each taken after 1 hour of exposure time using a flow rate of 454 g/hr of coal. The ash analysis shown previously reports that the coal was 7.2% ash by weight. Using a 2.5 cm diameter probe, across a 15.2 cm diameter reactor for an hour, one would expect to collect .908 g of fly ash if none of the ash deposited on the reactor walls before reaching the exit. The five measurements taken, shown in   Table 5-1, had an average sample size of 0.453g indicating that, on average, 49.9% of the ash made it out of the reactor. Of the five measurements made, the smallest and largest samples were both taken under the cold oxidizing conditions indicating a low signal to noise ratio for estimating differences in mass flux between different operating conditions. For this reason the five measurements were taken as a single population from which the average mass flux used in collection efficiency calculations was used.

Table 5-1 - Table of measured fly ash collected under various reactor conditions.

	Mass Collected (g)	Fraction Transmitted
Cold Oxidizing "a"	0.4214	0.464
Cold Oxidizing "b"	0.4860	0.535
Hot Oxidizing	0.4252	0.468
Cold Reducing	0.4632	0.510
Hot Reducing	0.4682	0.516

5.1.2   Size Distribution

The size distributions of the fly ash samples were measured to determine what, if any, differences existed between the fly ash collected under the different conditions. The measured distributions shown in Figure 5-1 indicates that only small differences exist between the samples.
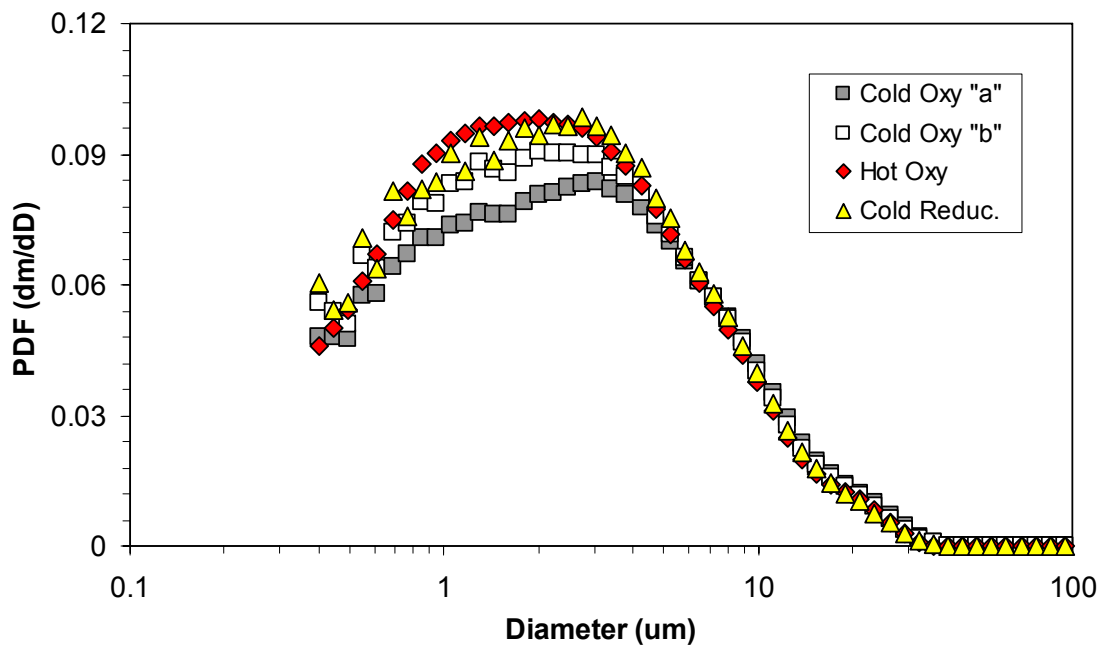

Figure 5-1 – Measured fly ash size distributions.

Two models were used in an attempt to predict the fly ash size distribution from the size distribution of the pulverized parent coal. The first model assumed that each coal particle began as a sphere with the density of the coal and formed a single spherical fly ash particle. The density of the fly ash was assumed to be a mass-weighted sum of the

density of its constituents. The second model made the same shape and density assumptions but instead predicted that each coal particle would fragment into equally-sized ash particles. The number of ash particles formed from a single char particle was assumed to be a function of initial char particle diameter for a given type of coal. This function, obtained empirically by Baxter (1992) is shown in Figure 5-2. Between these two models the fragmentation model predicted the measured fly ash size distribution much more closely than the non-fragmentation model as can be seen in Figure 5-3. However if the size distribution used in the simulation were obtained purely by predictive means using either model, the predicted impaction rate would be significantly affected. Either the predicted rate would be zero (fragmentation model predicts particles that are too small to impact the surface), or far too high (no-fragmentation assumption predicts distribution that yields much larger particles with order of magnitude higher impaction efficiencies). Using the measured size distribution solves the problem in this case and shifts the focus to other key Stokes number parameters including gas viscosity and freestream velocity. To further eliminate approximation errors the fly ash size distribution was treated as a piecewise-constant function which was multiplied by the FLUENT-based impaction efficiency, this product was numerically integrated to define overall impaction efficiency. The alternative approach of fitting the measured distribution with a rosin-rammler distribution function would not have been as precise as needed in this case.
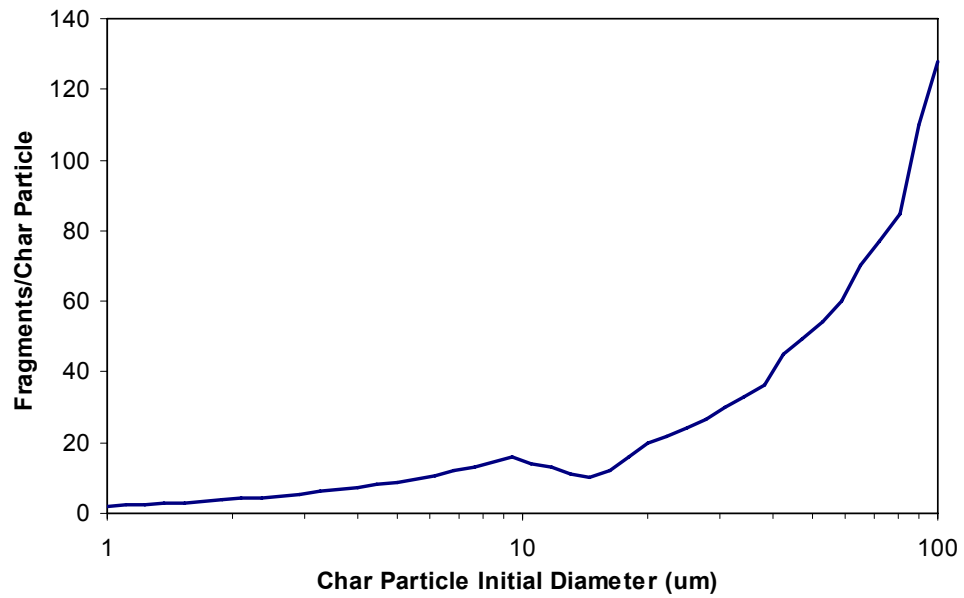
Figure 5-2 Number of fragments formed from a single char particle as a function of char particle initial diameter, as reported by Baxter (1992).
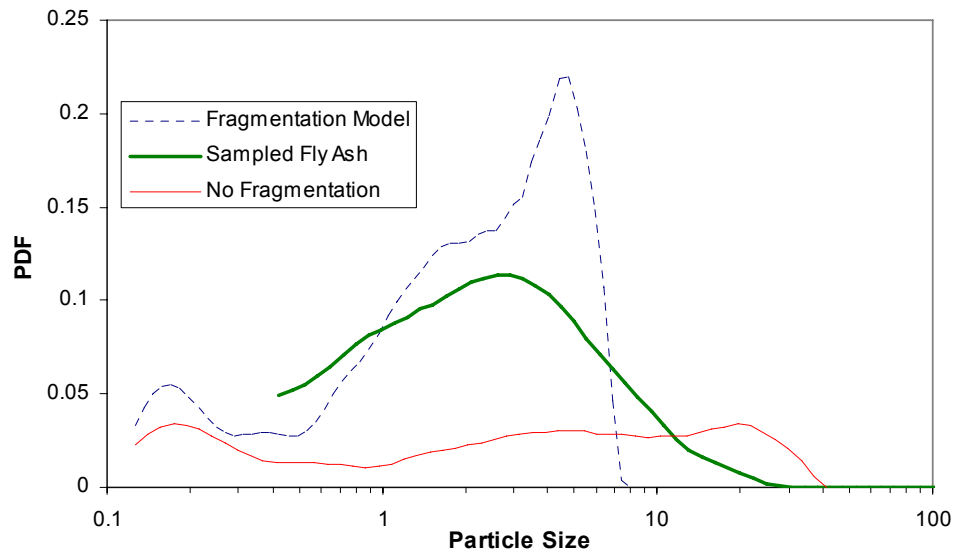

Figure 5-3 Comparison between measured and predicted fly ash size distributions using fragmentation and non-fragmentation models.

5.1.3   Selective Deposition

It was thought that the measured fly ash size distribution could possibly be predicted using the no-fragmentation model for fly ash formation by assuming that large particles were more likely to deposit on the reactor walls and thus never make it out of the reactor where they could be measured. However the predicted distributions produced under these assumptions could not reproduce the predicted measured size distribution.

5.2   Deposit Measurements

The deposit mass measurements which were made after the deposition probe had been exposed to the stream of fly ash and exhaust products for the previously-mentioned exposure times. The mass measurement was made by first removing the collection sleeve from the deposition probe. This was done very carefully so as not to disturb the delicate particulate and sintered deposit layers. The sleeve, with its still intact deposit was then weighed using a laboratory scale. The deposit was then carefully removed from the sleeve and collected. The sleeve was then cleaned with a dry towel to remove any leftover deposit, and then weighed again. This was done for both oxidizing and reducing conditions at two temperatures for each condition are shown in Figure 5-4. These data show similar deposition rates between the two oxidizing cases as well as between the two reducing cases. Unexpectedly, the reducing cases showed significantly lower, approximately one half, deposition rates than the oxidizing cases. When normalized, the overall collection rates of the deposits are between 2% and 6% of the total ash mass flux through the probe cross section over the time intervals tested.
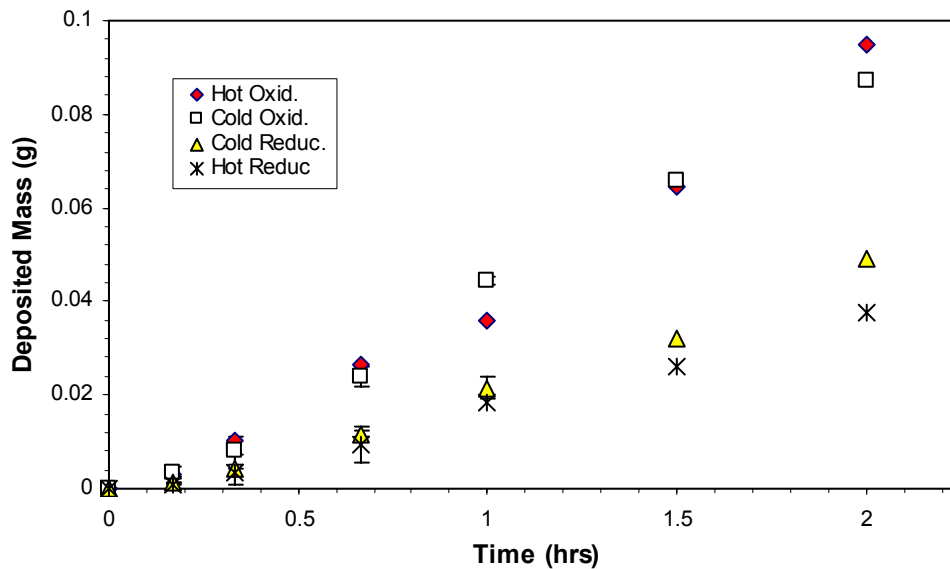
52

Figure 5-4 - Measurements of deposited mass as a function of probe exposure time for the various conditions. Error bars, where shown, indicate two standard deviations where runs were replicated.

The deposition rate from the same data are displayed in Figure 5-5, in grams per hour, where the ith deposition point was calculated using equation 5-1. These rates showed an upward trend over the first 40 minutes of exposure time indicating an increasing tendency for mass to deposit. This effect may be caused by the impaction surface softening slightly as the ash layer builds on the harder tube surface. Also of note is that each of the deposition rate curves follow a similar qualitative trend with time, that is the deposition rate increases fairly rapidly over the first approximately 40 minutes and then experiences a decreased deposition rate at some point between 40 and 90 minutes after which the deposition rate seems to flatten. The normalized deposited mass, shown in

Figure 5-6, is calculated by dividing the ith mass measurement by the product of ash mass flux through the projected probe cross-sectional area and the elapsed time until measurement i, as shown in equation 5-2. This method of plotting the data tends to

53

smooth out differences in deposition rate because total exposure time is used and an average deposition rate rather than an instantaneous deposition rate is reported. Each point represents the average deposition rate up to that time.

$$Deposition\ Rate = \dot{m}_i = \frac{m_i - m_{i-1}}{t_i - t_{i-1}}$$ (5-1)

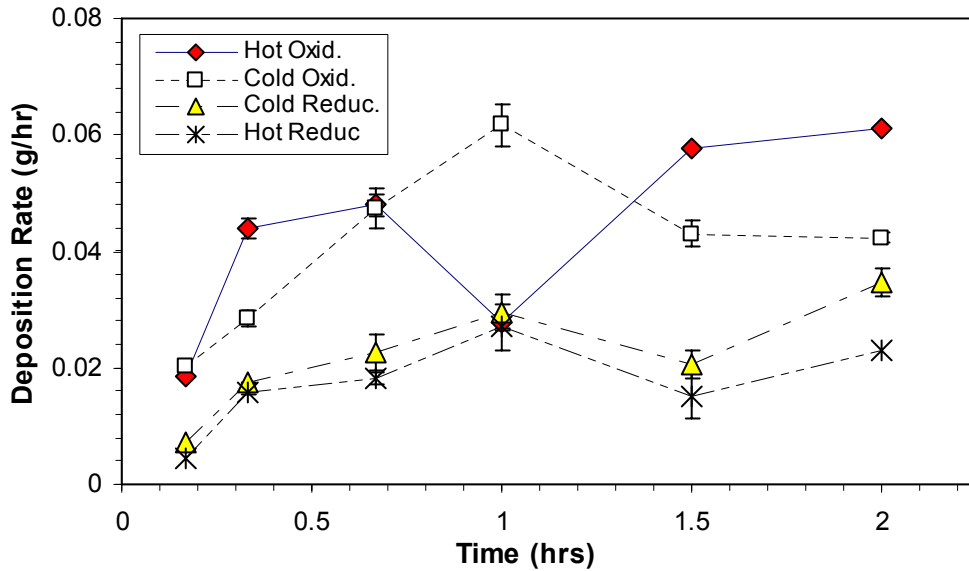$$Normalized\ Mass = (\eta G)_i = \frac{m_i}{\dot{m}'' A_{Pr\,obe} t_i}$$ (5-2)

Figure 5-5 - Deposition rate as function of time. Error bars, where shown, indicate the combined uncertainty of two standard deviations of each replicated, mass measurement.
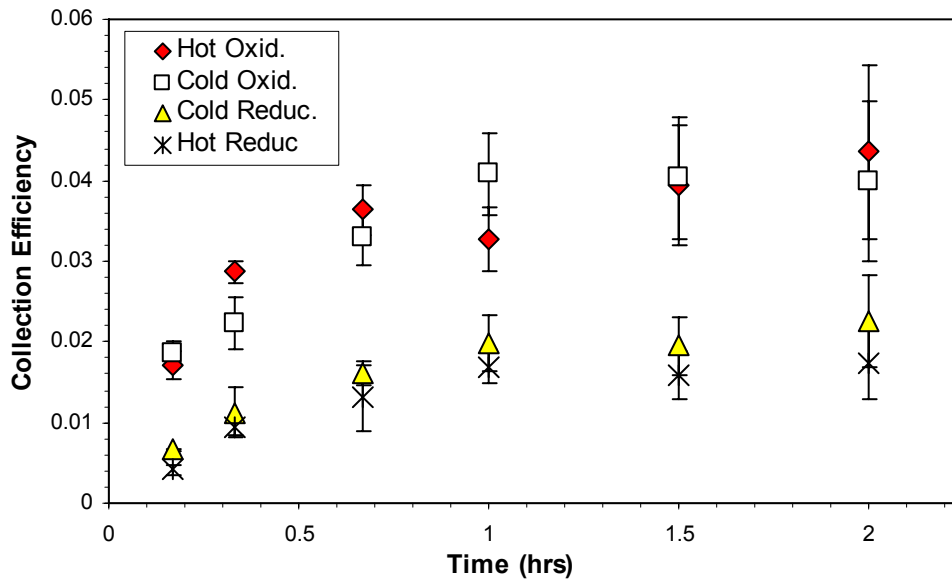
Figure 5-6 - Deposited mass vs. exposure time normalized to represent collection efficiency.

The similarity in deposition rates between the two oxidizing cases as well as between the two reducing cases, together with the difference between the oxidizing and reducing cases was not anticipated based on the size distributions or ash fusion temperatures of each case. The lower fusion temperatures of the ash under reducing conditions would normally predict a higher deposition rate even at similar temperatures due the higher capture efficiency associated with the softer, more fully melted particles. Even assuming perfect capture efficiency (all particle viscosities are below the critical viscosity), one might still expect a higher deposition rate in the reducing cases due to the higher velocities of the reducing cases due to higher mass flow rates and lower densities.

5.2.1 Deposit Sintering

At the end of each run the collected deposit was weighed and used to obtain a size distribution which was compared to the fly ash size distribution. In the case of the deposits produced under reducing conditions, not enough ash was collected to allow the size distribution to be measured. The resulting size distributions shown in Figure 5-7 showed particles that were much larger than the largest fly ash particles indicating possible sintering. Additionally, the deposits' size distributions appear to be bimodal from the simultaneous presence of sintered and unsintered particles, each with its own size distribution. Further the hotter deposit seems to show a more complete shift from the smaller, fly ash-like sizes to the larger, apparently sintered sizes.
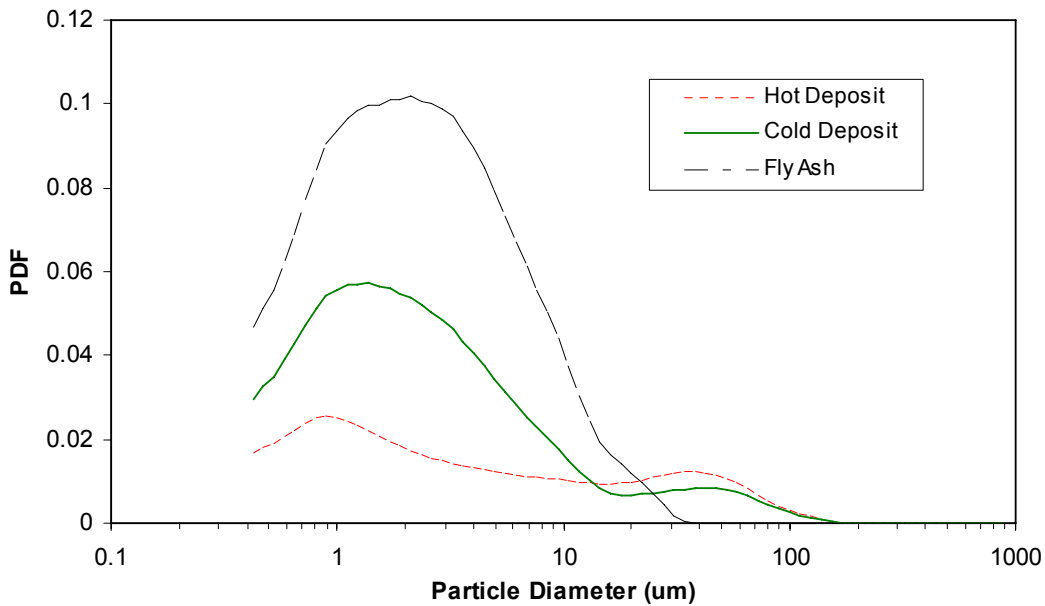
Figure 5-7 – Mass-based size distributions of deposits formed under oxidizing conditions compared to the fly ash size distribution.

5.3   Model Results

The modeling results were compared to the measurements in order to evaluate strengths and weaknesses of the model and to help interpret the data. The deposition model requires a critical viscosity to be input by the user. After initial calculations it could be seen that in order to produce a reasonable prediction, a large fraction of the particles impacting the surface would need to stick. The critical viscosity was therefore set high enough that all particles would stick. The value for critical viscosity used for the simulations, 10^4 Pa-s, is the same used by Huang et al. (1996) but could have been as low as 500 Pa-s without affecting the perfect capture efficiency assumption. First the results from these initial calculations will be shown, followed by a discussion and additional predictions.

5.3.1   Initial Model Results

Comparisons of initial modeling results to the measurements are shown in Figure 5-8 – Figure 5-11, with average collection efficiencies shown in Figure 5-12. These results calculated the gas phase viscosity based on the gas temperature of the FLUENT calculation.

The high critical viscosity forces the result of perfect capture efficiency which makes the predicted collection efficiency solely a function of impaction efficiency. The model showed good order-of-magnitude agreement with experimental measurements with this assumption. In general the simulation underpredicted deposition for the oxidizing cases. The model predicted slightly lower collection efficiency with higher temperature. This is because the temperature no longer impacted the capture efficiency

through softening of the particle because all particles impacting were sticking, but it did impact the Stokes number which affects impaction efficiency. As the gas temperature increases, its viscosity also increases (thus decreasing Stokes number) while the velocity simultaneously increases due to lower density (thus increasing Stokes number). The net effect is a small reduction in Stokes number and a small reduction in deposition rate with increasing free stream gas temperature. This trend of the model agreed well with the data in that neither oxidizing nor reducing conditions produced a significant change in deposition rate when temperature was increased. The model did not however capture the trend of significantly lower deposition rate seen in the reducing cases.
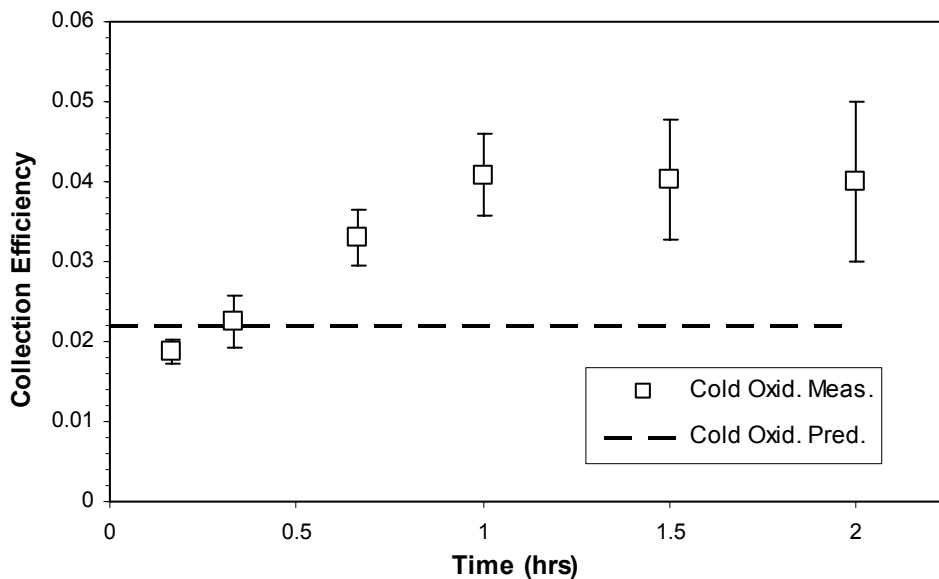
Figure 5-8 - Measured and predicted collection efficiencies for cold oxidizing case.
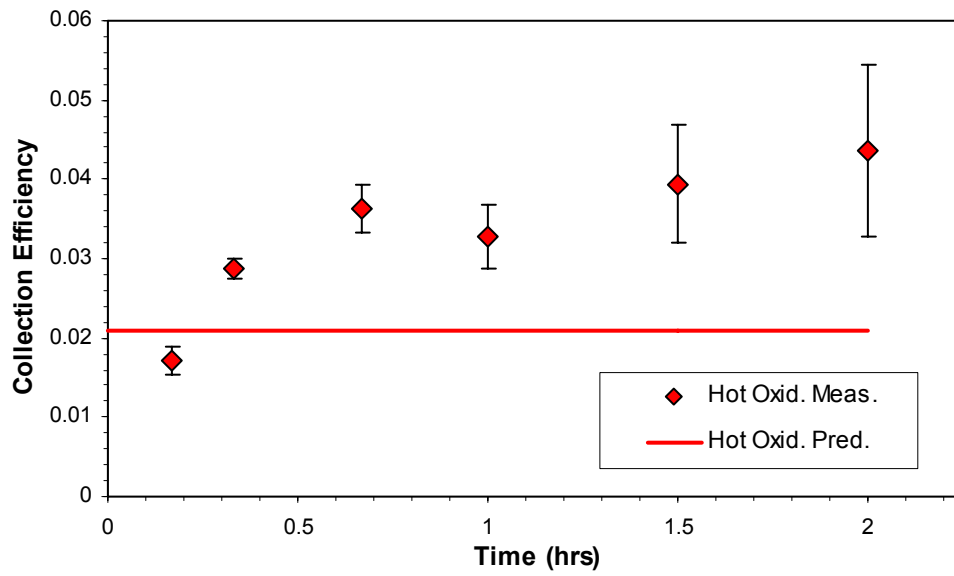
Figure 5-9 - Measured and predicted collection efficiency for the hot oxidizing case.
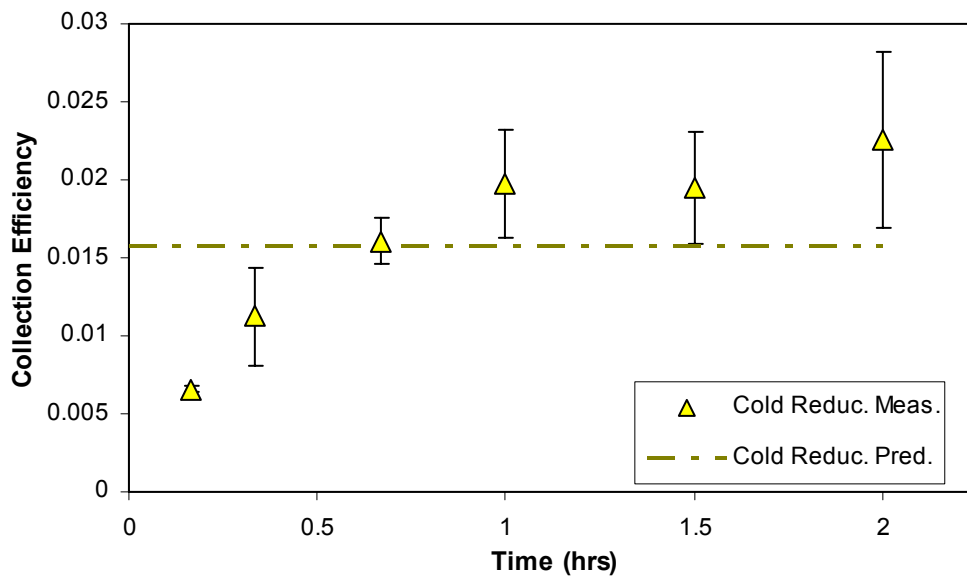
Figure 5-10 Measured and predicted collection efficiencies for the cold reducing case.
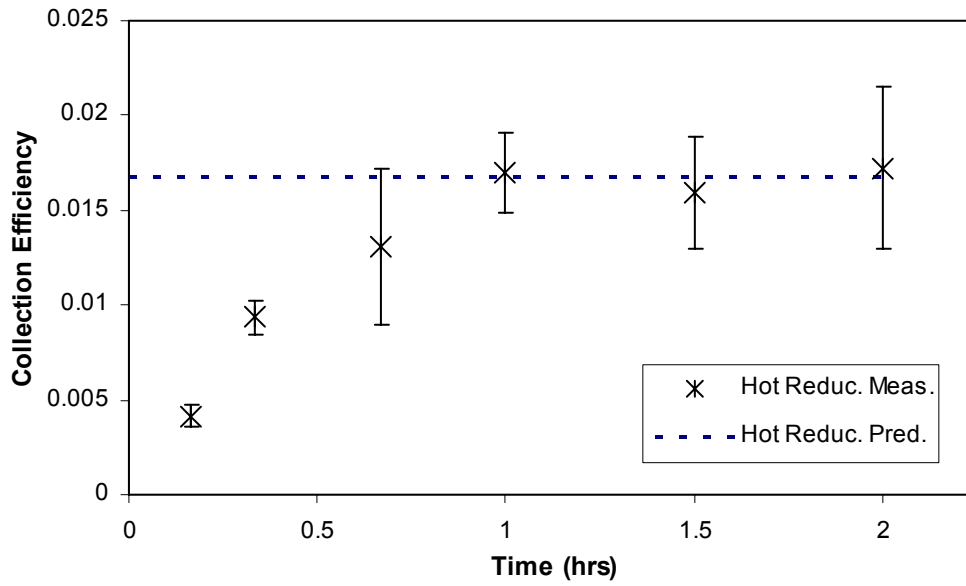
Figure 5-11 Measured and predicted collection efficiencies for the hot reducing case.
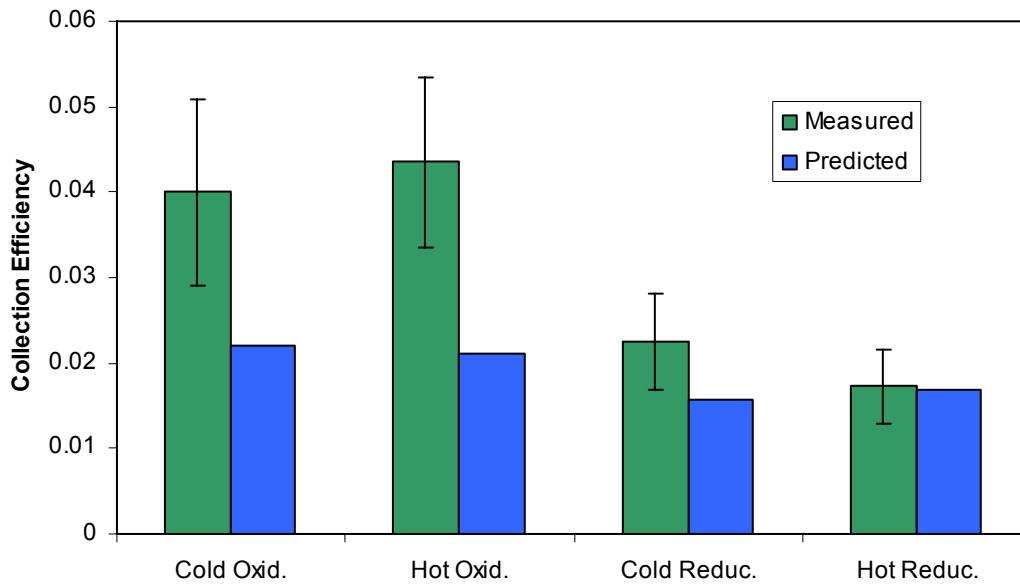

Figure 5-12 Measured and predicted collection efficiencies for a two-hour exposure time for all cases. Notice that the model does not predict the measured difference in deposition rates between the oxidizing and reducing cases.

5.3.2   Corrected Viscosity Results

It was hypothesized that the difference in measured deposition rates between the oxidizing and reducing conditions could be due to the hotter measured probe temperatures under reducing conditions. Since the hot combustion products leaving the reactor are exposed to room air as they are drawn into the reactor's exhaust system, a flame forms around the probe when the reactor is overall fuel-rich to produce reducing conditions. Thus the probe temperature was substantially higher for the reducing cases than the oxidizing cases. Thus the boundary layer temperature for the reducing case would have been higher which could have led to higher boundary layer viscosity without affecting the freestream temperature or velocity. Using the probe temperature to predict the viscosity used in the deposition simulation instead of the freestream temperature, showed improved agreement between model and measurement overall, and better captured the measured deposition rate difference between oxidizing and reducing cases.

Individual plots of predicted and deposited collection efficiencies as functions of time are shown below. Figure 5-13 shows the "cold" oxidizing case where the predicted collection efficiency is still somewhat lower than the measured efficiency. Figure 5-14 shows the "hot" oxidizing case which, after the initial 40-minute period shows good agreement between prediction and measurement. Figure 5-15, the cold reducing case, shows that the corrected viscosity prediction matches the measurement quite well after 60 minutes. The "hot" reducing case shown in Figure 5-16 still overpredicts the measurement after 120 minutes and is the only case that is actually shows a poorer match after the viscosity correction. In all cases the corrected temperature is lower than the FLUENT-predicted temperature which leads to a lower predicted viscosity, a higher

Stokes number and, in turn, a higher predicted deposition rate. A comparison of measured and predicted collection efficiencies after a 120-minute test is shown in Figure 5-17. In this figure it can be seen that the model is now capturing the trend of no or little change in deposition rate when free stream temperature is changed (hot and cold cases) and that the reducing conditions produce significantly lower deposition rates than the oxidizing condition. The model therefore appears to be useful in predicting trends and interpreting data.
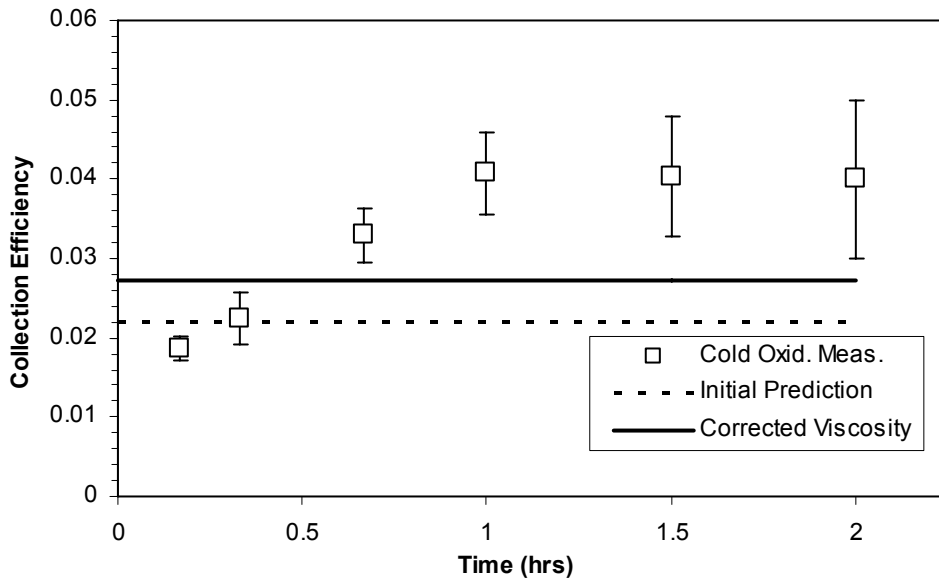
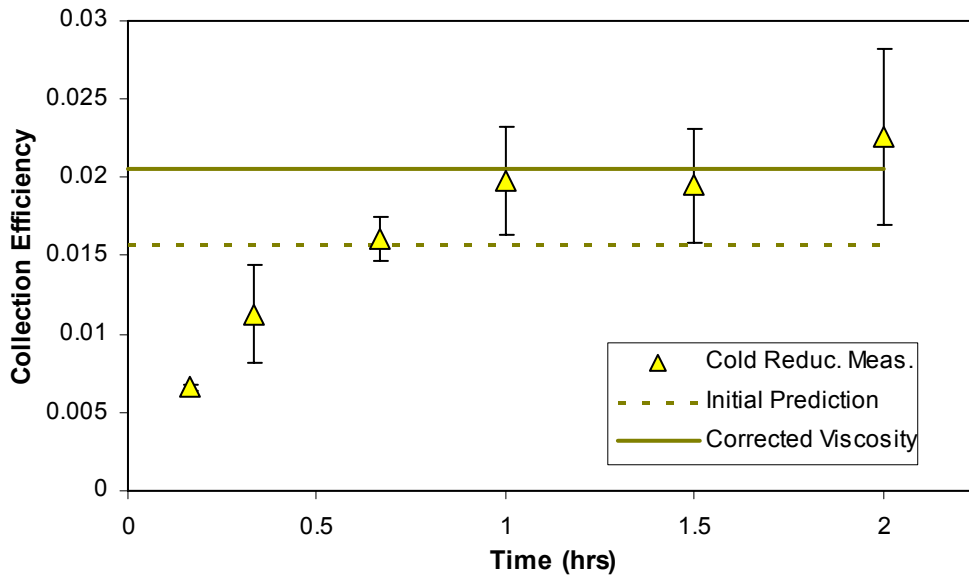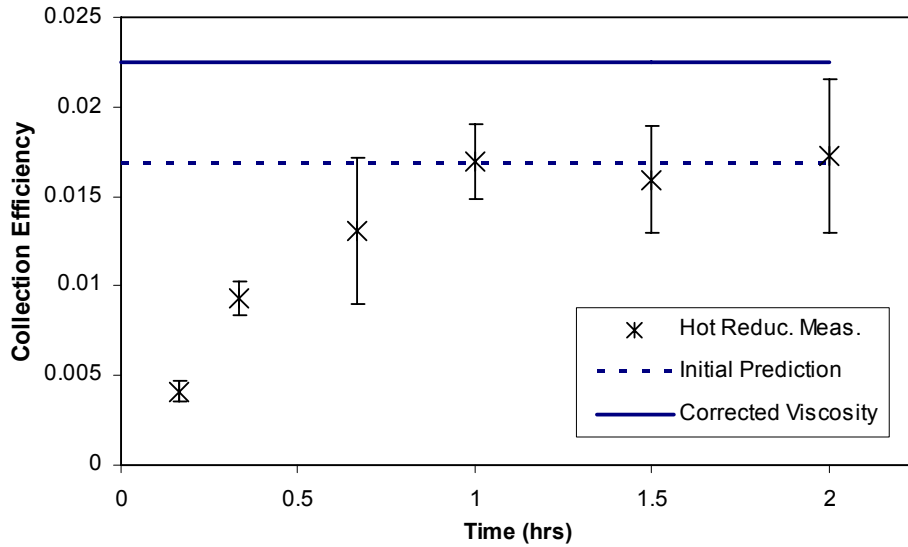**Figure 5-13 Comparison of predicted and measured collection efficiencies for the deposit formed under oxidizing conditions and colder temperatures. Notice that the measured collection efficiency exceeds the predicted collection efficiency, even assuming perfect capture efficiency. This may be the result of underpredicting the impaction efficiency.**
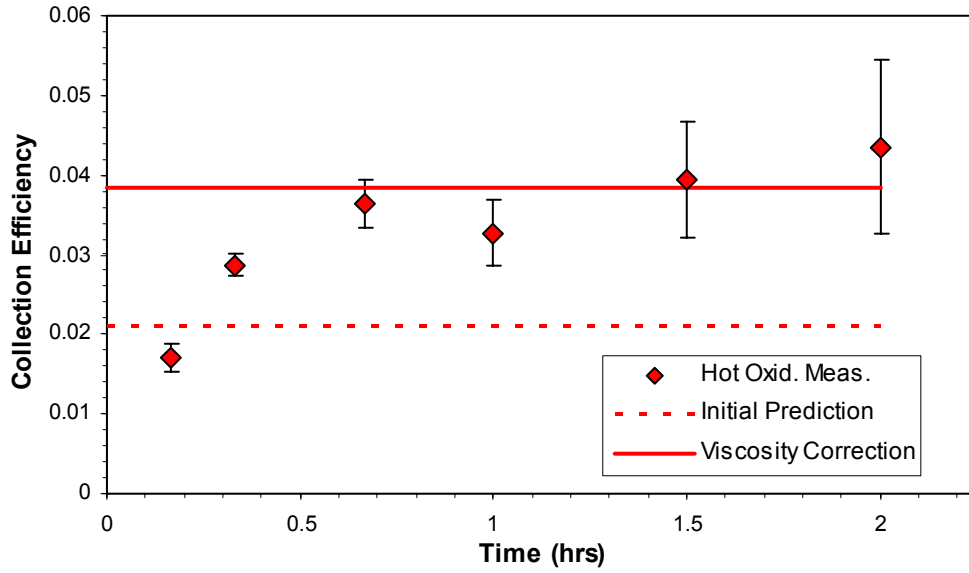
Figure 5-14 Comparison of predicted and measured collection efficiencies for the deposit formed under oxidizing conditions and hotter temperatures.

Figure 5-15 Comparison of predicted and measured collection efficiencies for the deposit formed under reducing conditions and colder temperatures.

Figure 5-16 Comparison of predicted and measured collection efficiencies for the deposit formed under reducing conditions and hotter temperatures.
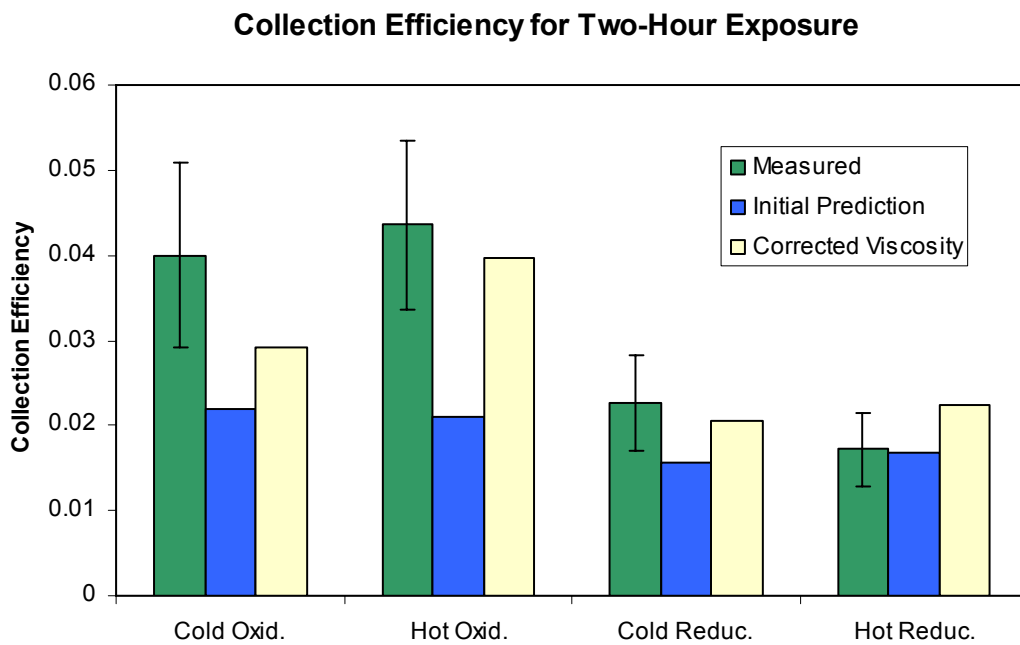
Figure 5-17 Measured and predicted collection efficiency for a two-hour exposure.

5.3.3   Sensitivity Analysis

The deposition model's sensitivity to particle size and probe and gas temperature was analyzed by noting the net collection efficiency change due to small perturbations in the independent variable of interest. The results of showed that the deposition rate is very sensitive to errors in particle size and the deposition rate is also sensitive to temperature changes, although the temperature effect is much less pronounced. All sensitivity analysis results make use of the cold oxidizing case a reference and make use of the perfect capture efficiency assumption.

As will be discussed later, impaction efficiency is strongly related to particle size. This relation showed that a 5.5% shift of the fly ash size distribution, from a mass mean particle diameter of 10.1 μm down to 9.52 μm, changed the predicted mass impaction efficiency by 9.9% from .0271 to .0247.

Changes in probe temperature change the calculated viscosity for the flow field. A 50 degree increase in probe temperature from 890 K to 940 K changed the calculated viscosity from 4.04E-5 Pa-s to 4.2E-5 Pa-S. This viscosity increase lowered the Stokes number of the simulated fly ash particles and caused a corresponding 4.6% decrease in predicted collection efficiency from .0271 to .0259.

Changes in flow temperature also affect the impaction efficiency due to the velocity change that accompanies the temperature-caused density change. To measure the sensitivity of collection efficiency to this parameter, the gas temperature was increased by 50 degrees from 1576 K to 1626 K. This changed the density from .178 kg/m^3 to .173 kg/m^3 and the velocity from 1.79 m/s to 1.85 m/s. The net of effect of the gas temperature change was to increase the predicted collection rate by 2.7% from .0271 to .0283.

5.3.4   Transient Deposit Growth

The ash layer thickness, the probe surface temperature, and the wall heat flux were all tracked as functions of space and time. The accompanying increased surface temperature and decreased heat flux were tracked as functions of location on the probe and time. Since the experimental results collected deposits for a relatively short time compared to an actual superheater tube, these model effects were of minimal importance in determining the measured deposition behavior. They are discussed here for a more complete description of the model.

The model predicts an ash layer thickness that is roughly parabolic in shape extending roughly 60 degrees to either side of the stagnation point as can be seen in Figure 5-18. Also notable is the fact that asymmetries exist across the two halves of the probe as defined by the stagnation point. These asymmetries exist due to the noisy nature of the random-walk model with a finite number of particle tracks. By modeling the entire circumference of the probe instead of just half (which would have required the assumption of symmetry), the magnitude of the asymmetry between the two side of the probe could be used to quantify the amount of uncertainty in the model's deposition behavior. The predicted surface temperature profiles around the circumference of the probe both as a clean probe as well as after a 2-hour exposure are shown in Figure 5-19. This temperature profile exhibits a much smoother shape than the deposit thickness profile due to the convective boundary providing some layer of smoothing between faces. The average surface temperature as a function of time is shown in Figure 5-20.
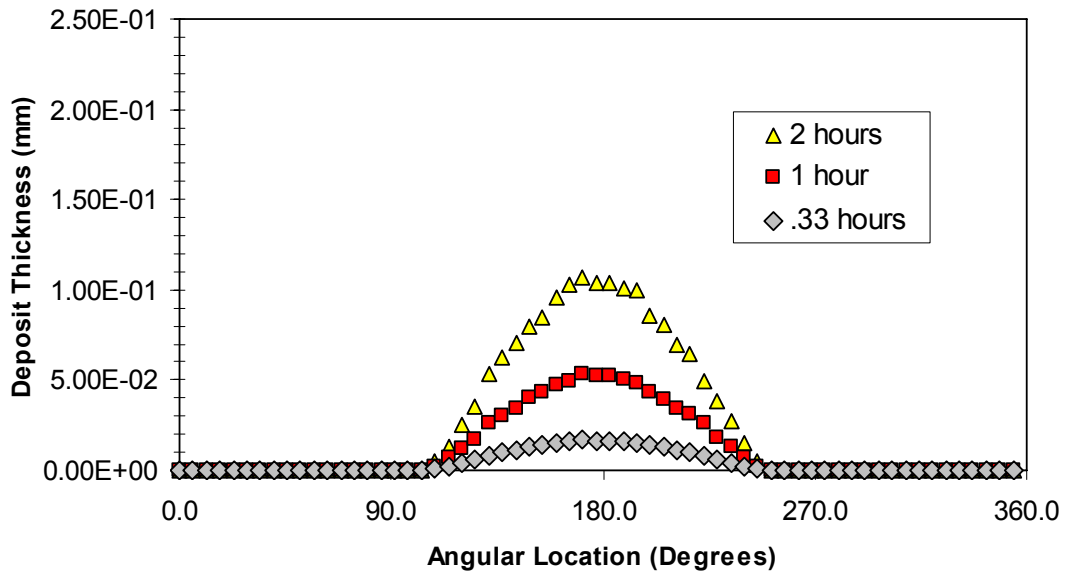
Figure 5-18 Plot of predicted ash layer thickness against angular location on the probe after three different exposure times. Note that 180 degrees corresponds to the stagnation point.
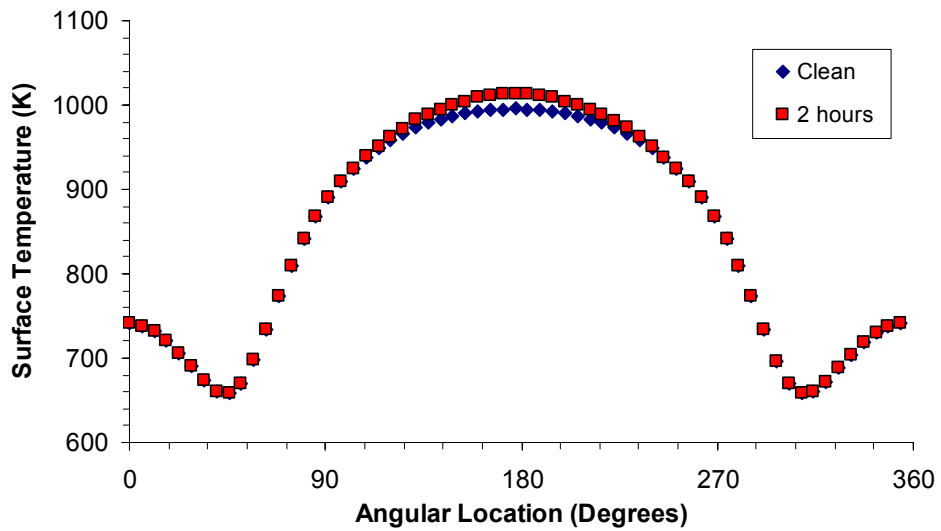

Figure 5-19 Plot of predicted surface temperature profile around the circumference of the probe for clean wall and 2-hour exposure cases.
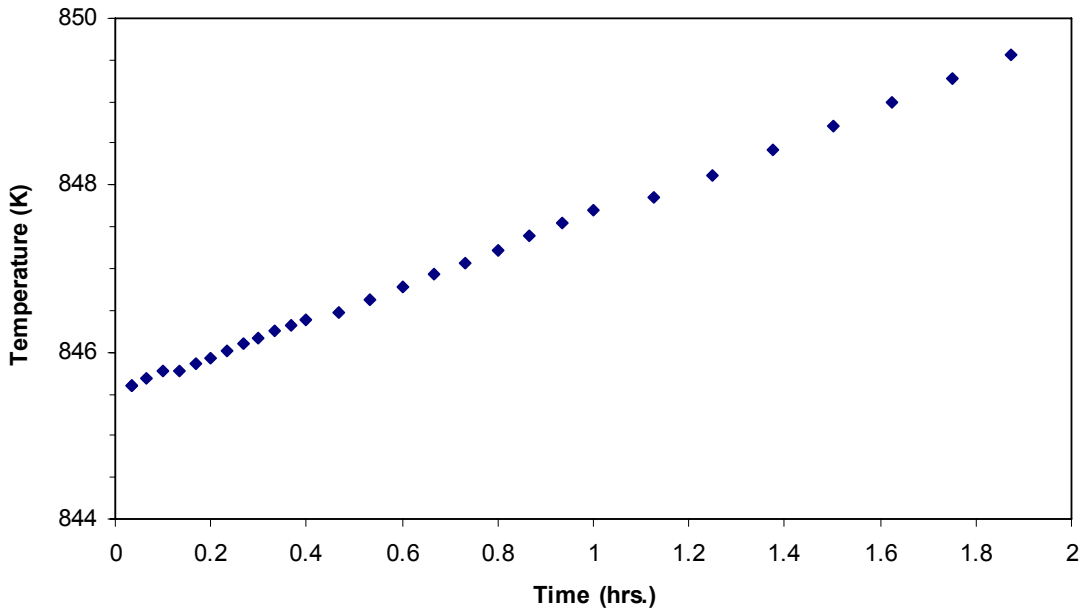
Figure 5-20 Plot of predicted average surface temperature over time over the course of a 2-hour test. Note that the overall average surface temperature change is less that five degrees Celsius.

5.3.5   Impact Characteristics

To facilitate easier implementation of future capture models, the impaction/capture UDF in FLUENT currently tracks most of the important variables that might be used in such models even though some are not currently used. These include particle velocity at impact, particle temperature at impact, and angle of impaction. Figure 5-21 shows the normalized values of some of these variables plotted against Stokes number. These allow for a better conceptual understanding of how conditions at impact change with particle Stokes number. Curve-fits to Plots like these could be used for faster model development by allowing impaction characteristics to be calculated without the added complexity of CFD simulation of particle trajectories.
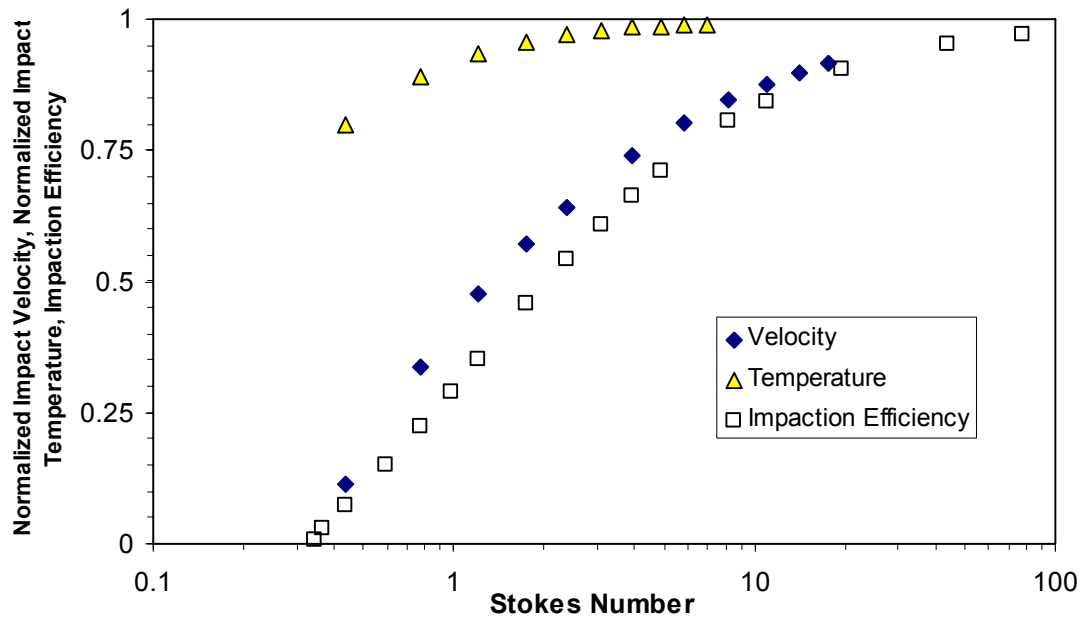
Figure 5-21 Plot of particle properties at impact as functions of Stokes number for a typical fly ash particle as tracked by the Fluent-based UDF.

6   Discussion

The results shown in the previous section are discussed in this section including the effects of particles size distribution and in particular its formation and collection.

6.1   Viscous Effects

Under the perfect capture assumption the particle impaction efficiency becomes very important in predicting deposition behavior. As mentioned in the introduction, the impaction efficiency relation developed by Israel and Rosner was based on a potential (inviscid) flow field. To determine the effect of a viscous flowfield surrounding the cylinder, two flowfields were generated in Fluent; one inviscid, one viscous. It was observed that predicted impaction efficiencies using the FLUENT-generated inviscid case matched the Israel relation very closely. This simulation had to be done in two steps to simultaneously solve Stokesian drag force on the particles (dominated by viscous drag) in a flowfield that neglects viscosity altogether. The first step consisted of obtaining a converged solution in FLUENT using the inviscid viscosity. The viscosity model was then switched back to the laminar model and particles were injected into the domain without further solving the transport equations. The impaction efficiencies for the viscous case were somewhat lower than the inviscid. At high Stokes numbers the difference between the two cases was negligible however at lower stokes numbers the difference is

quite significant. As seen in Figure 6-1, the inviscid case appears to asymptote to zero where the viscous case shows a clear zero point below which no particle will impact. The predicted deposition rates would have been about 80% larger had the Israel relation been used instead of tracking the particles individually in the viscous flow field using the random-walk model. This effect can be seen more clearly in Figure 6-2, where particle size distribution and impaction efficiency are plotted as a function of particle diameter. The figure shows that the region where both size distribution and impaction are greater than zero increases significantly when the impaction efficiency is determined by the inviscid flow solution.
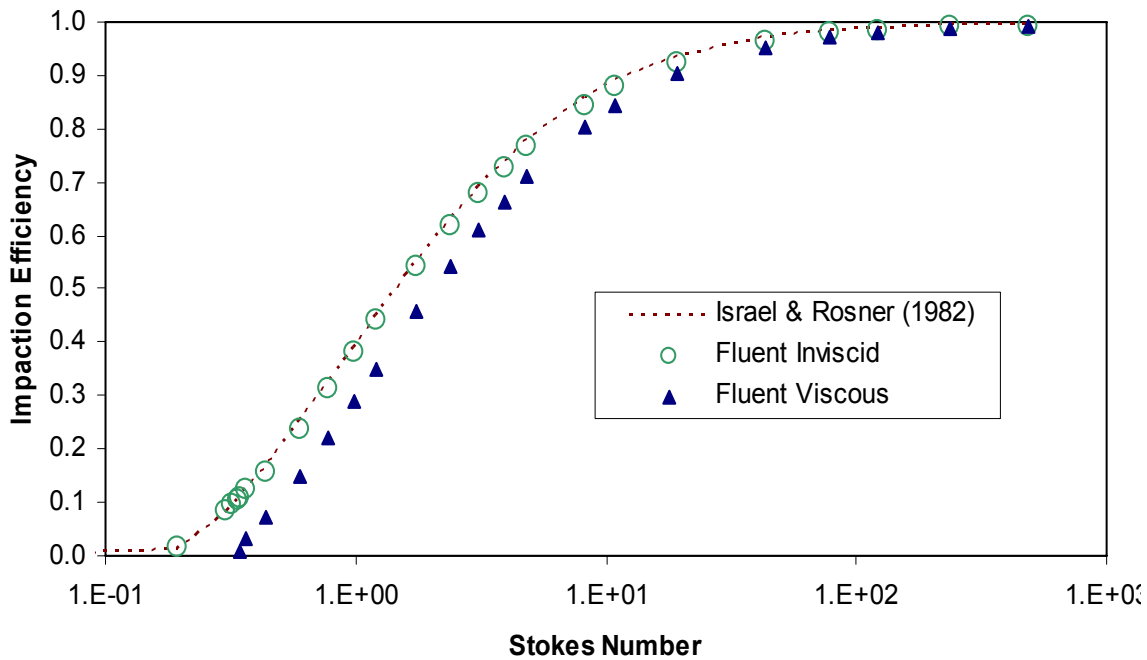
Figure 6-1 - Impaction efficiencies for invscid and viscous flow fields.
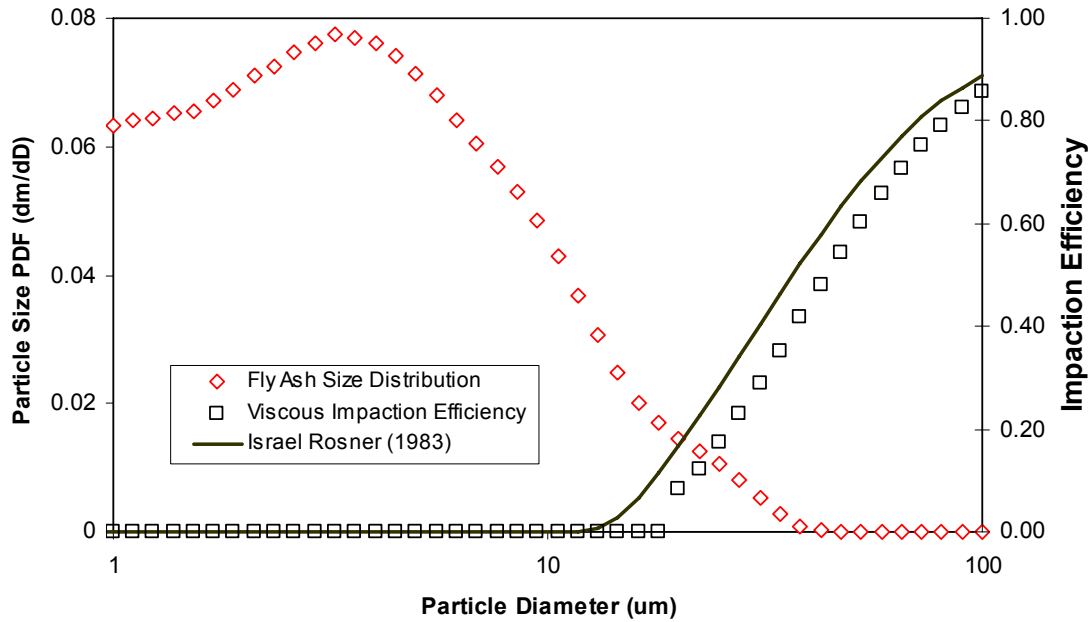
Figure 6-2 Superimposed plots of fly ash size distribution and impaction efficiency against particle diameter. Notice the majority of the particle mass is too small to deposit by inertial impaction. Using Israel's potential-flow-based relation would yield an 80% mass increase in impaction rate for the case shown here (cold oxidizing).

6.1.1   Eddy Impaction

Given the number of small particles in the fly ash and the low overall collection efficiency, further improvements to the predicted deposition rate might be realized by attempting to model eddy impaction. Eddy impaction modeling would depend heavily on being able to reliably predict the nature of the turbulent flow field surrounding the deposition probe. A brief survey of the two-equation turbulence models available in FLUENT showed large variations in the predicted turbulence intensity surrounding the probe, both in location and magnitude. One of these models (k, ε) predicted peak

turbulence intensities greater than 100% under certain conditions; while this seems far too high to be realistic this flow field does exhibit some signs of eddy impaction when used with the random-walk model. As shown in Figure 6-3, at low Stokes numbers this high turbulence flow field showed impaction efficiencies much higher than in the low turbulence case. The high turbulence field showed impaction even where the low turbulence field showed zero. To account for eddy impaction effects, an accurate description of the turbulent flow field, and particularly the boundary layer surrounding the probe would need to be produced.
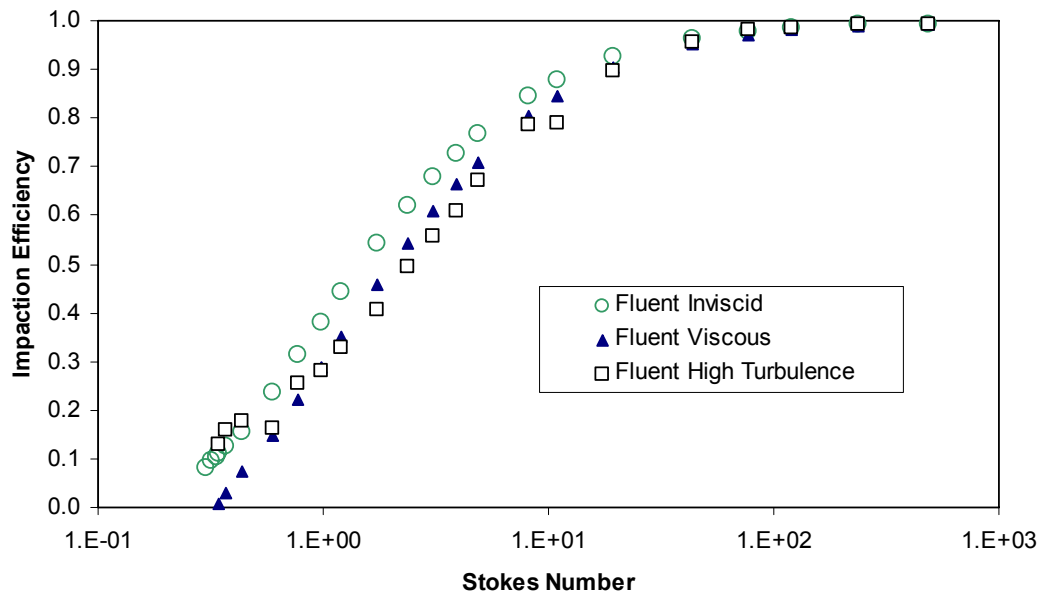
Figure 6-3 Impaction efficiencies for three flowfields in generated in Fluent. Notice that at low Stokes numbers the high turbulence flowfield exhibits signs of eddy impaction that are not predicted by the lower turbulence field.

74

6.1.2 Erosion

The Walsh capture model originally included an erosion model that predicted a mass removal rate of a particulate layer. This erosion model would not explain the lower measured deposition rate under reducing conditions measured as it predicts the erosion rate to be linear with mass flux of particles (i.e. total mass of particles per unit area per unit time) which was measured to be approximately constant throughout the range of experiments reported here. If erosion is the determining factor in the lower deposition rates observed under reducing conditions, a more sophisticated model would be needed to describe it.

6.1.3 Initial Layer Formation

Each plot of deposition rate with time showed an increasing deposition rate over the first 40 minutes of exposure time. This effect, which was not captured by the model, may be explained by the formation of an initial layer formed by condensation and/or small particle deposition due to eddy impaction or thermophoretic forces. Since this layer would appear to form in a short time relative to the total collection time of an ash deposit, it would appear to be of secondary interest at this time.

7   Summary and Conclusions

Following is a summary of accomplishments and conclusion that can be drawn from the work presented. A down-fired, electrically heated, pulverized coal reactor was assembled based on the design and procurement of previous students. The assembly involved the design of heat shielding and the management of electrical connections. A gas-fired preheater section was designed, fabricated and assembled. The reactor was tested to determine operating characteristics and identify problems. Issues resolved on the reactor included: 1. Installation of larger electrical connectors between the heaters and low gage wiring to reduce overheating of the connection. 2. Iterations on the fuel feed system to reduce clogging increase flow rate. 3. The implementation of a premixed natural gas jet mixture into the reactor to produce a non-sooting reducing zone, and 4. Documentation of the reactor components.

The reactor was used to collect fly ash mass flux and mass deposition measurements of a tube in cross flow. A sampling probe was calibrated to produce isokinetic flow for sampling. Measurements of fly ash mass flux, fly ash size distribution, mass of deposit and deposit size distribution were obtained at two oxidizing and two reducing conditions and two temperatures.

A FLUENT-based deposition model was produced that predicted the impaction effieciency and deposition rate. This model was and then combined with sub-models

written by other team members for ash deposit thickness, conductivity, and emittance to produce an ash deposition model containing four UDFs. The model has been demonstrated to produce converged results and documented for future development. The model results were compared with deposition measurements.

The following conclusions can be drawn from the modeling and measurement results.

1. Fly ash size distributions for the oxidizing and reducing conditions burning Illinois # 6 coal were the same within measurement uncertainty.

2. The measured fly ash flux showed that approximately half of the coal ash is depositing on walls prior to reaching the bottom of the reactor.

3. The fly ash size distribution demonstrates signs of particle fragmentation for which the mean size was relatively well predicted by literature correlations.

4. The deposition of fly ash is highly sensitive to size distribution and although mean size was well predicted by correlations, the measured size distribution, in particular the largest sizes in the distribution were needed to explain the measured deposition rate.

5. For the measured conditions, all fly ash appeared to be above the temperature required to produce the critical viscosity and the capture efficiency was near unity. The capture efficiency was not a function of temperature and collection efficiency was dominated by impaction efficiency.

6. The model was not adequately tested over a wide range of conditions, particularly with data related to conditions which would produce a variation in capture

efficiency. The viscosity and capture efficiency components of the model remain untested.

7. The impaction efficiency predicted by the model agrees well with previously published inviscid flow solutions and with the data when the capture efficiency is assumed to be one.

8. The model was useful in evaluating the combined effects of gas temperature on viscosity, density, particle temperature and particle velocity which led to improved understanding of deposition. Specifically, the idea of basing the Stokes number on the deposit surface temperature or a film temperature rather than the free stream temperature was identified.

7.1 Future Work

To improve upon the ability of the model to predict measured trends in deposition behavior additional experiments are required that investigate non-perfect capture efficiency when the fly ash particle temperatures are in the melting range of the particles to determine either the proper value for the critical viscosity in the Walsh capture model or whether a new model is needed altogether. Additional work may be required to determine the relative importance of eddy impaction to inertial impaction and whether or not this can be adequately modeled in FLUENT without prohibitive computational expense. Significant gains could also be made if the step of measuring the fly ash size distribution could be skipped by using a fragmentation model instead. Additionally, predicting the amount of ash mass captured by the reactor itself may also prove instructive.

8 References

[1]   Baxter, L.L., (1992) "Char Fragmentation and Fly Ash Formation During Pulverized-Coal Combustion." Combustion and Flame 90: 174-184

[2]   Baxter, L.L., (2000) "A Comprehensive Summary of Research Conducted at Sandia's Combustion Research Facility – Final Report" Sandia National Laboratory, CA: Livermore. 92-118

[3]   Browning G.J., Bryant G.W., Hurst H.J., Lucas J.A., Wall T.F. (2003) "An Empirical Method for the Prediction of Coal Ash Slag Viscosity." Energy & Fuels. 17:731-737

[4]   Chen, C., Horio, M., Kojima, T., (2001) "Use of Numerical Modeling in the Design and Scale-Up of Entrained Flow Coal Gasifiers." Fuel 80: 1513-1523

[5]   Cundick, D.P., Blanchard, R.P., Maynes, D., Tree, D., Baxter, L.L., (2007) "Thermal Transport to a Reactor Wall with a Time Varying Ash Layer." 5th US Combustion Meeting, San Diego, CA, USA.

[6]   FLUENT 6.2 User's Guide. Fluent Inc,. Centerra Resource Park, 10 Cavendish Court, Lebanon, NH 03766, January 2005.

[7]   Huang, L.Y., Norman, J.S., Pourkashanian, M., Williams, A., (1996) "Prediction of Ash Deposition on Superheater Tubes from Pulverized Coal Combustion." Fuel 75:3 271-279

[8]   Hurst, H.J., Patterson, J.H., Quintanar, A., (2000) "Viscosity Measurements and Empirical Predictions for Some Model Gasifier Slags - II" Fuel 79: 1797-1799

[9]   Israel, R. and Rosner, D. E. (1982) 'Use of a Generalized Stokes Number to Determine the Aerodynamic Capture Efficiency of Non-Stokesian Particles from a Compressible Gas Flow', Aerosol Science and Technology, 2:1, 45 -51

[10]   Kær, S.K., Rosendahl L.A., Baxter L.L. (2005). "Towards a CFD-based mechanistic deposit formation model for straw-fired boilers." Fuel. 84: 833-848

[11]   Kondratiev, A., Jak, E., (2001) "Predicting Coal Ash Slag Flow Characteristics (Viscosity Model for the Al_2O_3-CaO-'FeO'-SiO_2 System)" Fuel 80: 1989-2000

[12]   Li, A., Ahmadi, G., (1993) "Computer Simulation of Deposition of Aerosols in a Turbulent Channel Flow with Rough Walls." Aerosol Science and Technology 18:1, 11-24

[13]   Lokare, S.S., (2003) "Investigation of Ash Deposition and Corrosion Mechanisms in Combustion of Bio-Fuels and Fuel Blends in a Pilot Scale Facility." MS Thesis. Brigham Young University.

[14]   Masia, A.A.T., Buhre, B.J.P., Gupta, R.P., Wall, T.F., (2007) "Use of Thermo-Mechanical Analysis to Predict Deposition Behaviour of Biomass Fuels." Fuel (2007) 86: 2446-2456

[15]   Rushdi, A., Sharma, A., Gupta, R., (2004) "An Experimental Study of the Effect of Coal Blending on Ash Deposition." Fuel 83: 495-506

[16]   Rushdi, A., Gupta, R., Sharma, A., Holcombe, D., (2005) "Mechanistic Prediction of Ash Deposition in a Pilot-Scale Test Facility." Fuel 84: 1246-1258

[17]   Syred, N., Kurniawan, K., Griffiths, T., Gralton, T., Ray. R., (2007) "Development of Fragmentation Models for Solid Fuel Combustion and Gasification as Subroutines for Inclusion in CFD Codes." Fuel. 86: 2221-2231

[18]   Urbain, G., Cambier, F., Deletter, M., (1981) "Viscosity of Silicate Melts" British Ceramic Society 80:139-141

[19]   Vargas, S., Frandsen, F.J., Dam-Johansen, K., (1999) "Rheological Properties of High-Temperature Melts of Coal Ashes and Other Silicates." Progress in Energy and Combustion Science 27: 237-429

[20]   Walsh, P.M., Sayre, A.N., Loehden, D.O., Monroe, L.S., Beer, J.M., Sarofim, A.F., (1990) "Deposition of Bituminous Coal Ash on an Isolated Heat Exchanger Tube: Effects of Coal Properties on Deposit Growth." Progress in Energy and Combustion Science 16: 327-346

[21]   Watt, J.D., Fereday, F., (1969) "The Flow Properties of Slags Formed from the Ashes of British Coals: Part 1 Viscosity of Homogeneous Liquid Slags in Relation to Slag Composition" Journal of the Institute of Fuel 42: 99-103

[22]   Zhou, H., Jensen, P.A., Flemming, J.F. (2006) "Dynamic Mechanistic Model of Superheater Deposit Growth and Shedding in a Biomass Fired Grate Boiler." Fuel. 86:1519-1533

Appendix A. Reactor Information

A.1 Reactor Construction and Operation

Construction work on the new multi-fuel reactor has seen the coal-feeding, plumbing, air-preheating, and electrical systems transition from initial design stages through to installation, shakedown, and fully online.

A.2 Downtubes, Access Tubes, and Support Plates

The reactor's downtubes, access tubes, and support plates are all made of silicon carbide and are manufactured by Norton Saint-Gobain through our independent contact Bill Bolt. Bill Bolt can be contacted at:

P.O. Box 718
12621 Hwy 105 West
Suite 301
Conroe, TX 77305-0718
(936) 539-2552
(936) 539-2548 fax

Each of the main reactor tubes feature three collars, two with holes for accepting access tubes and one without holes that mate with the support plates. The original design called for these collars being bonded to the main tube before being installed however this

design has been replaced by the entire main tube including collars being cast as a single unit. The main tube is held in place by four support plates that are built up in two overlapping layers of two plates each. During installation the main tube is held in place while the support plates are slid into position under the uppermost collar, after the support plates are installed the access tubes may be installed.
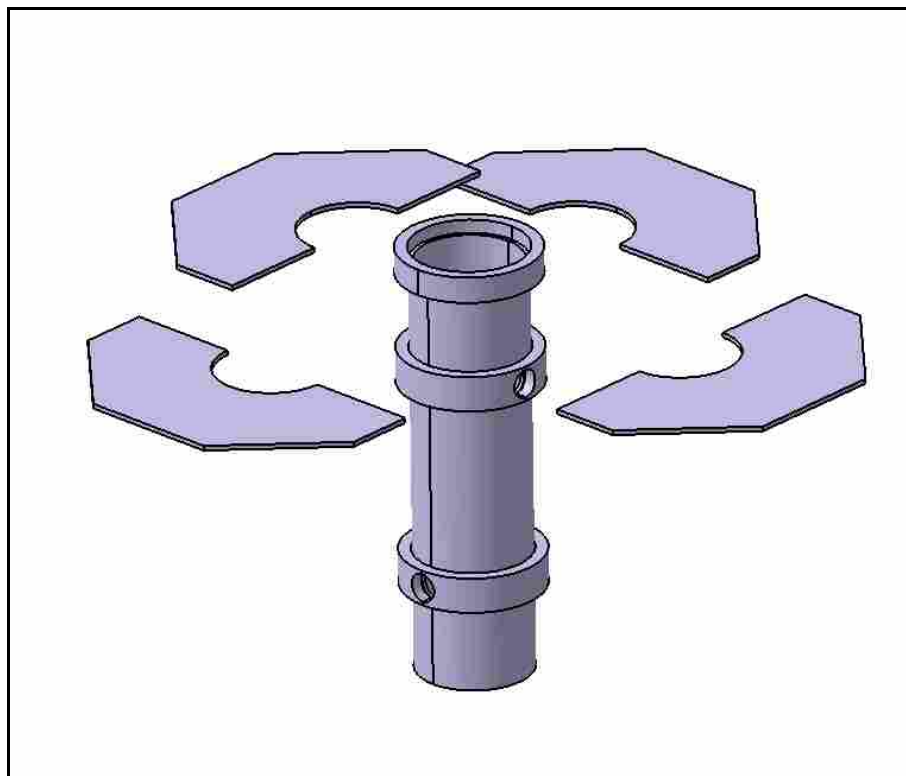
Figure A-1 Exploded view of the main reactor tube with support plates.
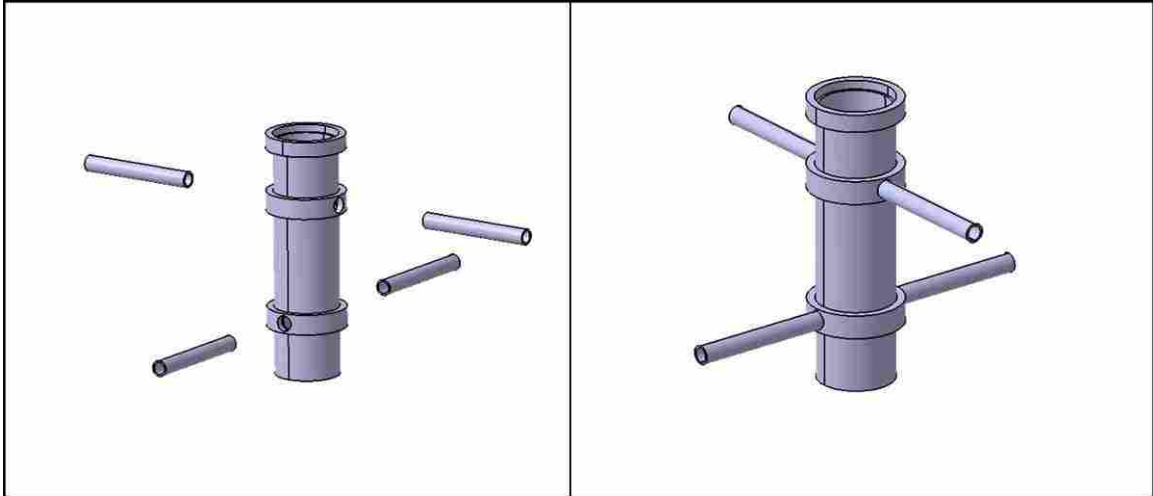
Figure A-2 Exploded and assembled views of the main reactor tube with its four access tubes.
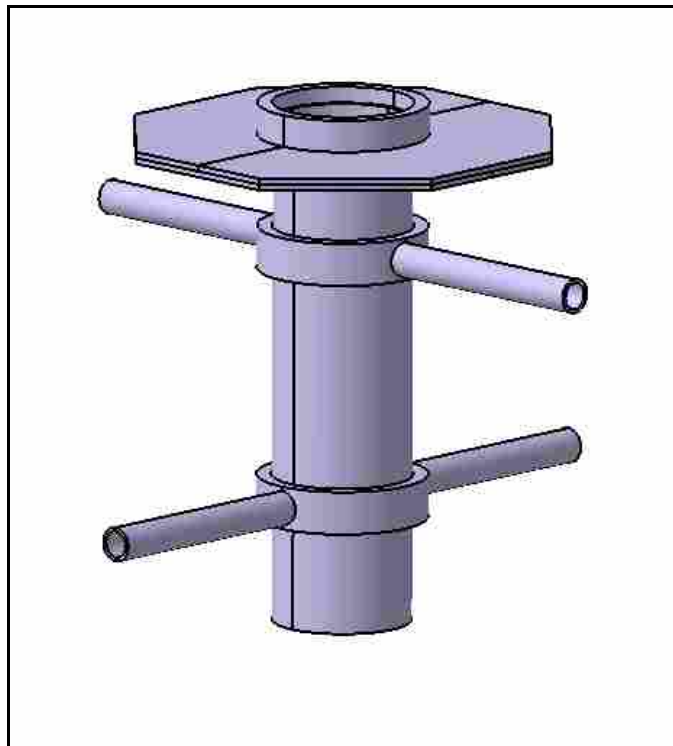
Figure A-3 Assembled silicon carbide components including the main reactor tube, support plates, and access tubes.

A.3 Insulation

The reactor's insulation comes in two forms, rigid panels and soft blankets both are made by Thermal Ceramics and were ordered from Mountain View Power and Industrial. The rigid panels are cut into various shapes and sizes to form the majority of the reactor's insulation, the blanket is used in various locations to add additional insulation around access tubes, around the edges of the support plates, and on top of each section's support plates. The insulation panels are used in two locations, the first is to form the bulk of the insulation between the main reactor tubes and the lab, panels are cut into a series of shapes that are assembled to form layers that surround the main reactor tubes and define an air gap inside of which the electrical heaters are located. The panel-type insulation is also used to insulate the support plates from the reactor's steel frame, this is done by cutting the panels into a number of identical blocks that are arranged to insulate the steel frame from the support plates.
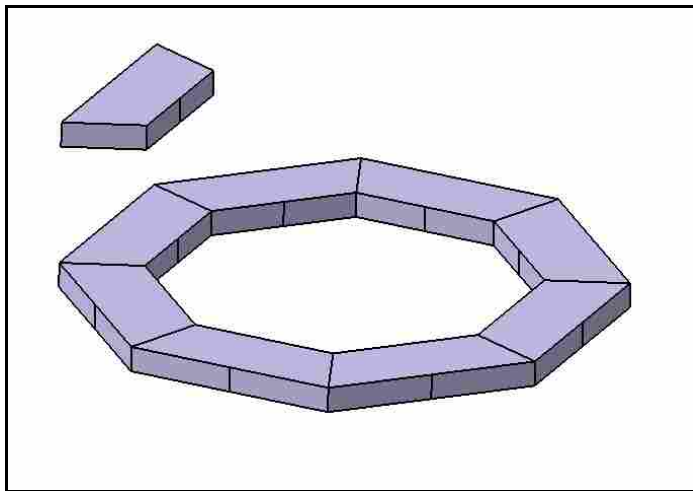
Figure A-4 Single insulation block and assembly of blocks upon which the support plates rest.

86
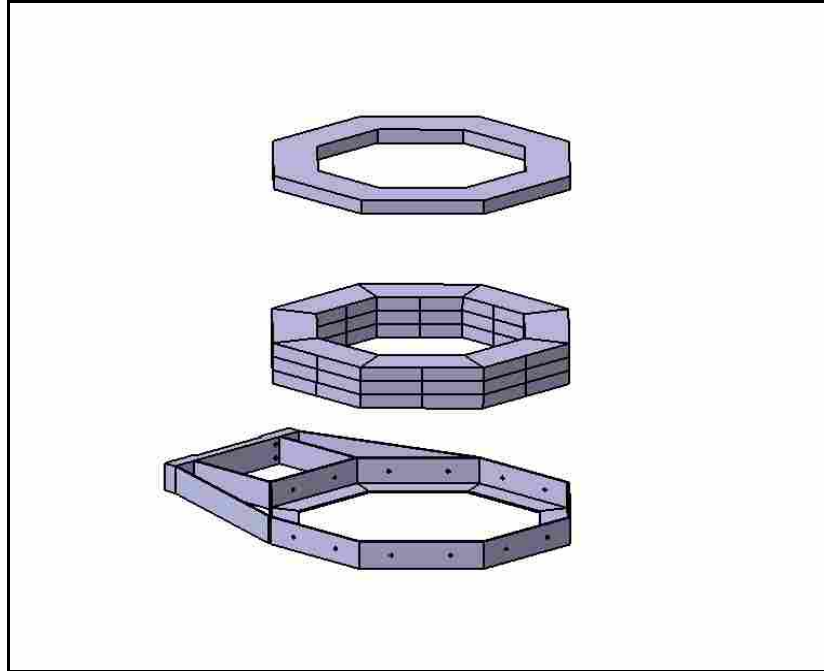
Figure A-5 Exploded view of the octagonal steel support frame and three layers of assembled insulation blocks, and a layer of insulation blanket cut to the same shape as the assembled blocks.
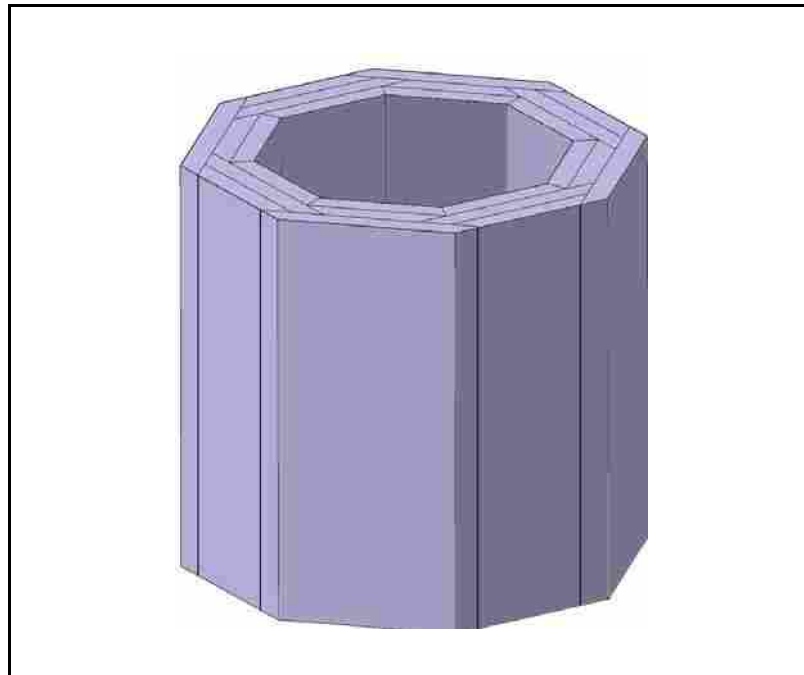
Figure A-6 Assembled insulation panels that surround the main reactor tube and the hot sections of the electrical heating elements.

A.4 Heaters and Electrical System

The reactor's heating elements are made of molybdenum DiSilicide and are capable of reaching temperatures of around 1775 °C. The heating elements together with the wire straps that connect the heating elements to the power cables are sourced through Micropyretics Heaters International (MHI). The heating elements are held in place by mullite tubes that fit into holes drilled in the insulation panels. The wire straps are connected to the power cables mounting lugs by fastening both to grade G-11 Garolite insulating panels, this material can be purchased from McMaster, the mounting lugs can be purchased from MSC for cable size 2/0.
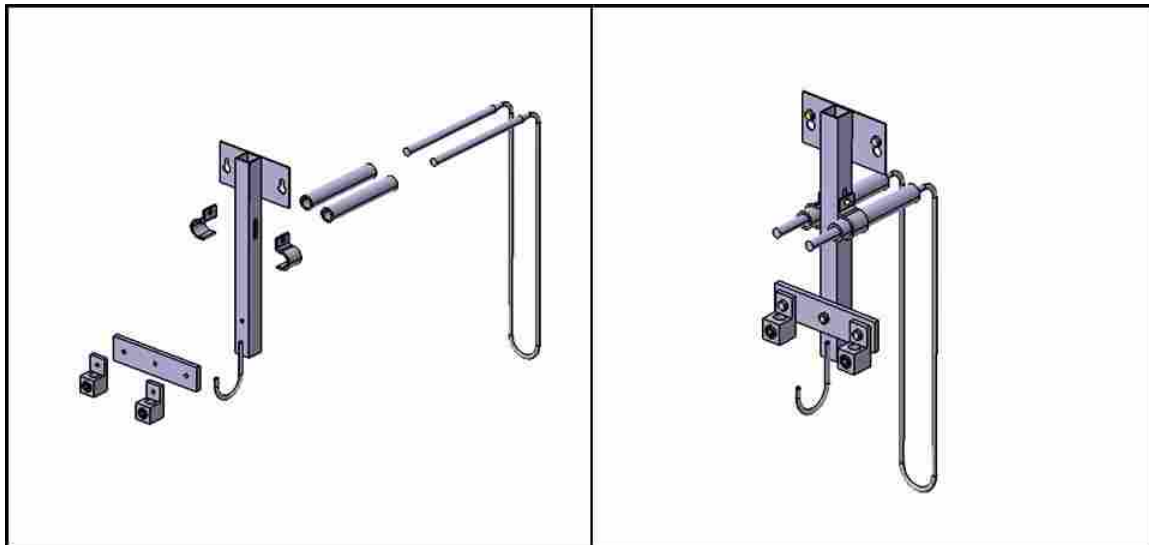
Figure A-7 Exploded and assembled views of the heating element installation. Shown are the steel support bracket, the Molydenum DiSilicide heating element, the mullite tube that support the cold section of the heating element, and the Garolite panel to which the mounting lugs are connected. Not shown are the wire straps that connect the mounting lugs to the ends of the heating element.

A.4.1 Control Panel and SCR/Relay Panel

The control panel and SCR/Relay panel were designed and custom built for the NMFR by Chromalox according to BYU's specifications. The control panel features 8 heater control circuits each composed of closed-loop temperature controllers as well as overtemperature sensors for monitoring the temperature of each heating element. The control panel is also fitted with other control units which are currently unused but which may be used in the future for additional reactor systems such as liquid fuel feed systems, natural gas burner ignition, electrical air preheater control, and so on.
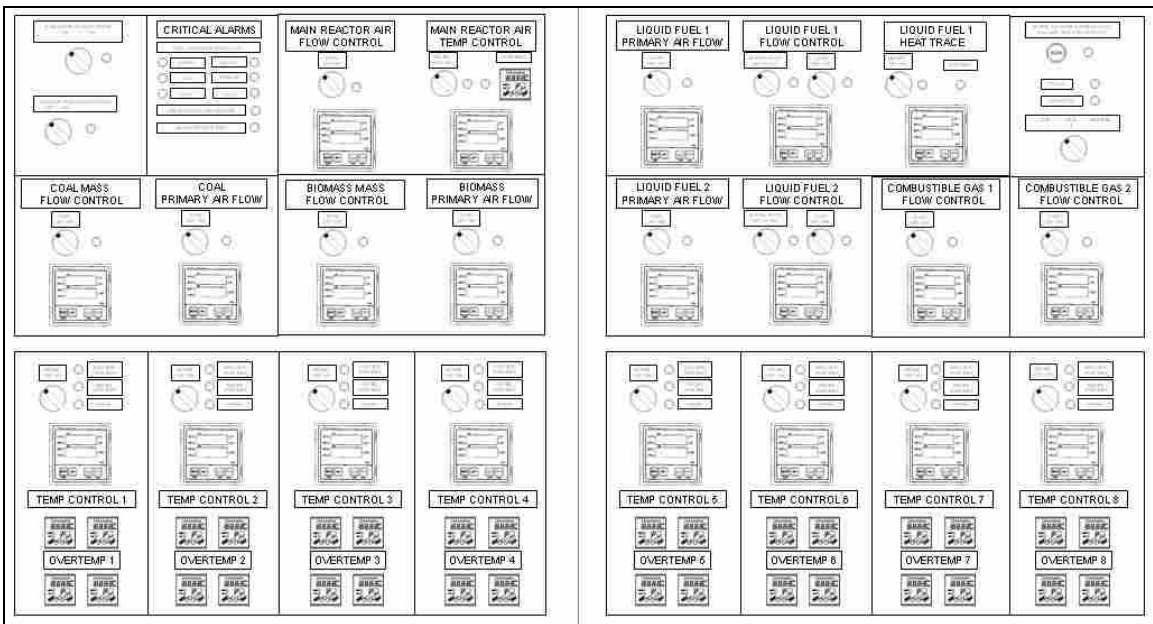
Figure A-8 Layout of the control panel. The bottom section features the temperature controllers for each reactor section's heating elements. The top half features unused controllers reserved for future uses like electrical air preheaters, liquid fuel feeders, etc.

89

A.4.2 Thermocouples

The air gap located between the main silicon carbide reactor tube and the surrounding insulation panels is fitted with a single, K-type thermocouple that is connected to the temperature control panel for use in feedback control. The reactor design originally called for four additional thermocouples in each reactor section to monitor the temperature of each heating element to prevent any single element from overheating. Later it was determined that the resistivity of the molybdenum disilicide element material increased so much with temperature that overheating the elements would be essentially impossible without changing power supplies. As it is currently setup, the overtemperature thermocouple sensors that would monitor the heating elements have been jumpered to indicate room temperature and thus never cut power to the heating elements.

A.4.3 Transformers

Each reactor section supplies power to each of its four heater elements from a single transformer. These transformers were sourced from the Johnson Electric Coil Company of Antigo, WI. The transformers' features a single primary winding design for single-phase 480 volt input power coming from the SCRs. The secondary side of each transformer features four windings, one for each heater, that is designed to supply up to 200 A at 17.5 volts to its heater.

A.5 Burner Assembly

The burner assembly is essentially a refractory-lined steel cylinder which sits atop the reactor and is designed to burn natural gas with air in an overall lean mixture before being fed into the reactor itself through a ceramic monolith flow straightener.

A.6   Air, Natural Gas, and Coal Feed Systems

The reactor is fitted with a plumbing system that is capable of delivering air, natural gas, and coal to the reactor. The systems can be staged in a wide range of configurations to provide flexibility in controlling the temperature, velocity, and stoichiometry inside the reactor.

A.6.1   Natural Gas Burner

The natural gas burner used to preheat the primary air stream before it enters the reactor consists of a custom built, stainless steel air distribution plenum that holds a modified Ventite Inpirator natural gas burner manufactured by Maxon. The burner was modified so that the air as well as the natural gas flowing through the burner could be metered (the original designed only allowed for natural gas metering). The burner is fitted with a replaceable, cast-iron burner nozzle that can be easily replaced when it wears out.

A.6.2   Air Distribution Plenum

Air is fed into the burner assembly through a stainless steel distribution plenum which feeds a single stream of air into the burner assembly via four inlet ports which are located circumferentially around a centrally located partially premixed natural gas feed as shown in Figure A-9. Several potential plenum designs were built using PVC tubing and fittings. To determine which design would most-evenly distribute the incoming air between the four port the designs were then connected to an air-supply and the flow velocity at each of the four ports were measured. The design with the smallest variation in exit velocities was chosen for the final design.
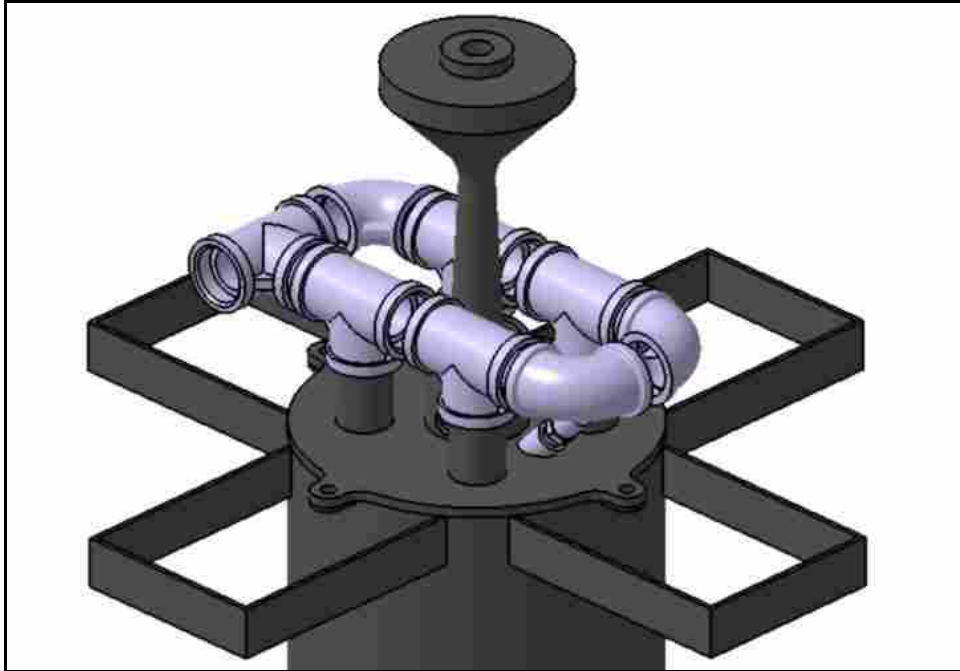
Figure A-9 - Air distribution plenum that divide a single air stream betwen four ports that feed the primary air into the natural gas burner/preheater before flowing into the reactor itself.

A.6.3   Refractory and Insulation

The cylindrical shell of the burner assembly is made of a section of thin-walled steel pipe. The steel pipe is protected from the natural gas flame by a layer of insulating fibers which are in turn covered by a cast layer of refractory that forms the inner surface of the burner assembly. The refractory used is Kast-o-Lite brand manufactured by RHI Refractories, a company which was recently purchased by ANH refractories which discontinued the Kast-o-Lite brand. For future reference the Kast-o-Lite material should be interchangeable with any castable refractory with a thermal conductivity of less than 0.5 W/m-K and a maximum service temperature of 1650 °C.

A.6.4 Flow Straightener

A ceramic substrate normally used for pollution control in diesel engine systems was installed at the bottom of the burner and rests inside the mounting lip of the top reactor tube. The substrate is a 15.2 cm (6 inch) diameter cylinder that is 5.1 cm (2 inch) tall with small, narrow parallel passages allowing flow to pass through the cylinder from top to bottom as can be seen in Figure A-10. The passages are narrow enough relative to their length that they remove essentially all swirl and large eddies from the flow before it enters the reactor.
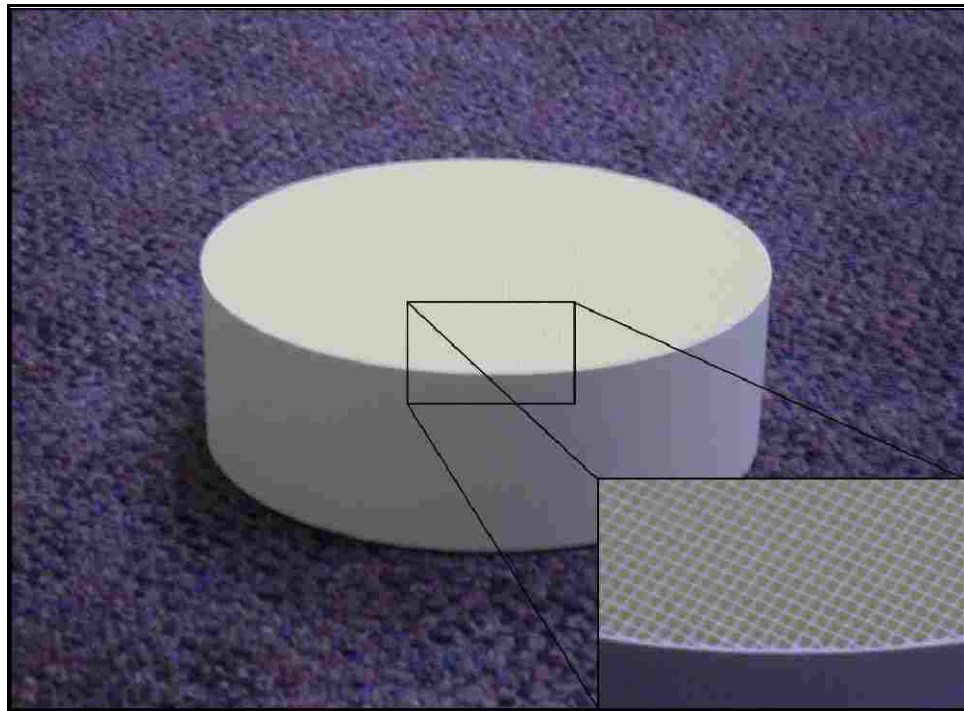
Figure A-10 Ceramic substrate used as a flow straightener below preheater.

A.6.5 Flame Detector

An electronic flame detector circuit was built in order to help ensure that natural gas from the burner does not enter the reactor unburned. The circuit works by conducting a very small current through the metal burner housing, the flame itself, the flame detector, and large resistor (approximately 20 MΩ). The circuit measures the voltage difference across the flame and passes this voltage through a simple voltage follower op-amp circuit which can then be used to activate a warning light to indicate when the flame has been extinguished (when the flames resistance has become much larger than 20 MΩ).

A.7 Plumbing

After construction was completed of the structural and electrical components of the reactor in the fourth quarter of last year, work began on completing the plumbing systems which are capable of supplying and measuring various fuels and gases.

A.7.1 Coal Feed

The new reactor shares an auger-driven coal feeder with the pre-existing reactor. The auger drives the pulverized coal out of a hopper and into a funnel which channels the coal through a funnel and into the throat of an eductor that entrains the coal in one of the air-supply lines leading into the reactor. The coal and air mixture is then fed through a stainless steel lance that fits through any of the access ports along the length of the reactor. The lance features an elbow which sprays the flow out of the lance downwards along the centerline of the reactor. The lance itself is cooled by the flow it carries and does not use any external cooling to prevent overheating.

A.7.2 Gas Feeds

In addition to the air feed in which the pulverized coal is entrained, the reactor has also been fitted with three additional air feeds. Two of these feeds lead to the burner assembly; one for the premixing with natural gas to prevent sooting, and the other is fed through the air distribution plenum and into the burner around the circumference of the burner to be heated by the natural gas flame. The final air feed is used for staging at some location in the reactor below the coal feed and can be combined with a natural gas feed.

The reactor as also been fitted with two natural gas feeds. As already mentioned, one natural gas feed leads to the burner assembly where it is premixed with air and burned to heat the excess air. The second natural gas feed leads to a stainless steel lance which can be inserted through any of the reactor's access ports.

A.8 New Reactor Brought Online

Once plumbed, the reactor was ready to be brought online and shaken down. The process involved developing procedures for running the reactor including start-up and shutdown procedures to prevent problems from arising including excessive thermal stresses.

A.8.1 Operational Procedures

To prevent damage to the reactor and to provide guidelines for the reactor's future use a document has been developed which lays out standard procedures for performing start-up and shutdown. The start-up procedure details the prescribed power settings, soak times, and set-point temperatures to heat up the reactor as quickly as possible while simultaneously avoiding thermal shocks to the reactor's more susceptible components

(heaters, ceramic plates, etc.). The start-up procedure also gives the proper sequence for starting the various auxiliary components of the reactor (air compressor, exhaust fan, natural gas flame ignition, gas analyzer, and coal feeder). Likewise, the shutdown procedure also lists the proper sequence for deactivating various reactor subsystems and also details proper soak times and power levels for allowing the reactor to cool down at the proper rate.

A.8.2   Thermal Stress Monitoring

In initial testing of a single section of the reactor, one of the silicon carbide plates that helps support the reactor tube was found to have cracked after its inner and outer edges experienced a large temperature difference. It should also be noted here that excessive thermal stresses may also arise due to the failure of one or more heating elements in a reactor section. A broken heating element may lead to locally cooler support plate temperatures and thus thermal stress. After analyzing the test data it was judged that 250 °C should be the maximum allowable temperature difference during normal operation (defined as the difference in temperature between the set-point thermocouple and a thermocouple mounted on the outer edge of upper support plate). While the standardization of the start-up and shutdown procedures have been designed to prevent the thermal stresses from being a problem again, each reactor section's temperature difference is constantly monitored as a further safeguard.
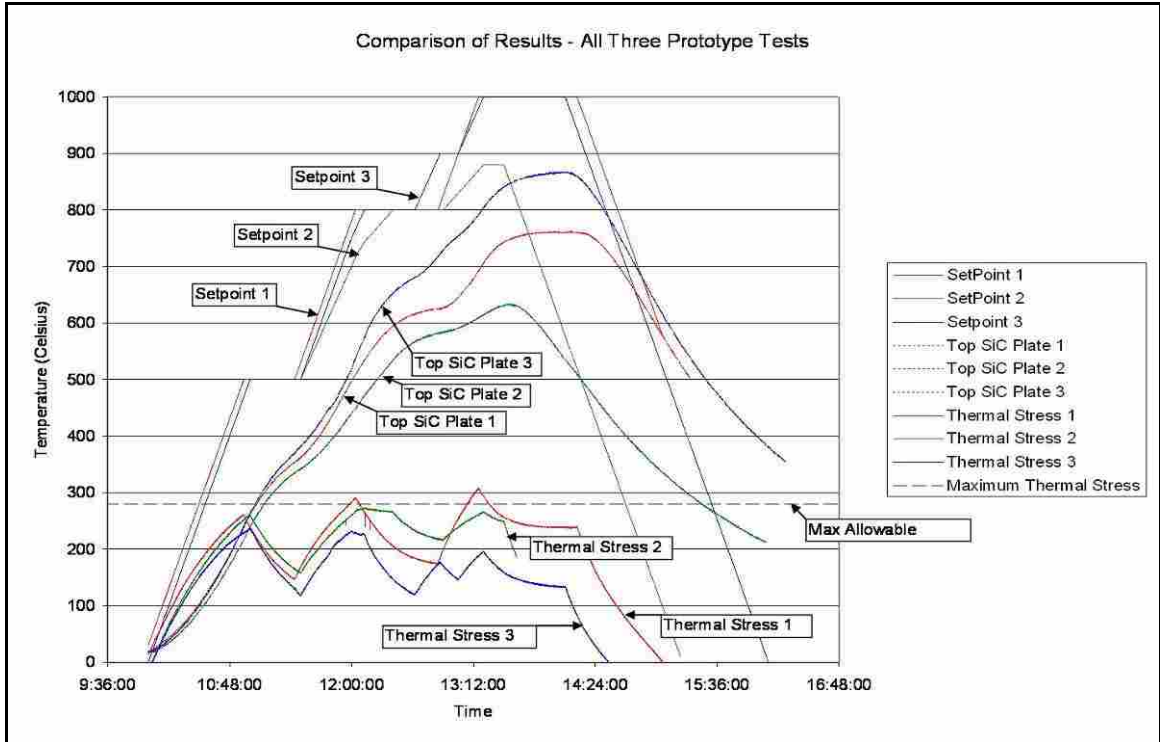
Figure A-11 Plot of temperatures during a test in which a support plate cracked apparently due to thermal stresses. The thermal stresses are represented as temperature differences between the setpoint (inner) temperature and the top SiC (outer) temperature.

A.8.3   Start-up and Cool-down Procedures

The operational procedures for the various reactor functions are given here:

- Electrical Heater Startup (Set-Point Mode)

  o Turn the Main Switch on the Power Supply Box to "On"

  o Turn the Control Panel Main Power Switch (Top Left) to "On"

  o Verify that all controller set-points are at 150 C

  o Change all controllers to "Auxiliary" control and set to 0% power output

  o Turn the power switches for each reactor section to "On"

97

- Each reactor section has a power-box switch and a control-panel switch, both of these switches must be turned to "On" before current will flow to the heaters

- Gradually Increase each controller's power output setting to 3%

- Gradually Increase each controller's power output setting to 6%

- Gradually Increase each controller's power output setting to 10%

- Allow Reactor Sections to Heat up to Just Above 150 C (155 C is about right)

- Decrease each controller's power output setting to 0% and Turn the power switch for each reactor section (use the control-panel switches instead of the power-box switches)

- Push the "Aux" button to switch to Set-point control

- Verify that the set point has increased to 150 C

- Push the "Aux" button again to verify that the set-point-control power output setting is less than 1%

- Turn the power switch for the reactor section back to "On"

- Push the "Aux" button to switch back to set-point control

- Enter New Set Point

- Labview Startup

  - Turn on the Ground Floor Computer, all power supplies, and the DAQ box hanging from the ceiling

  - Open the"Blanchard_Use_This_One" desktop shortcut to the labview DAQ program

- o Click cancel if an error message pops up

- o Start the VI and start recording data by pushing the record button so that it turns bright green and shows "on"

- o An excel spreadsheet called "project" will open when the VI is started but no data will be written to it until the record button is pushed.

- Air Flow Startup

  - o Start Air Compressor in B-38 per instructions in the Compressor Log Book

  - o Purge Moisture From Compressed Air Line in Basement

  - o Open the Basement Rotameter's Air Valve until approx. 5 SCFM are flowing through the Rotameter

  - o Open the Ground Floor Air Valve (the one that supplies the coal feed stream and the natural gas premixer stream) until Labview shows approx 9 kg/hr of air is flowing.

- Exhaust Fan Startup

  - o Change the Exhaust Fan Filter

  - o Turn on the Exhaust Fan Breaker Switch at the Breaker Box on the ground floor in the south-west corner of the building

  - o Set the Exhaust fan speed value to about 45 Hz

  - o adjust this speed while the reactor is running to ensure adequate dilution of the exhaust stream

- Natural Gas Burner Startup

- o Open the ground floor natural gas ball-valve upstream of the 2 natural gas lines.

- o Light the 'flamethrower' with a match

- o Lift the stainless steel burner manifold assembly off of the top of the burner housing.

- o The assembly can best be lifted by holding the assembly at the venturi throat

- o Hold the flame of the flamethrower near the exit of the venturi

- o Have an assistant turn the black plastic natural gas valve until the valve is about open by about 1/16 of a turn.

- o Have the assistant adjust the natural gas flow rate until it is 'just right.'

- Gas Analyzer Startup

  - o Turn the power switch on the back of the analyzer to "On"

  - o Wait Approximately 1 hr for the analyzer's start-up sequence to finish

  - o Calibrate as necessary (Instructions for calibration are not given here)

- Coal Feeder Startup

  - o Turn the Power Knob to "On"

  - o Push the Feed Rate Set Point Button and Enter Desired Coal Flow Rate

  - o The Coal Feeder Operates in Units of Lbs/hr

  - o Push the Power Knob to Start/Stop Coal Feed

- Shutdown Sequence (Set-Point Mode)

  - o Turn the set-points of the heater element controllers back to 150 C

  - o Turn coal feeder off

- Close Labview and save the spreadsheet data if desired

- Allow the section to cool down to about 800 C

- Turn off the natural gas burner

- Check the power output of each reactor section periodically (by pushing the "Aux" button twice) to monitor the power output of each section

- Once the power output for a section has gone to zero, turn the power switches for that section to "off"

- Turn off the Air Compressor in B-38

- Follow the shutdown instructions in compressor's operation manual

- Once the reactor has cooled to about 300C turn off the control panel, the main power supply box, and the exhaust fan (at the breaker, not with the controller)

- Gas Analyzer Shutdown

  - Push the "Purge" Button

  - Wait until the purge is completed

  - Turn the power switch on the back of the analyzer to "off"

A.9 Electrical System Repairs

Since being brought online the reactor's electrical system has suffered a number of reliability issues. Drawings and schematics for the electrical system including the control panels can be found inside the door of the large power control panel. The system involves high voltages, high currents, and high temperatures and repair work should only be undertaken with proper regard for safety.

A.9.1 SCR's

The current flowing to each reactor section's transformer is controlled by a single silicon-controlled rectifier (SCR). After tens of hours of normal operation one of the SCR's failed which turned the SCR into a short circuit and caused the circuit's very-fast-acting fuse to blow. Replacing the SCR solved the problem which has not occurred since. Replacement SCRs can be purchased from Allied Electronics at alliedelec.com under the stock number 550-0706.

A.9.2 SCR Control Circuit

At least one of the SCR controllers has experienced the problem of a "drifting zero," that is a "zero signal" (4 mA) coming from the temperature controller is interpreted by the SCR controller as non-zero, this can lead to either current being sent to the heaters when none is desired or vice-versa. This problem can be temporarily remedied by adjusting the SCR controller's "zero" trim potentiometer until its "demand" light just turns off, however this will only solve the problem until the next time the circuit is powered up, if that long.

A.9.3 Overheating Wires

When the electrical system was first designed, larger gage power cables were specified than were actually installed by the BYU electrical shop. These cables connect the transformers to the wire straps that lead to the heating elements. As a result these cables are located close to the reactor and tend to get very warm (temperatures around 70 – 80 °C have been measured). It is believed that the combination of the high temperatures and undersized cables have been the cause for a number of these cables overheating and,

together with the mounting lugs that connect the cables with the wire straps, partially melting. Electrically conductive grease has helped to this problem somewhat but the problems persists.

A.9.4   Heating Elements

The electrical heating elements located in the air-gap between the reactor tube and insulation panels reach extremely high temperature as they heat the reactor to higher than 1200 °C. Operating in this extreme environment the heating elements are liable to crack and break. It was thought that these problems could be related to electrical contact resistance at the elements' connections so each connection has been covered with conductive grease as was mentioned previously. So far each of the four elements that have failed, have broken at one of the elbows as can be seen in Figure A-12. The possibility of purchasing elements with thicker elbows is under consideration.

Figure A-12 - Broken heater element.

A.10 Reactor Part Drawings

THIN LAYER OF BLANKET INSULATION
BETWEEN PIPE AND REFRACTORY

PIPE

CAST REFRACTORY

SMALL TABS TO
RETAIN REFRACTORY

1.25
.13
1.25

Ø8.00 Ø7.50 Ø6.25

16.00

A-A

R .41 4 PLACES

Ø.39 4 PLACES

4.82 4 PLACES

Ø8.25

Ø8.63

20.00 5.00

BURNER CAN ASSEMBLY

106

Ø1.32
Ø1.05

2.25

PLENUM RUNNER - 4 PIECES

DRILL AND TAP FOR
1/4-28 SET SCREW

1.00
.65

B-B

A

B   B

A

.25

2.41
1.50

DRILL AND TAP FOR
1/4-28 SET SCREW

A-A

BURNER HOLDER

R.44   Ø.38
Ø8.63
Ø1.32
3.63
R.50 TYP
.35
.25   Ø2.38
3.63
FULL R

BURNER CAP PLATE

BURNER CAP ASSEMBLY

90-DEGREE TEE
1-INCH PIPE
6 PIECES

90 DEGREE ELBOW
1-INCH PIPE
3 PIECES

CONNECTOR PIPE
9 PIECES

3.50   3.63   3.50

3.63

⌀1.32
⌀1.10

1.55

CONNECTOR PIPE

PLENUM ASSEMBLY

1 END PRECISION GROUND

⌀1.61
⌀1.26

12.01

ACCESS TUBE

19.29

9.65

R3.25

135° TYP

4.00

.28
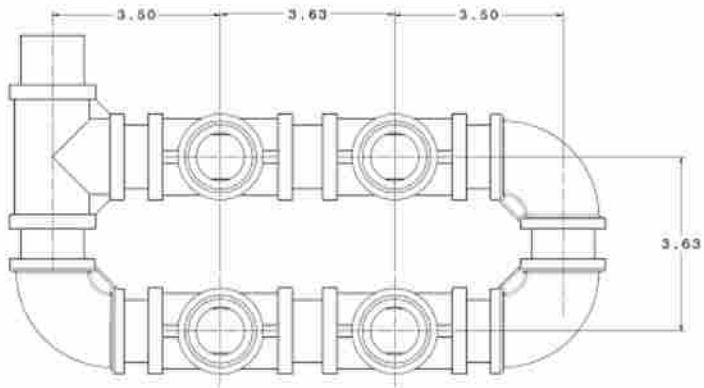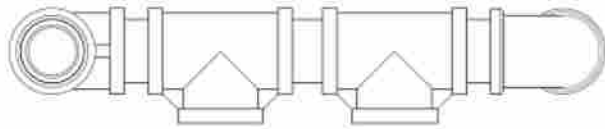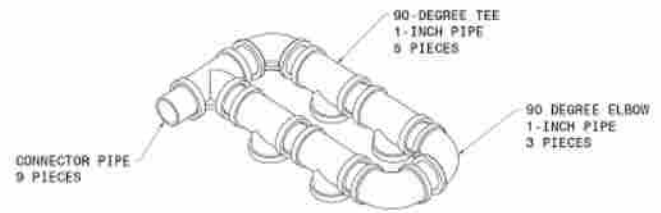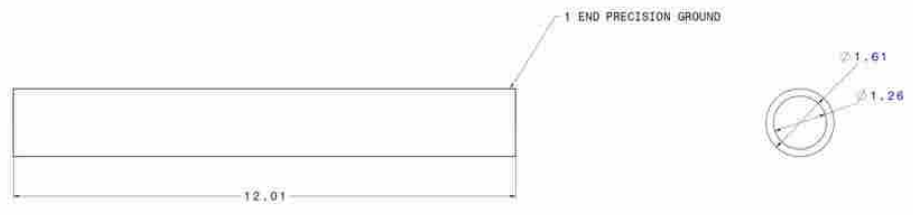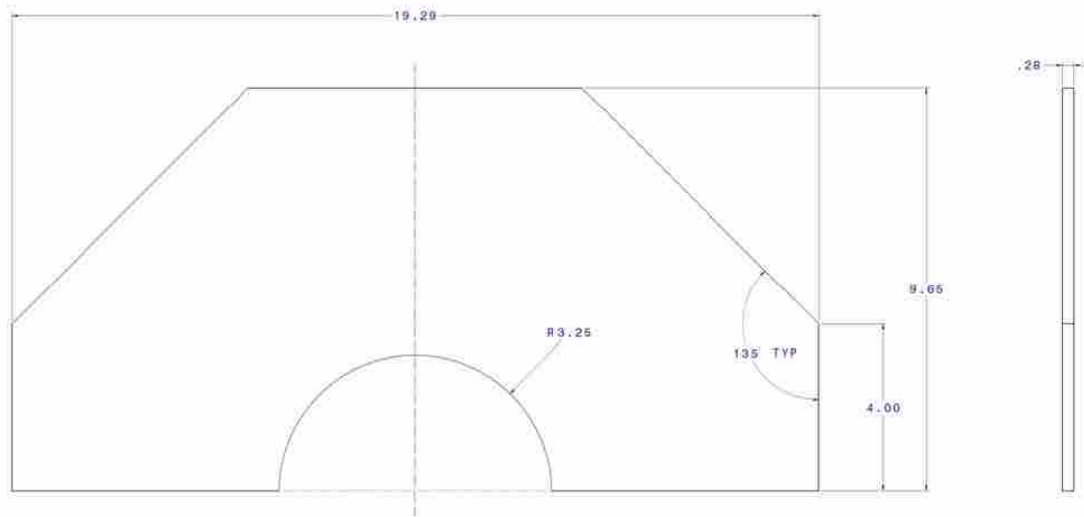
SUPPORT PLATE

Main Reactor Tube

110

8.62

.75

7.12

⌀.47

1.97

14.45

⌀.24

111

HEATER ELEMENT

112

Ø.25 2 PLACES
Ø.50 2 PLACES

5.00

4.00

2.50

.50 2 PLACES

1/16 SHEET

1x1 BAR
1/16 WALL

8.38

6.00

.25 DRILL THRU
3 PLACES

FIBERGLASS INSULATOR

1.50

3.75

.50

1.00

13.13

.29

2.00

.50

2.25

FULL R

.25

12.00

.25 DIA ROD
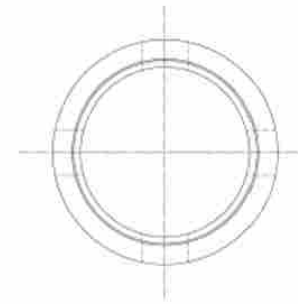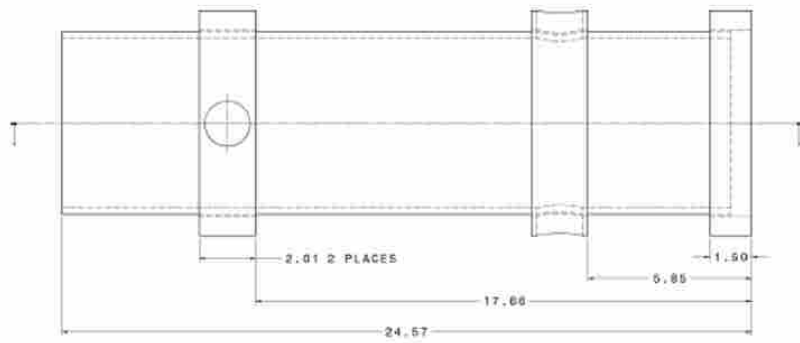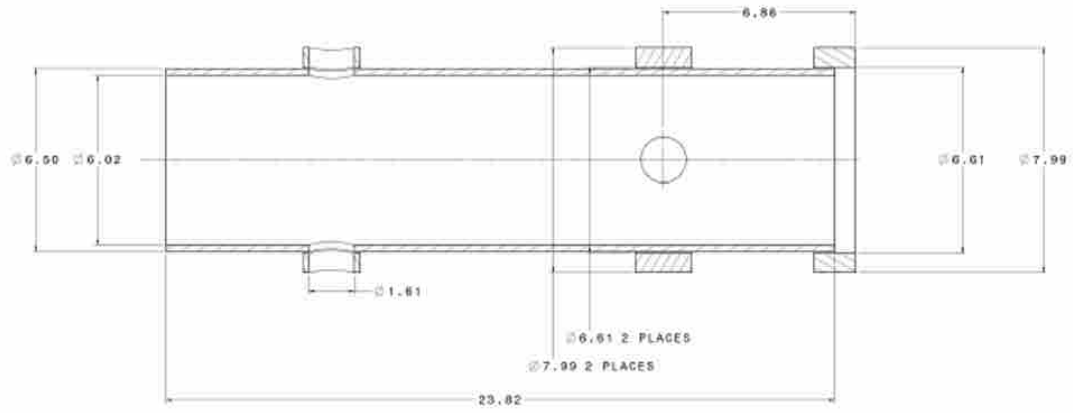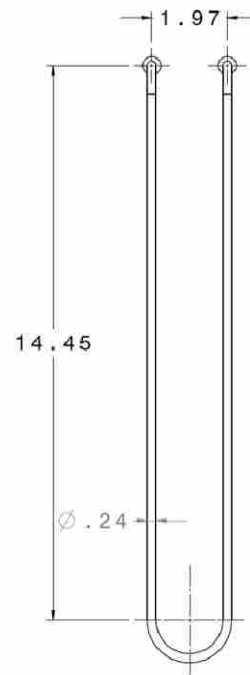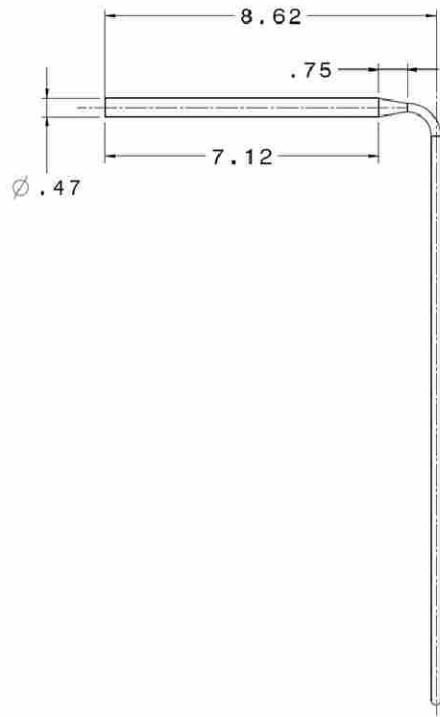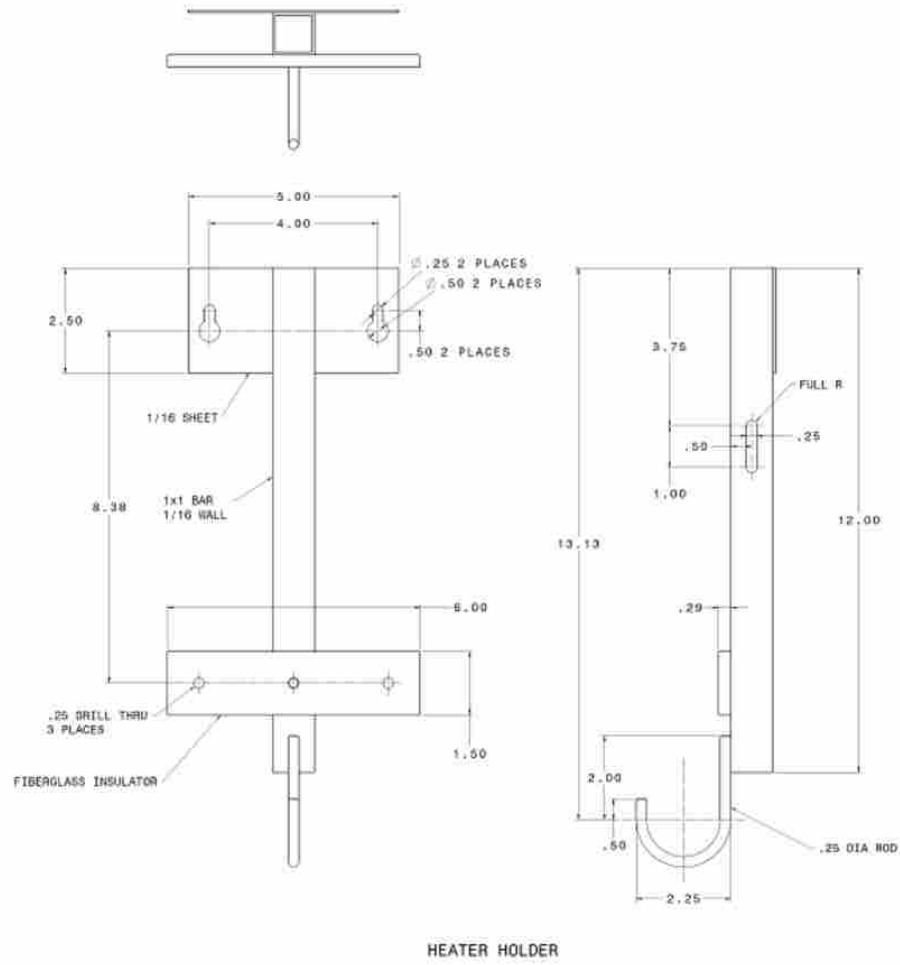
HEATER HOLDER

INSULATION RETAINER
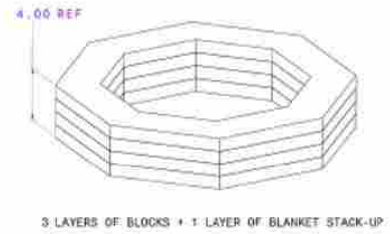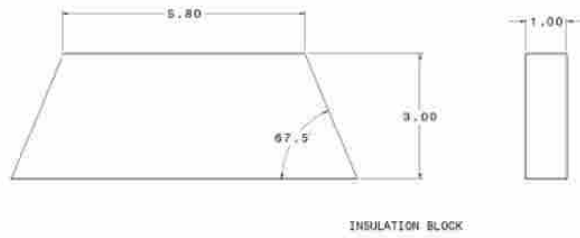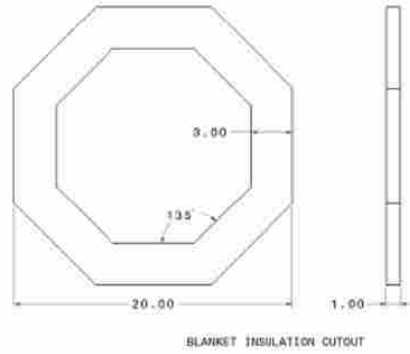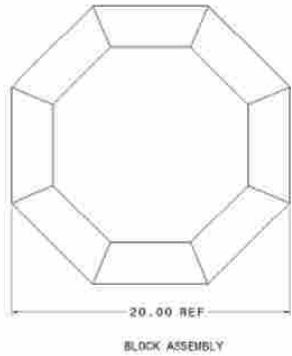
1.00

Ø.25

.50

Ø.50

2.50

1.00

4.00

6.00

.81

1/16 SHEET

20.00 REF

BLOCK ASSEMBLY

3.00

135°

20.00

1.00

BLANKET INSULATION CUTOUT

5.80

1.00

3.00

67.5°

INSULATION BLOCK

4.00 REF

3 LAYERS OF BLOCKS + 1 LAYER OF BLANKET STACK-UP

5.38   1.00

67.5

INNER LAYER : 8 PIECES

7.04   1.00

45

MIDDLE LAYER : 4 PIECES

4.21   1.00

45

MIDDLE LAYER : 4 PIECES

7.87   1.00

45   45

OUTER LAYER : 4 PIECES

5.04   1.00

45   45

OUTER LAYER : 4 PIECES

ASSEMBLY DIAGRAM

19.60

ASSEMBLED INSULATION PANELS

FRONT TAB

BACK TAB

BOTTOM TAB

4.59

3.37

1.17

1.42 1.25

.63

.80

4.22

.13

FRONT TAB

1.00

1.00

.13

A-A

1.50

.75

.55

1.06

.25

BACK TAB

9.76

11.43

135° TYP

13.84

5.71

22.60

REACTOR COVER - FRAME

5.22

1.59

1.90

3.63

.50

.88

.50

1.72

BOTTOM TAB

117

130°

135° 135°

40.74

35.02

29.20

21.18

9.76

2.82

⌀3.50

6.91

⌀3.50

18.12

22.00
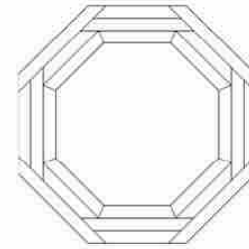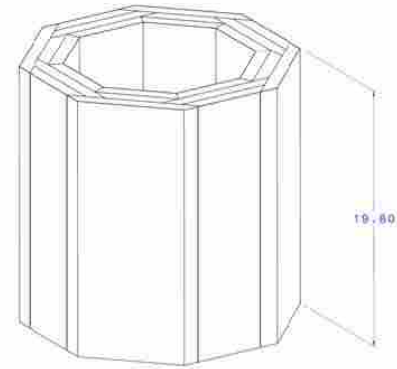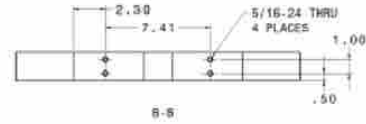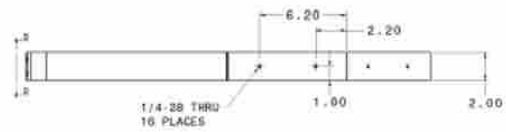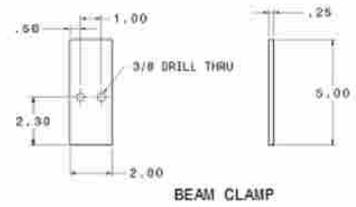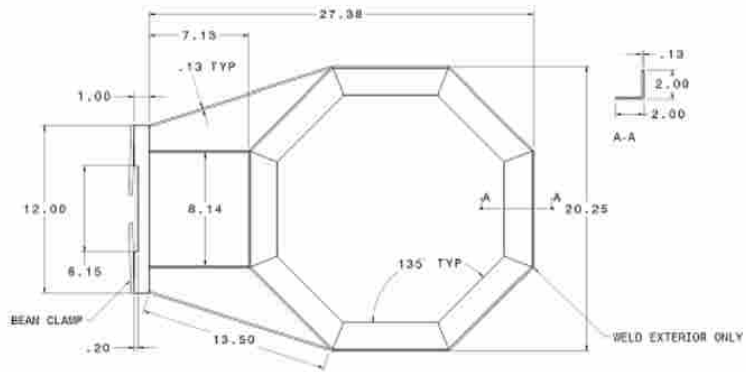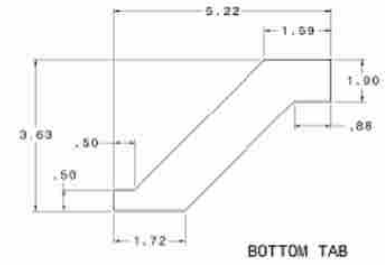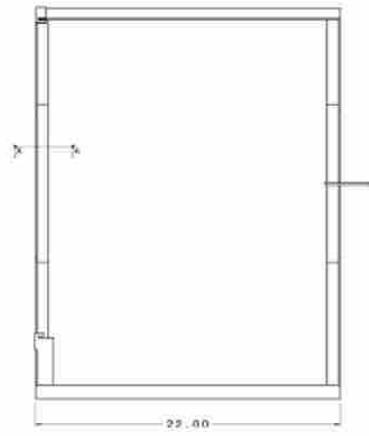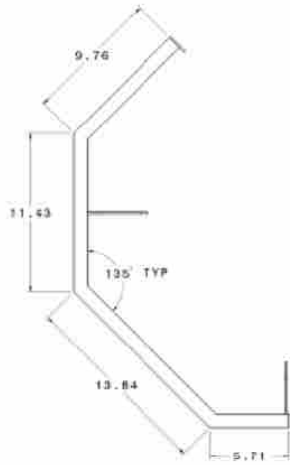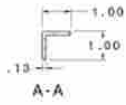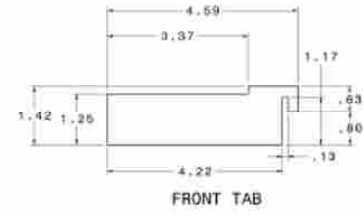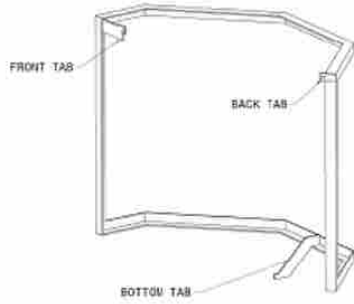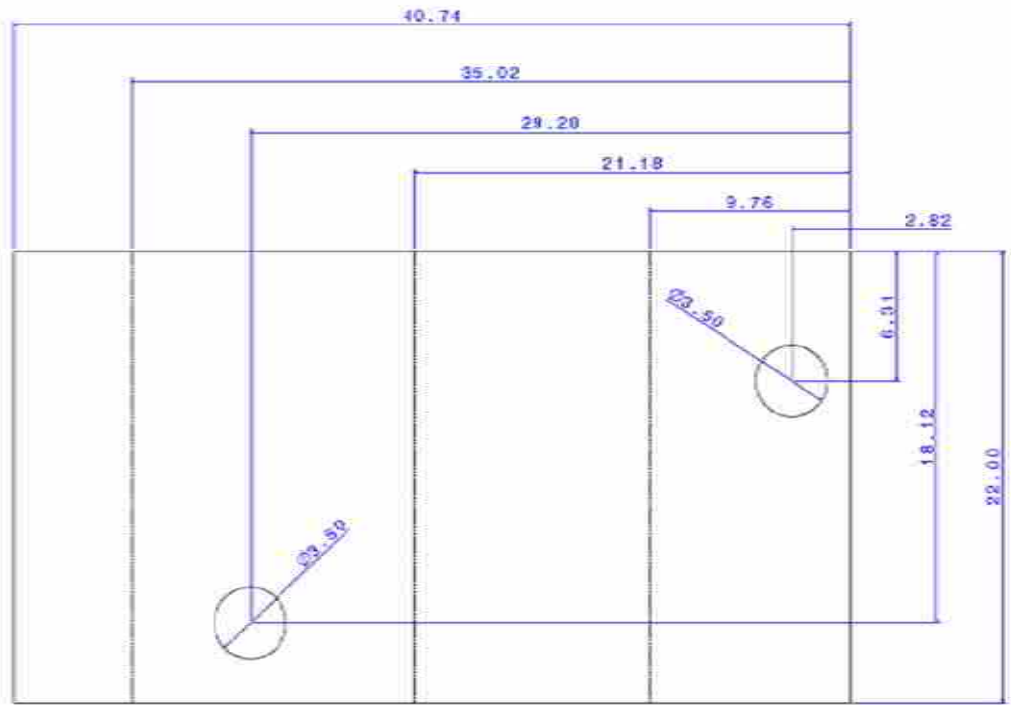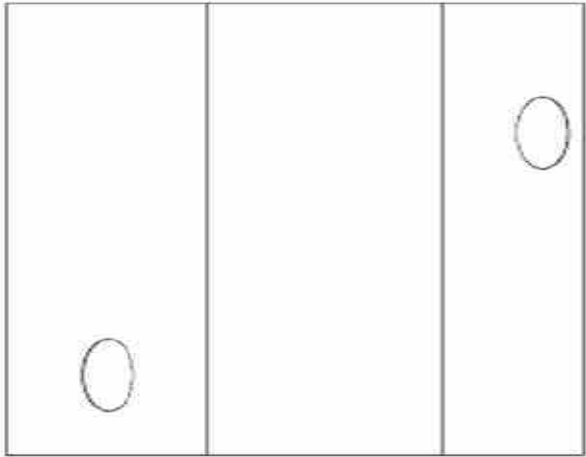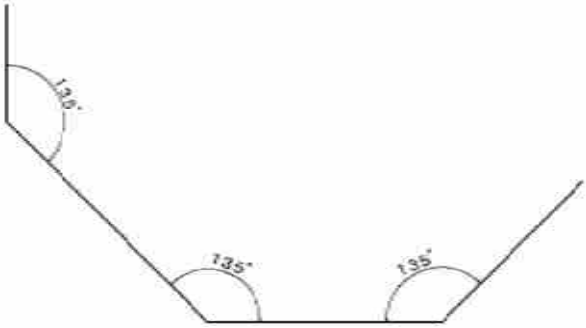
REACTOR COVER - SHEET METAL

118

.25 OD X .039 WALL
STAINLEES STEEL TUBE

17.25

R .62

R .62

1.00

4.13

NATURAL GAS FEED LANCE

1/4 SWAGE-LOK FITTING

18.13

.375 OD X .039 WALL
STAINLESS STEEL TUBE

R .94

.89

R 1.44

5.69

SOLID FUEL FEED LANCE

3/8 SWAGE-LOK FITTING
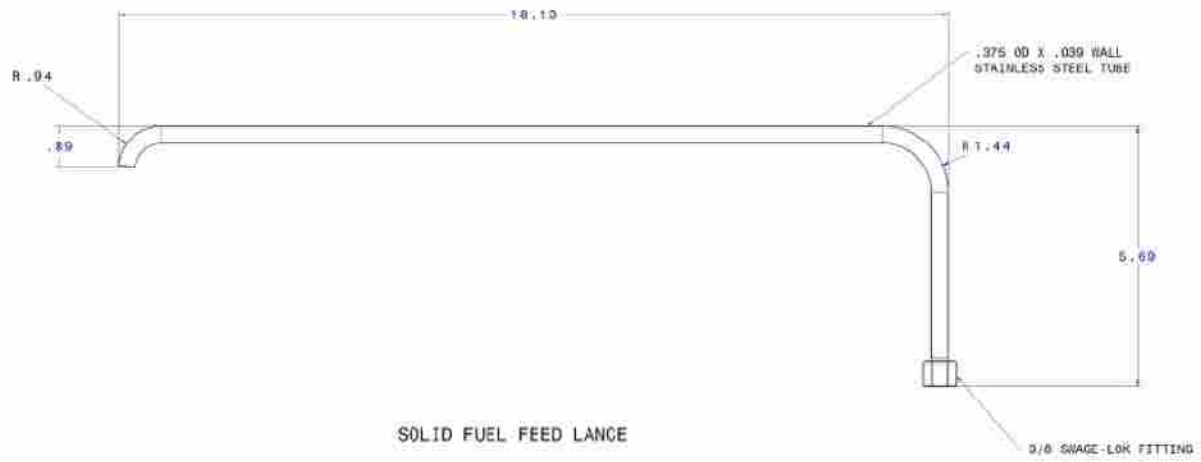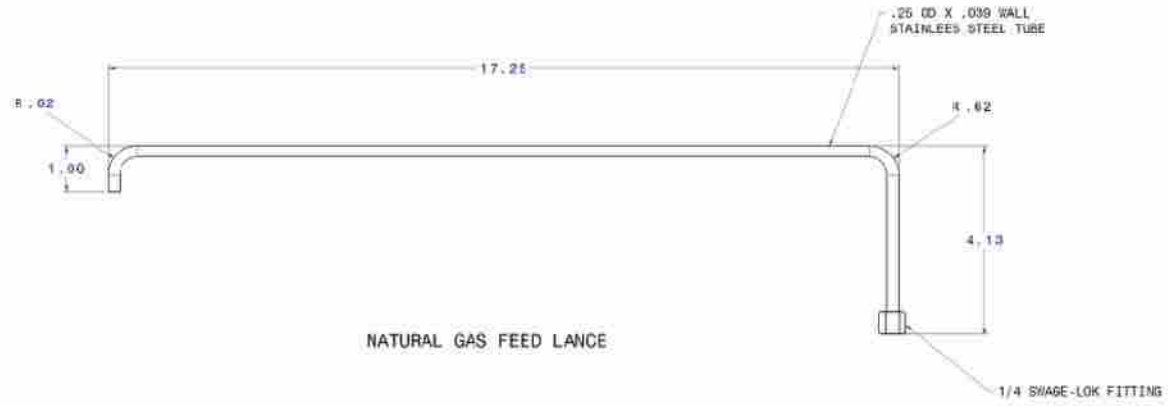
Appendix B.   UDF Source Code

/*

UDFs for describing transient ash deposition behavior

Ryan Blanchard

rpblanchard@gmail.com

*/

//Global Variables Defined

```c
#include "udf.h"
#include "models.h"
#include "dpm.h"
#define T_Cool      300              // Cooling Temperature Beneath Ash and
Base Layers (K)
#define T_Slag      1600             // Temperature at which slagging occurs (K)
#define T_Sinter 1300          // Temperature at which sintering occurs (K)
#define T_Shift -50           // Temperature Shift parameter for Browning
Viscosity Model (K)
#define K_Slag 5              // Thermal Conductivity of Slag Layer (W/m-K)
```

```
#define K_Sinter 1                    // Thermal Conductivity of Sintered Layer (W/m-K)

#define K_Particulate .4              // Thermal Conductivity of Particulated Layer
(W/m-K)

#define RHO_Sinter 1200                  // Density of Sintered Layer (kg/m^3)

#define RHO_Slag 2000                    // Density of Slag Layer (kg/m^3)

#define RHO_Particulate 800          // Density of Density of Particulate Lcccayer
(kg/m^3)

#define TIMESTEP_SIZE 600            // Timestep Length (s)

#define R_BASE 0.095                    // Thermal Resistance of Base Layer (m^2-
K/W)

#define RR_DBAR 10.6e-6                 // Rosin-Rammler parameter for avg.
particle size (m)

#define RR_SF 1.243                 // Rosin-Rammler parameter for shape factor

#define RR_NUM_PARTICLES  1000            // Total Number of particle streams
from injectors

#define RR_MASS_FLOW   8.8e-6        // Total ash mass flow from injectors (kg/s)

#define RR_DIAM_MAX    50e-6            // Rosin-Rammler maximum particle size
(m)

#define RR_DIAM_MIN    4e-7            // Rosin-Rammler minimum particle size
(m)

#define EXP   2.718282            // e

#define PI     3.141593          // pi

#define critical_viscosity 10000     // Critical viscosity for particle sticking (kg/m-s)
```

```
/*

UDM Locations

0 - Total Deposit Mass

1 - l/k Effective Thermal Resistance of Combined Ash Layers

2 - Particulate thickness

3 - Sintered thickness

4 - Slag thickness

5 - Current Simulation Time

*/



//Particle impaction Boundary Condition UDF that is called when particle 'p' impacts face
'f'

DEFINE_DPM_BC(capture_bounce_bc, p, thread, f, f_normal, dim)

{


real p_loc[ND_ND],p_temperature, p_diameter;

real plocy,pvel;

real A[ND_ND],area,flow,flux;

real viscosity, visc_exponent;

real p_rep_mass, deposit_mass;


//Calculate the mass represented by the impacting particle
```

p_diameter=P_DIAM(p); //Get Particle Diameter from Fluent

p_rep_mass=RR_MASS_FLOW*TIMESTEP_SIZE*(RR_DIAM_MAX-

RR_DIAM_MIN)*(RR_SF/p_diameter)*pow((p_diameter/RR_DBAR),RR_SF)*pow(E

XP,-1*(pow((p_diameter/RR_DBAR),RR_SF)))/RR_NUM_PARTICLES;

printf("%1.9lf\t%1.9lf\n",p_diameter,p_rep_mass);

//This is the function that is supposed to calculate the mass represented by the particle,

FLUENTreturns an error when I have used it

//p_rep_mass = P_FLOW_RATE(p)*TIMESTEP_SIZE;

//Determine viscosity of ash particle

p_temperature=P_T(p);   //Get particle

temperature from Fluent

visc_exponent=14788/(p_temperature-T_Shift)-10.931;   //Calculate Ash

Viscosity

viscosity=(p_temperature-T_Shift)*pow(10,visc_exponent);   // Finish Viscosity

Calculation

//Assume deposited mass is inversely proportional to viscosity when particle viscosity is

less than critical

deposit_mass = p_rep_mass;

```c
if(viscosity>critical_viscosity)

        {

        deposit_mass = p_rep_mass*critical_viscosity/viscosity;

        }




//Calculate mass deposited per unit face area

F_AREA(A,f,thread);

area=NV_MAG(A); //Get face area from Fluent

flux=deposit_mass/area;




F_UDMI(f,thread,0)+=deposit_mass;




//Add thickness to slag layer if the face temperature is higher than T_Slag, then kill

particle and return

if(F_T(f,thread)>T_Slag)

        {

        printf("Slag\t%lf\n",F_UDMI(f,thread,5));

        F_UDMI(f,thread,4)+=flux/RHO_Slag;
```

```
        return(PATH_ABORT);

        }
```

//Add thickness to sintered layer if the face temperature is higher than T_Sinter, then kill

particle and return

```
if(F_T(f,thread)>T_Sinter)

        {

        printf("Sinter\n");

        F_UDMI(f,thread,3)+=flux/RHO_Sinter;

        return(PATH_ABORT);

        }
```

//Add thickness to particulate layer if the surface temperature is lower than T_Sinter, then

kill particle and return

```
//printf("Particulate\n");

F_UDMI(f,thread,2)+=flux/RHO_Particulate;

return PATH_ABORT;

}
```

//Heat flux boundary condition

```
DEFINE_PROFILE(heat_flux_BC,thread,i)

{
```

```c
real pos_vec[ND_ND];

real R_EFF,wall_temp;

face_t f;


        begin_f_loop(f,thread)

        {

        //Calculate Effective thermal resistance of ash layers

        R_EFF=R_BASE+F_UDMI(f,thread,4)/K_Slag+F_UDMI(f,thread,3)/K_Sinter+
F_UDMI(f,thread,2)/K_Particulate;

        F_UDMI(f,thread,1)=R_EFF;


        wall_temp=F_T(f,thread); //Get boundary temperature from Fluent


        //Define heat flux at face f

        F_PROFILE(f,thread,i)=(T_Cool-wall_temp)/R_EFF;

        printf("R_eff = %f\n", R_EFF);

        }

        end_f_loop(f,thread)

}


//Emittance Boundary Condition - this very simple model is used until FTIR data is
available
```

```
DEFINE_PROFILE(Emittance_BC,thread,i)

{


real pos_vec[ND_ND];

real xloc, wall_temp;

face_t f;


        begin_f_loop(f,thread)

        {

        wall_temp=F_T(f,thread);


        F_PROFILE(f,thread,i)=.85+.00001*wall_temp;


        }

        end_f_loop(f,t)

}



//Reset UDML to Zero - This is a "define on demand" UDF so it is executed by the user

DEFINE_ON_DEMAND(Reset_UDMLs)

{


int i=0;
```

```
Thread *t;

Domain *d;

face_t f;


d = Get_Domain(1);


thread_loop_f(t, d)

    {

        begin_f_loop(f,t)

          {

                    for(i = 0; i < 6; i++)

                            F_UDMI(f,t,i)=0; //Set UDM to zero

          }

        end_f_loop(f, t);

    }

}


//Injection initialization UDF that defines the transition to a new simualtion timestep,

//First checks for melting and sintering, then increments simulation time, then injects new

particles

DEFINE_DPM_INJECTION_INIT(Injection_Init,I)

{
```

```
int i;

real current_time=0;

Thread *t;

Domain *d;

face_t f;


real R_Part, R_Sint, R_Slag, R_Total, L_Part, L_Sint, L_Slag, T_SintSlag_ifc,

T_PartSint_ifc, T_Surface, Delta_L_Sint,

Delta_L_Melt, Y_Sint, Y_Part;


d = Get_Domain(1);


//Check Sintering and Melting


thread_loop_f(t, d)
  {
    if (NNULLP(THREAD_STORAGE(t,SV_UDM_I)))
     {
      begin_f_loop(f,t)
       {
        L_Part=F_UDMI(f,t,2);
          L_Sint=F_UDMI(f,t,3);
```

```
L_Slag=F_UDMI(f,t,4);

R_Part=L_Part/K_Particulate;

R_Sint=L_Sint/K_Sinter;

R_Slag=L_Slag/K_Slag;

R_Total=R_Part+R_Sint+R_Slag+R_BASE;

T_Surface=F_T(f,t);


//Calculate Interface Temperatures Between Ash Layers

T_PartSint_ifc=T_Cool+(T_Surface-T_Cool)*(R_Part+R_BASE)/R_Total;

T_SintSlag_ifc=T_Cool+(T_Surface-
T_Cool)*(R_BASE+R_Part+R_Sint)/R_Total;


//Check Melting and melt appropriate amount of sintered layer

if(T_SintSlag_ifc > T_Slag);

{

Y_Sint=R_Total*K_Sinter*(T_Slag-T_Cool)/(T_Surface-T_Cool)-
K_Sinter*(R_Part+R_BASE);

Delta_L_Melt=L_Sint-Y_Sint;

F_UDMI(f,t,3)=Y_Sint;

F_UDMI(f,t,4)=L_Slag+Delta_L_Melt*RHO_Slag/RHO_Sinter;

}
```

```
//Check sintering and sinter appropriate amount of particulate layer

if(T_PartSint_ifc > T_Sinter);

{

Y_Part=R_Total*K_Particulate*(T_Sinter-T_Cool)/(T_Surface-T_Cool)-
R_BASE*K_Particulate;

Delta_L_Sint=L_Part-Y_Part;

F_UDMI(f,t,2)=Y_Part;

F_UDMI(f,t,3)=L_Sint+Delta_L_Sint*RHO_Particulate/RHO_Sinter;

}

}

}

end_f_loop(f, t);

}

}


//Increment simulation time, print to screen and store current simulation time at UDM
No.5

thread_loop_f(t, d)

{

  if (NNULLP(THREAD_STORAGE(t,SV_UDM_I)))

    {

    begin_f_loop(f,t)

      {

      F_UDMI(f,t,5)+=TIMESTEP_SIZE;
```

```
            printf("current_time = %f\n", F_UDMI(f,t,5));

        }

      end_f_loop(f, t);

    }

  }


}
```